

An Investigation of Morphology and Transport in Amorphous
Solid Water via Guest-Host Interactions

by

Jaimie Elizabeth Stomberg

A Dissertation Presented to the
FACULTY OF THE GRADUATE SCHOOL
UNIVERSITY OF SOUTHERN CALIFORNIA
In Partial Fulfillment of the
Requirements of the Degree
DOCTOR OF PHILOSOPHY
(Chemistry)

July 2015

Copyright 2015

Jaimie Elizabeth Stomberg

*I dedicate this thesis to my husband, Matthew Mills, who is my partner in science and
in life.*

“Science is magic that works.” –Kurt Vonnegut

Acknowledgements

First and foremost, I would like to thank my advisors: Curt Wittig and Hanna Reisler. They have both pushed me to think critically about the scientific process and my data, and I have become a better scientist because of it. Without their guidance, I would not be where I am today.

A close second in influence and help has been Stephanie McKean, my cohort in science throughout my entire graduate school career. She has provided a much-needed resource of support, insight, and friendship in a stressful environment, and I will be forever grateful.

I would also like to extend my appreciation to all of the people who have given me help from the Wittig and Reisler groups throughout the years (not to mention the physical chemistry community in SSC). They have all given me valuable information, been able to provide something to fix a broken instrument, or has pointed out something I never would have thought of on my own. In particular, I have benefited from the wisdom of Oscar Rebolledo-Mayoral and Chris Larson as they worked on this project with me.

I also want to thank the Women in Science and Engineering program, and by extension the Women in Chemistry group, at USC. Not only did they provide me with funding, but they gave me the opportunity to be part of a community of women who are inspiring, supportive, and smart as hell.

Lastly, I would like to thank my family. My father, Keith Stomberg, made sure I knew how to fix things myself when I was young, which has proven to be a valuable skill in the lab. My late brother, Wayne Stomberg, inspired me to try harder every day to improve the world. My fantastic mother, Maribeth Stomberg, has supported me since birth, and I could never have achieved as much without her presence in my life.

And of course, I never would have made it through graduate school without the steady presence of my husband, Matthew Mills. He is my rock and I am so thankful to have him as my partner.

Table of Contents

Dedication	ii
Acknowledgements	iv
List of Figures	xiii
List of Tables	xiv
Abstract	xvi
1 Introduction	1
1.1 Water: a Complex Molecule	1
1.1.1 Amorphous Solid Water	3
1.1.2 Amorphous Solid Water and Guest Molecule Interactions	7
1.2 Amorphous Solid Water in the Interstellar Medium	10
1.3 NO ₂ /N ₂ O ₄	12
1.4 Thesis Overview	15
Chapter References	16
2 Experimental Methods	21
2.1 Time-of-Flight Mass Spectrometry	21
2.1.1 Jacobian	24
2.1.2 Resolution	25
2.2 Laser-Induced Desorption	28
Chapter References	32
3 Experimental Apparatus	33
3.1 Ultra-High Vacuum System	33
3.2 Surface Manipulator	34
3.3 Surface Holder and MgO Surface	36
3.4 Sample Growth	39
3.4.1 Calibration Using TPD	41
3.4.2 Directed Dosing vs. Background Dosing	43
3.5 Time-of-Flight Mass Spectrometer	43
3.6 Time Synchronization	49
3.7 FTIR	51
Chapter References	54

4	Effects of Buried Heat in Amorphous Solid Water Films	55
4.1	Introduction	55
4.2	Experimental	57
4.2.1	Changing to UV: Using NOCl as a Test Species	60
4.3	Results	63
4.3.1	Standard Spectra and Data Analysis	63
4.3.2	ASW Spacer	67
4.3.3	N ₂ O ₄ Thickness	71
4.3.4	Laser Energy	71
4.3.5	Multiphoton Effects	75
4.3.6	ASW Upper Layer Thickness	77
4.3.7	High Fluence vs. Low Fluence	86
4.3.8	N ₂ O ₄ Codeposition	88
4.4	Discussion	88
4.4.1	Time Scales	91
4.4.2	Fissures	92
4.5	Conclusions	94
	Chapter References	96
5	Introducing a Third Species: Molecular Transport and Isotope Exchange	99
5.1	Introduction	99
5.2	Experimental	101
5.2.1	CO ₂ and C ₂ H ₂	102
5.2.2	D ₂ O	102
5.3	Results	103
5.3.1	Depth Profiling With CO ₂ and C ₂ H ₂	103
5.3.2	Switching to D ₂ O	107
5.4	Discussion	112
5.5	Conclusions	115
	Chapter References	117
6	Future Work	119
6.1	Improvements in Experimental Apparatus	119
6.2	Introducing a Third Species: What Next?	121
6.3	Gold nanoparticles as Fissure-Creators	121
6.4	Experimental Strategy	124
6.4.1	Surface Preparation and Experimental Adjustments	124
6.5	Initial Results	126
6.5.1	Nanoparticle Breakdown	127
6.6	Summary and Future Experiments	128
	Chapter References	131
	BIBLIOGRAPHY	132

List of Figures

- 1.1 A 3D depiction of hexagonal ice (HI), the most common form of crystalline ice on earth. Each water molecule participates in 4 hydrogen bonds with neighboring molecules, which forms a tetrahedral structure and characteristic long-range order. 2
- 1.2 (a) Ball-and-stick model of N_2O_4 . The N–N bond is quite weak (around 0.5 eV) [2, 84]. (b) The bcc structure is the dominant structure of crystalline N_2O_4 at low temperatures. Defects, including presence of the NO_2 and unstable isomer ONONO_2 , start to appear below 20 K [17]. . . 13
- 2.1 A schematic of a linear two-stage Wiley-McLaren TOFMS system. Material enters the region between repeller and extractor plates initially kept at the same voltage (A). If necessary, the material is ionized (this can be done by electron impact ionization, photoionization, etc). Subsequently, the voltage is dropped on the extractor plate and ionized material is extracted and further accelerated by a grounded third plate into a field-free drift region (C). Ionized material of different masses can be differentiated by flight times, with more massive ions arriving after lighter ions (relative mass is indicated by size in the diagram). 22
- 2.2 Two particles of the same mass, A and B, are ionized in a finite ionization region with a width of Δl . The flight path can therefore differ by a range of $\pm\Delta l/2$; in this case, particle A will have a shorter flight path than particle B. However, particle B will gain more kinetic energy than particle A. This means that there will be a point in space where particle B will pass particle A. 26
- 2.3 A particle trajectory, depicted as a blue circle, with initial kinetic energy U_0 . Only the component in the direction of extraction will affect the overall kinetic energy of the extracted particle, U_{tot} 27
- 3.1 An external view of the UHV chamber (not to scale). Key sections are labeled. The surface manipulator provides xyz translation capabilities. The window through which UV radiation enters for a typical experiment is designated with a star. The diamond indicates the FTIR pathway. 35

3.2	An exploded view of the substrate holder and associated components. Two machined copper pieces are electrically isolated from each other by a custom ceramic spacer and attached to the copper block with long screws fixed with flat and ceramic hat washers on each side. Two 18-gauge copper wires are screwed to the machined pieces to allow for current to flow through the tantalum heater that is bonded to the back of the substrate holder. A thermocouple is glued to the “hot” side of the MgO substrate and connected to a wire threaded through the LN ₂ reservoir sheath.	38
3.3	An AFM image of a cleaved MgO(100) surface. The surface is quite flat and unblemished, with terraces as the main visible feature along with a slightly larger aberration.	39
3.4	(a) TPD spectra from ASW films (20-100 ML) grown in standard dosing position (Tier 2). The bulk ASW desorption occurs at 165 K, with a crystallization peak that appears at 160 K. (b) Integrated areas from the plots in (a) compared to previously calibrated film thicknesses.	42
3.5	FTIR spectra of ASW grown by background and directed dosing, each at 2×10^{-7} Torr for 5 minutes (equivalent to 100 ML for background deposition). Removing the contribution of material that grows on the back side of the MgO substrate (see text for discussion of this calculation), directed dosing increases film thickness by a factor of 1.7 when compared to background dosing.	44
3.6	A schematic representation of the TOFMS experiment. The fourth harmonic from a Continuum Nd:YAG is used. The beam waist is reduced to 3 mm using a telescope. The radiation enters the chamber and excites the film at normal incidence. Released material is ionized, extracted, and then detected using a multi-channel plate (MCP) at a rate of 100 kHz. The set-up shown is with focused radiation, which allows for 9 individual “experiments” on one film via translation in the <i>xz</i> plane, as indicated by the grid. These data can be averaged to improve S/N. By removing the 50 cm lens, a larger area can be irradiated (shown in light purple) to allow FTIR experiments of the ablated film.	46
3.7	(a) An example of a full temporal profile. It is the average of data collected from eight individual spots from a film of 80 L of N ₂ O ₄ ablated with focused 1.0 mJ radiation. Each 10 μs segment represents a full mass spectrum, shown as (b), of a segment of the plume of material that desorbs from the surface. The data can be analyzed as a full temporal profile or as individual mass spectra.	48

3.8	A schematic of the four SRS DG535 Digital Delay/Pulse Generators that control the triggering for the TOFMS, chopper wheel, and Nd:YAG laser flash lamps and Q-switch; only necessary connections and switches have been depicted for clarity. Refer to Table 3.1 for individual pulse generator settings.	50
3.9	A schematic of the top chamber tier, showing the FTIR pathway. Radiation from the detector is directed and focused through the surface using flat and parabolic mirrors. It is then focused on a liquid nitrogen-cooled InSb detector with a second parabolic mirror. All external optics are encased in plexiglass boxes that are purged with dry air.	52
4.1	(a) FTIR spectrum of 100 L of N ₂ O ₄ . The sharp peak at 2960 cm ⁻¹ is a weak combination band [110]. All fundamental bands for N ₂ O ₄ are below the detection range of the InSb detector used in these experiments (cutoff at 1850 cm ⁻¹), so this small peak was the only indication of the presence of N ₂ O ₄ on the surface. However, it was distinct and reproducible. (b) FTIR spectrum of 110 L of NOCl (negative peaks are due to decrease in water vapor signal on the experimental time scale). The peak centered at 1955 cm ⁻¹ is the N–O bond stretching mode [62]. We did not detect any other peaks associated with NOCl. While this particular peak is also representative of NO only, our surface was not cold enough to condense NO [35]. Furthermore, we were able to desorb fragments of NOCl successfully with UV radiation.	62
4.2	Mass spectrum of NO ₂ , N ₂ O ₄ , NO, and H ₂ O obtained from our experimental apparatus. All ratios given are based on peak areas. (a) 300 K NO ₂ leaked into the UHV chamber gives NO ⁺ /NO ₂ ⁺ = 3.18, O ⁺ /NO ₂ ⁺ = 0.58, and N ⁺ /NO ₂ ⁺ = 0.19. (b) 300 K NO leaked into the chamber gives O ⁺ /NO ⁺ = 0.01 and N ⁺ /NO ⁺ = 0.06. The NO ²⁺ signal at <i>m/q</i> = 15 is a distinctive feature of NO electron impact ionization. (c) 300 K H ₂ O leaked into the chamber gives OH ⁺ /H ₂ O ⁺ = 0.27, O ⁺ /H ₂ O ⁺ = 0.02, and H ⁺ /H ₂ O ⁺ (not shown) = 0.07. (d) The spectrum obtained via N ₂ O ₄ sublimation at ~155 K gives NO ⁺ /NO ₂ ⁺ = 0.9, O ⁺ /NO ₂ ⁺ = 0.1, and N ⁺ /NO ₂ ⁺ = 0.02. Neither N ₂ O ₃ ⁺ or N ₂ O ₄ ⁺ (76 <i>m/q</i> and 92 <i>m/q</i> , respectively) was detected (not shown).	66
4.3	(a) The initial design for a TOFMS electrode to minimize the effect of molecular collisions with the plates. (b) Improved design for a TOFMS electrode to allow material to pass out of the ionization region. The stars designate the openings parallel to the substrate through which desorbing material would enter the ionizing region.	67

4.4	Temporal profiles of NO_x^+ signal with and without an ASW spacer, with cartoon depictions of deposition films. Both films were irradiated with a focused 266 nm, 1.0 mJ beam. (a) 80 L N_2O_4 deposited on a bare MgO substrate. (b) 80 L N_2O_4 deposited on 300 ML ASW.	68
4.5	Averaged mass spectrum from extractions 2-11 (20-110 μs) of data from Figure 4.4b. All species detected can be attributed to N_2O_4 irradiation and cracking. There is a slight bump at mass 18, but it is insignificant in comparison to the other peaks and compared to previous experiments conducted by this lab.	70
4.6	Sum of peak areas for NO^+ and NO_2^+ signals from laser ablation of 20-100 L N_2O_4 films grown on 300 ML of ASW. The signal increases with increasing thickness, indicating that absorption within the film hasn't been saturated in the range of thicknesses studied.	72
4.7	Sum of peak areas for NO^+ and NO_2^+ signals from laser ablation of 80 L N_2O_4 dosed on 300 ML H_2O . The signal generally increases with increasing laser energy.	73
4.8	A representative resolved TOF spectrum of the fast ions from the first extraction. The spectrum has been shifted to account for the 2 μs delay. The peaks are labeled with probable species assignments.	76
4.9	Nine first-pulse temporal profiles from a single 300 ML D_2O /80 L N_2O_4 /2400 ML H_2O sandwich (1.0 mJ focused radiation, configuration shown in cartoon, depicted on common scale). For clarity, water signal is shown in black and NO_x^+ signal is shown in red. The irregularity of the water signal, particularly at long times, is indicative of nonthermal processes. The amount of signal at long times is considerable. It should also be noted that the NO_x^+ signal does not exhibit this behavior and decays with time.	79
4.10	A water monomer's kinetic energy compared to its flight time, assuming the molecule left the surface at $t = 0$	80
4.11	Temporal profiles comparing first and second incident pulses for upper H_2O layer thickness: (1) 600 ML, (2) 1200 ML, and (3) 2400 ML. Each profile is the average of nine individual profiles (1 mJ, 266 nm). Red peaks designate NO^+ and NO_2^+ . Black peaks denote H_2O^+ , OH^+ , and H^+ . All temporal profiles are on the same ordinate scale. The lower ASW layer is 300 ML of D_2O and the N_2O_4 layer is 80 L (sample composition shown at bottom).	82
4.12	Mass spectra representing the 100 μs extraction from each temporal profile in Figure 4.11; refer to the caption of that Figure for composition details. The peaks in spectrum (a) have been labeled with ion assignments for clarity.	83

4.13	Plots of R_N for each extraction with good S/N from each temporal profile in Figure 4.11; refer to the caption of that figure for composition details. After the initial extractions, first pulse R_N values (filled circles) level off around unity. Second pulse R_N values (open triangles) follow the same qualitative trend but level off at higher values, indicating the presence of N_2O_4 in the surface region.	84
4.14	(a) Overlaid FTIR spectra of a 300 ML D_2O /80 L N_2O_4 /2400 ML H_2O sandwich (configuration depicted in figure) before and after 70 shots of 6 mJ radiation. A 3 mm beam waist was used to ensure that a reasonable area was available for FTIR measurements. The red line represents the spectrum of the undisturbed film; the black line is the spectrum collected after irradiation. The O–D stretch peak centered at 2435 cm^{-1} is virtually unchanged, but the O–H peak centered at 3250 cm^{-1} is reduced by 14%. (b) 2400 ML of H_2O was annealed at 165 K for 10 minutes to induce crystallization and is shown for comparison. The “after” spectrum in (a) did not show any observable increase in crystallinity despite the prolonged exposure to laser radiation.	85
4.15	Averaged mass spectrum from extractions 2-11 (20-110 μs) of data from a low fluence experiment (0.2 J/cm^2) with the same film composition as Figures 4.4b and 4.5 (300 ML ASW/80 L N_2O_4). The difference in the NO^+/NO_2^+ ratio compared to Figure 4.5 is striking.	87
4.16	Expanded mass spectrum of 80 L N_2O_4 codeposited with 240 ML of ASW and irradiated with focused 1.0 mJ radiation. Five first-shot experiments from the film have been averaged to improve S/N. While small, clusters up to the protonated water tetramer were visible. No protonated species were detected in any of the experiments where N_2O_4 was deposited as a discrete layer. It is also important to note that there is no signal at $m/q = 62$, which would indicate the presence of NO_3^+	89
4.17	A cartoon depiction of how material expelled from neighboring fissures may interact.	93
5.1	Cartoon depiction of different sandwich configurations using a third species as a probe (black represents the MgO substrate). Typical ASW sandwiches are deposited in layers, with layers of CO_2 or C_2H_2 deposited at different depths within a film. Thicknesses used were 300 ML for the bottom H_2O spacer, 80 L for the N_2O_4 layer, and 100 ML of CO_2 or C_2H_2 . The top H_2O layer was 200 ML [consisting of two separate 100 ML sections for configuration (3)].	102

5.2	Mass spectra averaged from extractions 2-21 where CO ₂ is underneath the ASW/N ₂ O ₄ sandwich [configuration (1) in Figure 5.1]. Mass spectrum (a) is after the first laser pulse, while (b) is from the second pulse incident on the same location (2.0 mJ); CO ₂ ⁺ peaks are boxed in red for clarity. In (a), the very small peak at mass 44 shows how little CO ₂ escapes the film. This signal increases significantly after the second pulse on the same spot, indicating a morphological change that allows for CO ₂ to move upward through the film.	105
5.3	Temporal profiles comparing CO ₂ ⁺ signal in configuration (2) versus (3) (refer to Figure 5.1). Trace (a) is the result of configuration (2); trace (b) is due to ablation of configuration (3). For both temporal profiles, data was averaged for the first incident shot on 9 spots on the film (2.0 mJ). Signal due to H ₂ O, N _x O _y and CO ₂ are designated by black, red, and blue, respectively. Because CO ₂ ⁺ is partially obscured by NO _x ⁺ signal, a trace of its outline is drawn in blue for clarity. (a) When CO ₂ is deposited directly on top of N ₂ O ₄ , its temporal profile tracks with the NO _x ⁺ signal. (b) Embedding CO ₂ in the upper water layer results in a smaller signal when compared to (a), as well as slower CO ₂ ⁺ signal that tracks more closely with the water. Taken together, the traces indicate that material removal occurs via two different pathways: mixing with the hot fluid and scraping of fissure walls.	106
5.4	Waterfall plot of averaged mass spectra (8-9 spots, 20 extractions) from experiments using C ₂ H ₂ in configuration (3) where the water spacer between C ₂ H ₂ and N ₂ O ₄ ranged from 100 to 0 ML. The main fragments detected from C ₂ H ₂ are C ₂ H ₂ ⁺ , C ₂ H ⁺ , and C ₂ ⁺ (indicated by the red arrow). Change in C ₂ H ₂ fragment signal is small as the H ₂ O spacer between N ₂ O ₄ and C ₂ H ₂ is decreased. However, the complete removal of a water spacer results in a significant C ₂ H ₂ signal drop.	108
5.5	Overlaid FTIR spectra of a film initially grown at 100 K of 300 ML of H ₂ O deposited on 300 ML of D ₂ O (red) that was then heated to 160 K for 1.5 minutes (black). The appearance of a central structure in both peaks is indicative of HDO exchange occurring; there may be some contribution from crystallization of the film, but the impact should be small due to heating the film for <2 minutes. This shape change was not detected at lower temperatures or when the sample was left to sit for 20 minutes at 100 K. The negative-peak distortion of the O–D peak is due to background age.	109

5.6	Representative mass spectra showing HDO ⁺ formed from isotopic scrambling during the ablation process. The spectra are averaged from the first 20 extractions yielding signal from first laser pulse temporal profiles (1.5 mJ). Mass peaks are labeled in (a) for clarity. The film layer thicknesses for both samples (a) and (b) are: 300 ML H ₂ O, 80 L N ₂ O ₄ , and 200 ML each of H ₂ O and D ₂ O (configurations depicted in cartoons). . .	111
5.7	Plot showing the inverse between R_I and film thickness. R_I values were calculated for sandwich configurations like that depicted in Figure 5.6, comparing D ₂ O on top of a layer of H ₂ O or underneath a layer of H ₂ O. The thicknesses reported on the x -axis refer to the thickness of the individual D ₂ O and H ₂ O layers (<i>i.e.</i> , the top layer of the sandwich is twice as thick). There is a clear decrease in R_I as the thickness of the H ₂ O and D ₂ O layers increases.	112
6.1	Cartoon depiction of how gold nanoparticles can be used to form channels in ASW using 532 nm radiation, which is resonant with 10-80 nm gold nanoparticles. (1) Nanoparticles are deposited on a bare MgO surface, and particle density is determined using AFM. (2) A layer of N ₂ O ₄ , followed by ASW is grown over the nanoparticles. (3) 532 nm radiation is focused on the surface, heating the nanoparticles via surface plasmon resonance to remove material. Once SPR heating is no longer able to remove material, UV radiation (355/266 nm) is used to excite the N ₂ O ₄ layer. (4) This iterative process can form vertical channels in the ice that are roughly the diameter of the gold nanoparticle and length of the film. Once these channels are formed, they can be doped with molecules of interest and the film can be further probed with spectroscopic techniques.	123
6.2	AFM image of a MgO(100) surface wetted with one drop of a solution containing 20 nm gold nanoparticles with a concentration of approximately 6×10^{10} nps/mL. This scan was taken from the center of the surface, where the density of the particles was ~ 10 nanoparticles per square micron. In scans taken near the edge of the surface, the density of nanoparticles was slightly higher and more aggregates of particles were visible.	125
6.3	A temporal profile of 300 ML of ASW grown over 20 nm gold nanoparticles after irradiation with 6.4 mJ of focused 532 nm light (average of three spots). The majority of the signal is due to water and water fragments, with some contribution from citrate fragments.	127
6.4	AFM images of 80 nm gold nanoparticles on the MgO substrate before (a) and after (b) laser ablation. The particle density of the freshly-prepared film was approximately 1 particle per micron. The particles in (b) have experienced several 532 nm pulses at a fluence of up to ~ 3 J/cm ² .	129

List of Tables

3.1	Timing settings for each pulse generator used in the timing set-up. Note: all of the pulse generators are triggered at 100 kHz except for the pulse generator triggering the optical chopper, which has a repetition rate of 100 Hz. Refer to labels from Figure 3.8.	51
4.1	70 eV ionization cross sections for detected molecules. All values obtained from the NIST database [90], except for N_2O_4 , which was computed from the equation given in [73].	65
4.2	R_N values for different laser energies at different extraction times. The changing ratio indicates that different species are the result of the desorption process, such as collisions; a consistent value would indicate all species are due to a fragmentation process that occurs in the ionization region.	75

Abstract

The effects of inserting energy in a buried stratum in amorphous solid water (ASW) films were investigated using pulsed 266 nm radiation. Material ejected from irradiated films was detected with time-of-flight mass spectrometry (TOFMS). A technique was developed using N_2O_4 in conjunction with focused UV radiation ($\sim 1 \text{ J/cm}^2$) that enabled facile introduction of energy in a spatially selective way via an electronic transition of N_2O_4 . A variety of experiments were carried out to explore the structural changes induced by the sudden addition of energy to ASW films, and an attempt was made to characterize the nature of transport within and above the surface of the film.

Layered ASW/ N_2O_4 films, up to 2800 monolayers (ML) thick, were grown on a MgO(100) substrate. All samples were grown at $\sim 100 \text{ K}$ under ultra-high vacuum conditions to produce porous, high quality films. Once deposited, the films were irradiated with 266 nm radiation that was generated as the fourth harmonic of a Nd:YAG laser (10 ns pulses, reduced to 1 Hz) focused to a 0.3 mm beam waist. After a single laser pulse incident on the film, the N_2O_4 layer was converted to a hot fluid that heated the surrounding material. Heating of the film competes with cooling by the MgO(100) substrate, which acts as an efficient heat sink due to its high thermal conductivity (250 W/mK). Therefore, extreme pressure and heat gradients exist within the film upon radiation and the film cools quickly upon cessation of the laser pulse.

Despite fast cooling of the film, laser-heated N_2O_4 fluid, along with water monomer, was detected at times greater than 1 ms. This was due to a catastrophic structural change triggered by the temperature and pressure gradients, which resulted in the formation of fissures. The hot fluid of N_2O_4 and its photoproducts escaped to ultra-high vacuum through these fissures, scraping the walls and removing H_2O molecules. Long flight times were attributed to collisions occurring above the surface of the film due to the high density of the escaping material and prevalence of fissures in the irradiated area. Fissures proved to be robust, with spectra from subsequent pulses on the same spot resembling spectra of exposed N_2O_4 .

This model will be explored further by implementing gold nanoparticles as fissure-creators. Being able to form fissures of a known dimension and density within an ASW film would allow for more careful analysis of this system and would be the first demonstration of induced morphological changes in ASW that are relatively well-defined. An outline of this technique is presented, along with preliminary results.

Introduction

Analyzing amorphous solid water interacting with the guest species N_2O_4 is the central focus of this dissertation. Amorphous solid water (ASW) as an experimental species is useful for modeling liquid water, glassy materials, and highly porous compounds because of its disordered structure. It is also of great interest to the astrochemical community due to its prevalence in the interstellar medium and its unique characteristics. Therefore, it is necessary to begin with a discussion of ASW properties, as well as a brief summary of key experiments conducted with this mercurial substance.

1.1 Water: a Complex Molecule

Water is a research interest to scientists because of its omnipresence on Earth and in the interstellar medium (ISM) [1–6]. It is involved in innumerable mechanisms in life processes and acts as a near-universal solvent. Because of this, water is one of the most investigated materials in science. Its simple molecular structure consisting of two hydrogen atoms bonded to an oxygen atom belies its many unusual properties. These include its high heat capacity, maximum density at 4 °C, glass transition, and many solid phases [3, 7–9]. The exact nature and origin of these properties are still not well understood and require additional study. Building a cohesive picture is further complicated by the fact that the intramolecular interactions of water are dominated by hydrogen bonding, which is notoriously difficult to model [10–12]. Because of this,

investigation of water and aqueous systems continues to be a path for scientists to gain insight into this ubiquitous molecule.

A unique feature of water is its many solid phases; there are at least 15 defined crystalline states of water [9]. The most common on Earth is hexagonal water, HI, which is thermodynamically and kinetically favorable at atmospheric pressure. It has a regular structure that is characterized by a tetrahedral hydrogen-bonding network, as shown in Figure 1.1. When ice crystallizes below 240 K it can have a different structure, identified by König in 1944 as cubic ice (CI) [13]. Both hexagonal and cubic ice have a tetrahedral first coordination shell; the difference arises from the stacking arrangement of hexagonal bilayers [14].

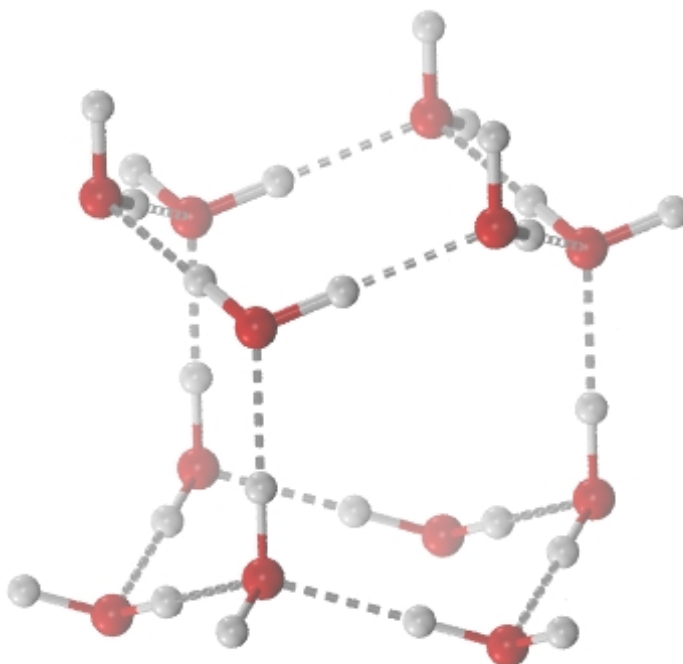


Figure 1.1: A 3D depiction of hexagonal ice (HI), the most common form of crystalline ice on earth. Each water molecule participates in 4 hydrogen bonds with neighboring molecules, which forms a tetrahedral structure and characteristic long-range order.

Condensing water at temperatures of ≤ 140 K gives rise to solid water with long range disorder referred to as amorphous solid water (ASW) [15–19]. Due to the low temperature needed for formation, on Earth it is only found in laboratories. However,

it is believed to be the most common form of water in the universe due to its prevalence in the ISM. Amorphous solid water is known to be a component of dust grains, satellites, and planetary rings [4, 6]. Studying its characteristics and interactions with other molecules is important for understanding the fundamental chemical and physical reactions occurring in the universe. ASW is also useful in the laboratory environment because its disordered structure resembles that of the liquid phase, but its molecular immobility makes it more appealing for study [8]. It has even been used as a substrate to investigate large molecules and biological compounds, such as RNA, in order to freeze material in a hydrated solid phase to allow for electron microscopy of embedded material [20]. However, much about its structure and molecular interactions remain unknown, so continued study is needed to illuminate properties of this unusual compound. It is necessary to provide an outline of ASW characteristics, which will be given in the subsequent section.

1.1.1 Amorphous Solid Water

Amorphous solid water is a complex substance, with multiple morphologies. Furthermore, structural changes can occur through temperature changes or other insertions of energy into the ASW system. This section will consist of a brief summary of ASW characteristics, as well as concepts and experiments done in this lab and others as this information is relevant to the results reported later on in this dissertation.

Amorphous ice was first discovered in 1935 by Burton and Oliver in an X-ray diffraction study of water that had been vapor-deposited on a cryoplate held at 100 K [21]. The absence of Bragg peaks indicated a long-range internal disorder that is representative of an amorphous solid. In this way, ASW is analogous in form to liquid water [8]. Since this initial report, multiple formation methods and unique amorphous phases have been reported in the literature. The sample preparation method dictates the structure of the ASW sample, so it is instructive to describe the most common techniques.

One of the most popular methods of ASW creation is vapor deposition of water at temperatures below 140 K [3]. At these temperatures, kinetic factors dominate structural growth, despite a crystalline structure being more thermodynamically favorable. Film growth at ≤ 30 K will produce high-density amorphous solid water (HDA), while higher temperatures will grow low-density amorphous solid water (LDA) [22, 23]. The angle of deposition also affects the amorphous structure; the specific effects of this will be discussed in a later section. Another preparation of ASW samples is the fast quenching of small liquid water drops at cryogenic temperatures [24]. Samples prepared with this method are sometimes referred to as hyperquenched glassy water (HGW). Finally, hexagonal ice can undergo a transition to amorphous ice if it is subjected to pressures in excess of 1 GPa [25, 26]. This process is referred to as pressure-induced amorphization (PIA) and produces HDA. There are two mechanisms that have been suggested for this transition: “melting” of ice to generate a vitreous solid [25], or mechanical collapse of the HI structure itself [27]. HDA can also undergo another transition to very high-density amorphous solid water (VHDA) if subjected to increased pressure and annealing [28, 29]. The work presented in this dissertation deals only with vapor-deposited ASW (*i.e.*, LDA), but a discussion of the different morphologies is required for context.

LDA, HDA, and VHDA are the three designations of ASW morphologies that are well agreed on in the scientific community [3, 7, 9, 30, 31], though there is still some debate about the distinction between the latter two structures [17]. LDA has an average density similar to that of hexagonal ice, 0.94 g/cm^3 . In contrast, HDA has a density of 1.17 g/cm^3 and VHDA has a density of 1.25 g/cm^3 (and even higher densities have been reported) [3, 31]. Conversely, the hydrogen bond length *increases* with increasing density [28, 29]. This seemingly incongruous trend is due to local structure of ASW. Unique to amorphous water compared to other amorphous materials is that it has localized order: analysis of high frequency dynamics of ASW has revealed crystal-like

phonon excitations that indicate local structure is well-ordered [32]. However, it is important to emphasize the fact that this is indicative of *local order only*; amorphous solid water is designated as such due to its *long range disorder*. Experiment and simulations have found that the local structure in ASW adopts a tetrahedral arrangement similar to that in crystalline ice [30, 33, 34]. Therefore, ASW roughly follows the same local structure rules for ice published by Bernal and Fowler in 1933 [35]. A water molecule will have a tetrahedral coordination shell with the surrounding 4 molecules. This network is known as the Walrafen pentamer [34]. The structural differences between the amorphous phases is due to the presence (or lack thereof) of molecules in the interstitial sites. LDA has an “empty shell” between the first coordination shell and the second shell. In comparison, HDA has one water molecule in the empty shell and VHDA has two [23, 29, 34]. The presence of these additional molecules increases the density while at the same time causes a distortion in the Walrafen pentamer that pushes the molecules slightly apart, therefore increasing hydrogen bond length. In this way, these contradictory trends of density and hydrogen bond length are reconciled.

ASW is a metastable form of solid water; simply put, this means that it forms due to energy restrictions impeding rearrangement to a more thermodynamically favorable (crystalline) structure. Because ASW is formed due to kinetic factors and not thermodynamic stability, it is highly susceptible to morphological changes. It is possible to change from one ASW morphology to another through external stress on the system. For example, amorphous ice can experience relaxation to less strained morphologies. This occurs in HDA formed from PIA, which will experience a slight change in density as it structurally relaxes upon annealing (heating) [17]. ASW can also experience amorphous-amorphous phase transitions via annealing or pressure changes. Defined as polymorphism, this is a property that is very rare in the chemical world [9, 17, 31]. In addition, temperature-programmed desorption (TPD) studies done by this lab and others have found unique transformations that occur in the ASW as it is heated. When ASW is subjected to heating, the structure can abruptly change at specific temperatures

[1, 36, 37]. The most significant change occurs around 140 K, when the structure undergoes a rapid transition via irreversible crystallization. This transition acts as a marker for the presence of ASW and can be consistently observed in TPD experiments as a “bump” in the desorption peak [38]. This results from a change in vapor pressure due to the decrease in free energy when transitioning from ASW to PCI. It is important to note that the temperature of crystallization is not a set temperature as this is a kinetic process, not a thermodynamic process. Therefore, the experimental conditions (such as ramp rate) play a role in the crystallization temperature [36]. Above this temperature, solid water exists as a mix of cubic ice and hexagonal ice known as polycrystalline ice (PCI) [14]. Crystallization can be induced at even lower temperatures if the ASW film is grown on a crystalline water substrate due to the removal of the nucleation activation barrier [39].

ASW behavior near the crystallization temperature has been the focus of intense study. Near this temperature it is believed that water undergoes a glass transition to a highly viscous fluid [18, 40, 41]. A glass transition is usually determined experimentally using differential scanning calorimetry (DSC). When a material goes from its glass state to a supercooled liquid, there is a significant increase in heat capacity as degrees of freedom become unfrozen. ASW exhibits such an increase at 136 K; however, the increase is extremely small when compared to the transition behavior of classically glassy materials [42]. This has resulted in much debate about the temperature of the glass transition or whether it actually exists at all [7, 43]. Another investigation pathway into the “glassy water” question is analysis of diffusion rates. Diffusion rates in crystalline ice are extremely slow: below 10^{-18} cm²/s. TPD experiments by Smith and coworkers with binary isotopic ices (D₂O/H₂O and H₂¹⁶O/H₂¹⁸O) found a million-fold increase in the diffusion rate as evidenced by isotopic mixing products [44]. This is indicative of a highly viscous liquid-like state that exists prior to crystallization and may point to a glass transition.

1.1.2 Amorphous Solid Water and Guest Molecule Interactions

The interactions of guest molecules with an ASW matrix are of interest to astrochemists due to the prevalence of ASW mantles on dust grains in the ISM. Other atoms and molecules adsorb and/or become trapped in the ASW coating and can undergo chemical changes in an amorphous ice host. Because of its high porosity, it is facile for molecules to become trapped in ASW and remain in the host matrix until energy is introduced into the system. The degree of porosity is directly related to growth conditions such as temperature and deposition angle. Because ASW is formed at low temperatures that don't allow for movement of molecules to achieve thermodynamic stability, vapor deposition growth of ASW follows the simple model of "hit and stick". When a water molecule adsorbs to a surface that is below 155 K, it doesn't have enough internal energy to rearrange into a thermodynamically favorable structure, so it has a kinetically-determined (random) orientation. More molecules will "hit and stick", forming unique filamentary structures and a porous film. Background deposition of water vapor on a surface that is cooled below 140 K forms a LDA film ($\rho = 0.8 \text{ g/cm}^3$) with a porosity of $\sim 20\%$ [45]. The group of Bruce Kay has shown that directed dosing with a molecular beam can give a range of porosities depending on dosing angle [46, 47]. Samples grown at normal incidence have a maximum density of 0.94 g/cm^3 and are considered to be compact, nonporous ice. In contrast, films grown at extreme glancing angles (86° from normal to the surface) have a maximum porosity of $>80\%$ and minimum density of 0.16 g/cm^3 . At incident angles greater than 45° the average pore size begins to increase along with the increasing porosity. This is due to the growth of "filament" structures that tilt in the direction of dosing and whose spacing increases with increasing incident angle, an effect referred to as "shadowing". As molecules approach the substrate at increasingly oblique angles, filament growth will block a larger segment of the pathway. This model was corroborated with ballistic deposition simulations [46, 48].

The highly porous nature of ASW significantly increases the surface area of ASW with respect to crystalline ice, with as much as 10% of water molecules at pore surfaces.

[49, 50]. Also, the number of dangling $-OH$ groups is much larger for ASW, as evidenced by detection of an absorption peak at $\sim 3700\text{ cm}^{-1}$ [51, 52]. This is in contrast with hexagonal ice, where dangling $-OH$ groups are limited to the surface of the material. The presence of $-OH$ groups encourages uptake of adsorbing materials through van der Waals interactions, and pores provide room for guest species [53].

Thermal processing of ASW with trapped molecules gives rise to explosive release of material during crystallization at 155 K, dubbed the “molecular volcano” [38, 54, 55]. Ejection of guest species is possible at the amorphous-to-crystalline transition due to a relaxation in the ice matrix. Any guest molecules that remain in the film after crystallization remain trapped in the PCI structure until they can codesorb with water at 180 K. Some experimental and theoretical studies have posited that the remaining molecules are trapped in clathrate-hydrate cages within the crystal structure [49, 56].

Nucleation sites and crystal growth has been hotly discussed for the last 20 years, with debate over whether initiation occurs at the substrate, in the bulk, or at the ASW/vacuum interface [39, 57, 58]. Building a nucleation model may be further complicated by different mechanisms for different morphologies [59]. Recent compelling experiments by May and coworkers [60] have made a strong case for crystallization initializing at the surface of ASW films and then propagating down towards the substrate when an ASW sample was heated at a constant rate. A monolayer of Ar was dosed on the substrate surface (graphene) under a 300 ML film of ASW while a monolayer of O_2 was dosed at various levels in the film; TPD experiments were then conducted on the ternary films. The desorption temperature of Ar remained consistent for each film, but the desorption temperature for the O_2 layer increased as the layer was moved deeper in the ASW film. This indicates that cracks initiate at the vacuum interface, propagate downwards and open a pathway for sequential release of the O_2 layer and then the Ar layer. As such, the molecular volcano peak is due to the top-down propagation of cracks during crystallization that initialize at the ASW/vacuum interface. Until this process occurs, many guest species are effectively contained within the water host matrix. This

is significant because molecules can stay in the film above their characteristic desorption temperatures. This has important implications for chemistry in the ISM that will be discussed in the next section of this chapter. Guest molecules may also escape through stress-induced fracturing of the ASW film, in a “bottom-up” mechanism [37, 61]. This occurs when no direct pathway to the surface is available to species that become mobile at low temperatures. With enough heat, the pressure of the trapped species can fracture surrounding ASW and be violently ejected from the matrix. Experiments done by Bar-Nun and associates with cm-thick samples of ASW also saw the ejection of large ice “needles” along with the guest species [37].

A different method of probing ASW with and without guest molecules is using laser radiation to induce photodesorption. One method, originally reported by Livingston and coworkers [62] and put to use in this lab [63], excites the O–H stretch in condensed ASW with $\lambda = 2.94 \mu\text{m}$. This heats the water, resulting in desorption of material from a substrate. The process is very selective to the spatial regime being irradiated due to the limited diffusion of heat during a ns-scale laser pulse and can be used for depth-profiling of an ASW film. Photodissociation of water itself to form H and OH can be achieved with wavelengths $<160 \text{ nm}$. This reaction is believed to be an important source of H_2 in the universe [64]. A third mechanism for laser-induced desorption in ASW films is excitation of a guest molecule. This method was used effectively by Thrower and coworkers [65–67], who investigated benzene-doped ASW samples. They were able to instigate an indirect-adsorbate-mediated desorption process with 250 nm radiation. Even though H_2O has negligible absorbance in this region, benzene was able to efficiently transfer energy to the surrounding ASW film and trigger water codesorption. Such a result implies that a wider range of wavelengths can initiate physical and chemical change in ASW found in the universe.

1.2 Amorphous Solid Water in the Interstellar Medium

The chemistry of the universe is not limited to the surfaces of planets or the interior of stars: much of it occurs in the space between, which is called the interstellar medium (ISM). More than 140 unique molecules have been identified to exist in the interstellar medium by astronomers [1, 2]. This variety of compounds, ranging from diatomics to small organic molecules, seems in contradiction with the low temperatures (<20 K in dense molecular clouds) and molecular density ($\sim 10^4$ atoms/cm³) observed in space [4]. Furthermore, chemistry in the interstellar medium is more complex than can be explained solely from gas-phase processes. The diversity of molecules, which includes organic material and large carbon molecules, is thought to be due to the presence of silicate and carbonaceous “grains” [2, 4, 68, 69]. These grains provide surfaces on which material can interact, and may have been the source of prebiotic organic molecules on Earth [70]. Such grains also play a role in the formation of water in the ISM, which then collects as a mantle on the surface of the grain [23].

Hydrogen and oxygen are among the most ubiquitous atoms in the interstellar medium (first and third most abundant, respectively, with a ratio of $1 : 5 \times 10^{-4}$ [2]), providing ample material for water formation. Specifically, water molecules are generated in dense gas and dust clouds where reactions are facilitated by grains [4, 69]. The gas-phase mechanism is believed to begin with the creation of molecular hydrogen on a dust grain surface. This sublimates quickly and can be ionized by cosmic-ray protons; the H_2^+ ion can then react with another molecular hydrogen to form the triatomic hydrogen ion. This can then react with oxygen to form either OH^+ or H_2O^+ , and the chain continues. In contrast, a solid phase path can occur via diffusive reactions, called the Langmuir-Hinshelwood (LH) mechanism, on the surfaces of dust grains [2, 4, 69]. The exact mechanism and starting materials are debated, but the end product is water ice accretion on the surface of the grain. It is believed that ASW makes up to 70% of surface material on grains in the universe and is mostly high density in structure [3, 23, 71]. While the icy mantle is growing, other molecules can form on the grain through

similar surface reactions and get trapped in the ice. Species believed to be a part of these icy mantles include CO, CO₂, methanol, and polycyclic aromatic hydrocarbons (PAHs) [2, 66, 69]. Over the extremely long lifetime of molecular clouds (10⁶-10⁸ years), ices coating grains are subjected to many different external stresses. For example, dust is bombarded with energetic particles and radiation (e.g. Lyman- α , UV, etc.) from celestial bodies. Such interactions can cause morphological changes, chemical reactions, desorption, or other structural transformations and chemical processing [1, 6]. Laboratory experiments have tried to understand these reactions by studying ASW in model systems under UHV conditions in an effort to mimic the low temperatures and pressures of space.

ASW films can also facilitate reactions between trapped species, as seen in experiments done by Fesneau and coworkers [72]. When acetone and ammonia were co-condensed on a gold-plated surface at 20 K, no reaction between the two species was detected by Fourier transform infrared spectroscopy (FTIR) or mass spectrometry (MS) detection as both products desorbed at their typical desorption temperatures. Adding water to the mixture being condensed resulted in the formation of an aminoalcohol upon heating to 150 K, which was robust even above the water desorption temperature of 185 K. The ASW host matrix traps the reactants above their desorption temperatures, allowing for the reaction to occur when sufficient thermal energy is available. In this way, ASW can act as a medium for the formation of more complex molecules and promote the chemical diversity observed in the ISM.

On the macroscale, ASW covers the surface of certain comets and moons in the outer solar system and beyond [4, 37]. A case that has attracted scientific interest is that of Enceladus, a moon of Saturn. Enceladus has a thick crust of ASW covering its entire surface. During the early phases of the Cassini mission, images were captured that showed "eruptions" of material from the icy surface, similar to volcanoes. These spouts of water, ammonia, and other small molecules have been studied to ascertain a mechanism for these volcanoes and to try and understand what could be happening

beneath the ASW crust. The current theory involves gravitational stress due to the orbit of Enceladus that generates enough heat for a liquid ocean [73–75]. While the planetary scale is vastly different than that in the laboratory, it prompts scientific interest in how heating of buried strata affects ASW.

1.3 $\text{NO}_2/\text{N}_2\text{O}_4$

Previous experiments done in this lab have focused on introducing energy to thin films via the water OH stretch. Subsequent analysis focused on how that energy disrupts the water matrix and was transferred to a dopant species. This method resulted in an irreversible change in the film triggered by a single IR laser pulse that was able to liberate water monomer and small clusters from the solid film. Furthermore, there was preferential release of CO_2 , the dopant, even from the depths of the film because of the relaxation of the host matrix [63].

In contrast, the following dissertation outlines the study of an ASW/ N_2O_4 system where the energy is introduced to the film via exciting an electronic state of N_2O_4 and examining how that energy changes the system. Nitrogen dioxide is a molecule of interest for a few reasons. First of all, it is part of the NO_x family of chemicals that are a key component of pollution from car exhaust and industrial processes. It can interact with solid water in the troposphere and undergo various changes when subjected to radiation (e.g. generating O atoms that react with O_2 to form ozone), and understanding these reactions is extremely important for predicting the impact NO_2 has on the environment [79]. Furthermore, nitrogen compounds have been found in the ISM [80, 81] and may play a role in chemical processing. Most important for our work, it acts as a easy-to-use dopant for introducing energy into a film.

When NO_2 is condensed between 20 K and 140 K, it exclusively forms a stable dimer of the form O_2NNO_2 without any remaining monomer [76]. N_2O_4 readily absorbs in the UV via an electronic transition when adsorbed on a substrate [82, 83], making it an attractive candidate for condensed-phase introduction of heat via laser radiation. As

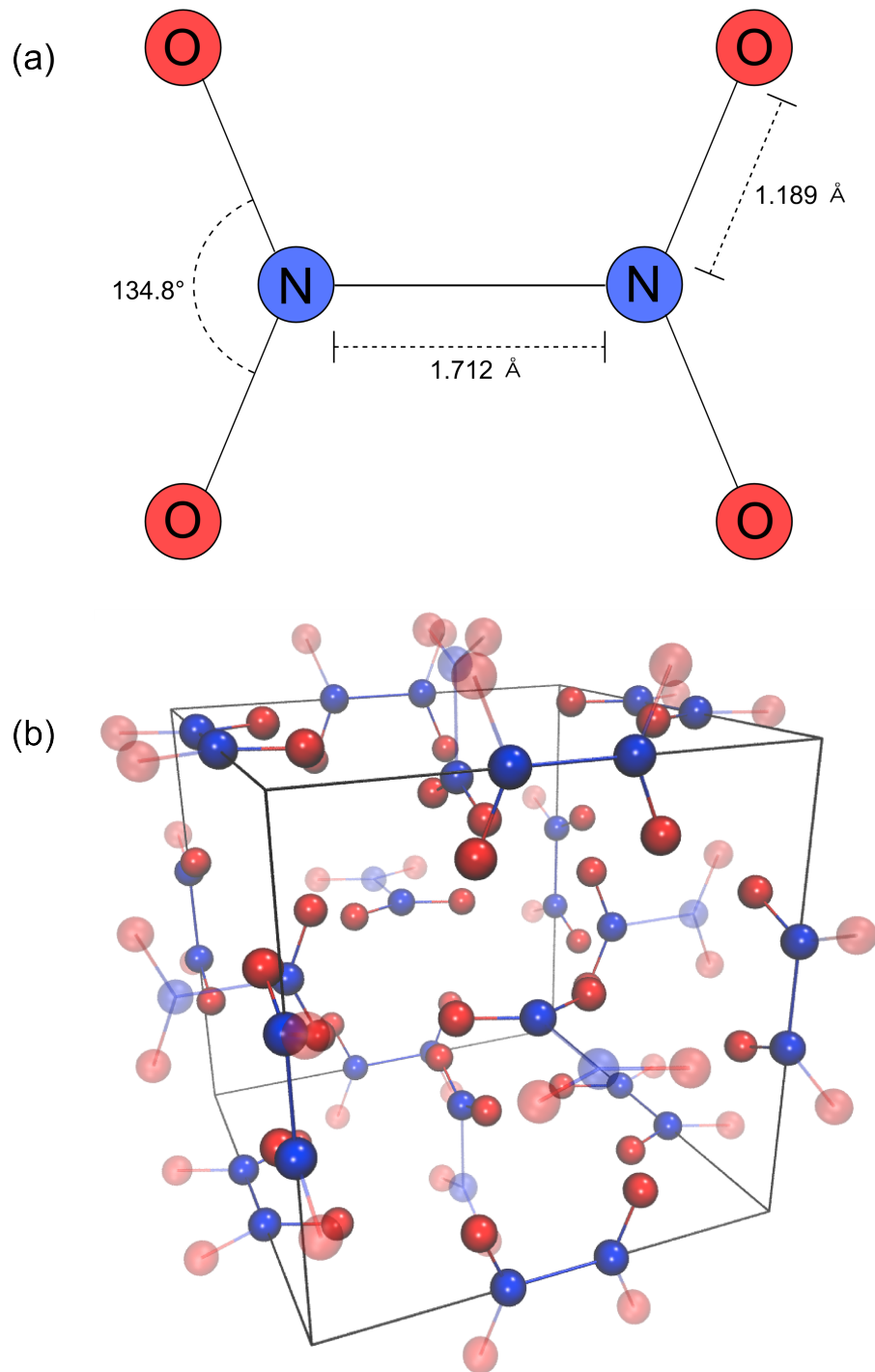


Figure 1.2: (a) Ball-and-stick model of N_2O_4 . The N–N bond is quite weak (around 0.5 eV) [76, 77]. (b) The bcc structure is the dominant structure of crystalline N_2O_4 at low temperatures. Defects, including presence of the NO_2 and unstable isomer ONONO_2 , start to appear below 20 K [78].

the LUMO of N_2O_4 is the N–N antibonding orbital, the weak N–N bond between the NO_2 molecules (~ 0.5 eV [79, 84]) can break apart easily when irradiated (ball-and stick model shown in Figure 1.2a). This forms two excited NO_2 molecules [82, 83]. The NO_2 can then be used to further excite a film with additional UV photons. In this way, a multistep film excitation process is easily attained.

The monolayer structure of N_2O_4 when condensed on a substrate is still under debate. Different groups have found that the monolayer is either ordered [85] or disordered [86]. The bulk structure when condensed from the gas phase has been found to be body-centered cubic and belonging to the space group $T_h^5(Im3)$. The cubic structure is stable down to temperatures of 20 K; below this temperature, amorphous structures, unstable isomers, and the monomer may be present [77, 87]. While the most stable molecular structure of condensed N_2O_4 is that shown in Figure 1.2b, various isomers have been detected by several groups. Bolduan and coworkers [78] found evidence of both the O_2NNO_2 and O_2NONO isomers of N_2O_4 when NO_2 was deposited on a copper substrate at 15 K, whereas only the O_2NNO_2 dimer was detected in films grown at 80 K. When condensed on ASW films, N_2O_4 physisorbs to the H_2O interface in a disordered monolayer without any chemical changes. This is apparent in the low binding energy of 0.40 eV between the N_2O_4 and H_2O [87].

Photodissociation experiments conducted by Dixon-Warren and coworkers of adsorbed NO_2 conducted with UV radiation (193–351 nm) have found two distinct desorption processes that are substrate-dependent [88]. When N_2O_4 is photodesorbed from a metal substrate [in this case Pd(111)], there is a significant “hot” peak that is due to a charge-transfer mechanism from substrate to desorbing molecule. In contrast, photodesorption of N_2O_4 multilayers from an insulator (LiF) results in a dominant slower pathway that is due to direct desorption of the species.

One drawback to spectroscopic investigation of N_2O_4 is its IR absorption spectrum. The IR-active modes of solid N_2O_4 are outside of the range of certain detectors (e.g., InSb), with the highest energy fundamental peak at 1257 cm^{-1} [76]. There are a few

combination bands detectable above 1850 cm^{-1} , but they are extremely weak or can be obscured by water absorption peaks. This can make N_2O_4 difficult to examine with certain FTIR set-ups; this will be discussed more in depth in following chapters.

1.4 Thesis Overview

The research presented in this thesis explores molecular transport using UV radiation in combination with the guest molecule of N_2O_4 to introduce energy to ASW films. A time-of-flight (TOF) mass spectrometer and Fourier transform infrared (FTIR) spectrometer were the main detection tools used. This work presents the following:

- N_2O_4 as an effective guest molecule to introduce energy to ASW in a buried stratum.
- A model that qualitatively describes molecular transport and the induction of fissures in ASW films due to a superheated guest molecule layer.
- A direction for future work that focuses on fissures with well-determined shape and size.

Chapter 2 details the theory behind the experimental methods used, while Chapter 3 describes the specific apparatus used for these experiments. A variety of results characterizing the N_2O_4 /ASW system are presented in Chapter 4. Chapter 5 discusses the introduction of other guest molecules, with a particular focus on D_2O and isotope exchange. Finally, the future direction for these experiments along with preliminary results is covered in Chapter 6.

Chapter References

- [1] Burke, D.; Brown, W. *Phys. Chem. Chem. Phys.* **2010**, *12*, 5947–5969.
- [2] Hama, T.; Watanabe, N. *Chem. Rev.* **2013**, *113*, 8783–8839.
- [3] Angell, C. *Annu. Rev. Phys. Chem.* **2004**, *55*, 559–583.
- [4] Van Dishoeck, E.; Herbst, E.; Neufeld, D. *Chem. Rev.* **2013**, *113*, 9043–9085.
- [5] Kang, H. *Acc. Chem. Res.* **2005**, *38*, 893–900.
- [6] Baragiola, R. *Planet. Space Sci.* **2003**, *51*, 953–961.
- [7] Debenedetti, P. J. *Phys.: Condens. Matter* **2003**, *15*, R1669–R1726.
- [8] Angell, C. *Science* **2008**, *319*, 582–587.
- [9] Malenkov, G. *J. Phys.: Condens. Matter* **2009**, *21*, 283101.
- [10] Rice, S.; Sceats, M. *J. Phys. Chem.* **1981**, *85*, 1108–1119.
- [11] Vega, C.; Abascal, J.; Conde, M.; Aragonés, J. *Faraday Discuss.* **2009**, *141*, 251–276.
- [12] Gandyopadhyay, D.; Mohan, S.; Ghosh, S.; Choudhury, N. *J. Phys. Chem. B* **2013**, *117*, 8831–8843.
- [13] König, H. *Z. Kristallogr.* **1944**, *105*, 279–286.
- [14] Moore, E.; Molinero, V. *Phys. Chem. Chem. Phys.* **2011**, *13*, 20008–20016.
- [15] Poole, P.; Essmann, U.; Sciortino, F.; Stanley, H. *Phys. Rev. E* **1993**, *48*, 4605–4610.
- [16] Johari, G.; Andersson, O. *Thermochim. Acta* **2007**, *461*, 14–43.
- [17] Loerting, T.; Winkel, K.; Seidl, M.; Bauer, M.; Mitterdorfer, C.; Handle, P.; Salzmann, C.; Mayer, E.; Finney, J.; Bowron, D. *Phys. Chem. Chem. Phys.* **2011**, *13*, 8737–8794.
- [18] Limmer, D.; Chandler, D. *PNAS* **2014**, *111*, 9413–9418.
- [19] Fanetti, S.; Pagliai, M.; Citroni, M.; Lapini, A.; Scandolo, S.; Righini, R.; Bini, R. *J. Phys. Chem. Lett.* **2014**, *5*, 3804–3809.
- [20] Chiu, W. *Ann. Rev. Biophys. Biophys. Chem.* **1986**, *15*, 237–257.
- [21] Burton, E.; Oliver, W. *Nature* **1935**, *135*, 505–506.
- [22] Wenzel, J.; Linderstrom-Lang, C.; Rice, S. *Science* **1975**, *187*, 428–430.

- [23] Jenniskens, P.; Blake, D.; Wilson, M.; Pohorille, A. *Astrophys. J.* **1995**, *455*, 389–401.
- [24] Brüggeller, P.; Mayer, E. *Nature* **1980**, *288*, 569–571.
- [25] Mishima, O.; Calvert, L.; Whalley, E. *Nature* **1984**, *310*, 393–395.
- [26] Giovambattista, N.; Stanley, H.; Sciortino, F. *Phys. Rev. Lett.* **2005**, *94*, 107803.
- [27] Tse, J. *J. Chem. Phys.* **1992**, *1992*, 5482–5487.
- [28] Loerting, T.; Salzmann, C.; Kohl, I.; Mayer, E.; Hallbrucker, A. *Phys. Chem. Chem. Phys.* **2001**, *3*, 5355–5357.
- [29] Finney, J.; Bowron, D.; Soper, A.; Loerting, T.; Mayer, E.; Hallbrucker, A. *Phys. Rev. Lett.* **2002**, *89*, 205503(4).
- [30] Brovchenko, I.; Oleinikova, A. *J. Chem. Phys.* **2006**, *124*, 164505.
- [31] Giobambattista, N.; Amann-Winkel, K.; Loerting, T. In *Liquid Polymorphism: Advances in Chemical Physics, Volume 152*, Stanley, H., Ed.; John Wiley & Sons, Inc.: Somerset, NJ, 2013.
- [32] Schober, H.; Koza, M.; Tölle, A.; Masciovecchio, C.; Sette, F.; Fujara, F. *Phys. Rev. Lett.* **2000**, *85*, 4100–4103.
- [33] Essmann, U.; Geiger, A. *J. Chem. Phys.* **1995**, *103*, 4678–4692.
- [34] Loerting, T.; Giovambattista, N. *J. Phys. Condens. Matter* **2006**, *18*, R919–R977.
- [35] Bernal, J.; Fowler, R. *J. Chem. Phys.* **1933**, *1*, 515–548.
- [36] Smith, R.; Petrik, N.; Kimmel, G.; Kay, B. *Acc. Chem. Res.* **2012**, *45*, 33–42.
- [37] Laufer, D.; Bar-Nun, A.; Igal, P.; Jacovi, R. *Icarus* **2013**, *222*, 73–80.
- [38] Smith, R.; Huang, C.; Wong, E.; Kay, B. *Phys. Rev. Lett.* **1997**, *79*, 909–912.
- [39] Dohnálek, Z.; Ciolli, R.; Kimmel, G.; Stevenson, K.; Smith, R.; Kay, B. *J. Chem. Phys.* **1999**, *110*, 5489–5492.
- [40] Mishima, O.; Stanley, H. *Nature* **1998**, *396*, 329–335.
- [41] Smith, R.; Kay, B. *Nature* **1999**, *398*, 788–791.
- [42] Ediger, M.; Angell, C.; Nagel, S. *J. Phys. Chem.* **1996**, *100*, 13200–13212.
- [43] Shephard, J.; Evans, J.; Salzmann, C. *J. Phys. Chem. Lett.* **2013**, *4*, 3672–3676.
- [44] Smith, R.; Huang, C.; Kay, B. *J. Phys. Chem. B.* **1997**, *101*, 6123–6126.

- [45] Raut, U.; Famá, M.; Teolis, B.; Baragiola, R. *J. Chem. Phys.* **2007**, *127*, 204713.
- [46] Dohnálek, Z.; Kimmel, G.; Ayotte, P.; Smith, R.; Kay, B. *J. Chem. Phys.* **2003**, *118*, 364–372.
- [47] Kimmel, G.; Stevenson, K.; Dohnálek, Z.; Smith, R.; Kay, B. *J. Chem. Phys.* **2001**, *114*, 5284–5294.
- [48] Kimmel, G.; Stevenson, K.; Dohnálek, Z.; Smith, R.; Kay, B. *J. Chem. Phys.* **2001**, *114*, 5295–5303.
- [49] Devlin, J. *J. Geophys. Res.* **2001**, *106*, 33333–33349.
- [50] Maté, B.; Rodríguez-Lazcano, Y.; Herrero, V. *Phys. Chem. Chem. Phys.* **2012**, *14*, 10595–10602.
- [51] Mitlin, S.; Leung, K. *J. Phys. Chem. B* **2002**, *106*, 6234–6247.
- [52] Cholette, F.; Zubkov, T.; Smith, R.; Dohnálek, Z.; Kay, B.; Ayotte, P. *J. Phys. Chem. B* **2009**, *113*, 4131–4140.
- [53] Ayotte, P.; Smith, R.; Stevenson, K.; Dohnálek, Z.; Kimmel, G.; Kay, B. *J. Geophys. Res.* **2001**, *106*, 33387–33392.
- [54] Kumi, G.; Malyk, S.; Hawkins, S.; Reisler, H.; Wittig, C. *J. Phys. Chem. A* **2006**, *110*, 2097–2105.
- [55] May, R.; Smith, R.; Kay, B. *J. Phys. Chem. Lett.* **2012**, *3*, 327–331.
- [56] Faizullin, M.; Vinogradov, A.; Koverda, V. *Chem. Eng. Sci.* **2015**, 000–000.
- [57] Kondo, T.; Kato, H.; Bonn, M.; Kawai, M. *J. Chem. Phys.* **2007**, *127*, 094703.
- [58] Backus, E.; Grecea, M.; Kleyn, A.; Bonn, M. *Phys. Rev. Lett.* **2004**, *92*, 236101.
- [59] Safarik, D.; Mullins, C. *J. Chem. Phys.* **2004**, *121*, 6003–6010.
- [60] May, R.; Smith, R.; Kay, B. *J. Chem. Phys.* **2013**, *138*, 104501.
- [61] May, R.; Smith, R.; Kay, B. *J. Chem. Phys.* **2013**, *138*, 104502.
- [62] Livingston, F.; Smith, J.; George, S. *Anal. Chem.* **2000**, *72*, 5590–5599.
- [63] Rebolledo–Mayoral, O.; Stomberg, J.; McKean, S.; Reisler, H.; Wittig, C. *J. Phys. Chem. C* **2012**, *116*, 563–569.
- [64] Yabushita, A.; Kanda, D.; Kawanaka, N.; Kawasaki, M.; Ashfold, M. *J. Chem. Phys.* **2006**, *125*, 133406.

- [65] Thrower, J.; Burke, D.; Collings, M.; Dawes, A.; Holtom, P.; Jamme, F.; Kendall, P.; Brown, W.; Clark, I.; Fraser, H.; McCoustra, M.; Mason, N.; Parker, A. *Astrophys. J.* **2008**, *673*, 1233–1239.
- [66] Thrower, J.; Collings, M.; McCoustra, M.; Burke, D.; Brown, W.; Dawes, A.; Holtom, P.; Kendall, P.; Mason, N.; Jamme, F.; Fraser, H.; Clark, I.; Parker, A. *J. Vac. Sci. Tech.* **2008**, *26*, 919–924.
- [67] Thrower, J.; Abdulgalil, A.; Collings, M.; McCoustra, M.; Burke, D.; Brown, W.; Dawes, A.; Holtom, P.; Kendall, P.; Mason, N.; Jamme, F.; Fraser, H.; Rutten, F. *J. Vac. Sci. Technol., A* **2010**, *28*, 799–806.
- [68] Draine, B. *Annu. Rev. Astron. Astrophys.* **2003**, *41*, 241–289.
- [69] Herbst, E. *AIP Con. Proceed.* **2013**, *1543*, 15–30.
- [70] Chyba, C.; Sagan, C. *Nature* **1992**, *355*, 125–132.
- [71] Tielens, A.; Hagen, W. *Astron. Astrophys.* **1982**, *114*, 245–260.
- [72] Fresneau, A.; Danger, G.; Rimola, A.; Theule, P.; Duvernay, F.; Chiavassa, T. *MNRAS* **2014**, *443*, 2991–3000.
- [73] Hansen, C.; Shemansky, D.; Esposito, L.; Stewart, A.; Lewis, B.; Colwell, J.; Hendrix, A.; West R.A., W. J.; J.H. Teolis, B.; Magee, B. *Geophys. Res. Lett.* **2011**, *38*, L11202.
- [74] Porco, C.; DiNino, D.; Nimmo, F. *Astron. J.* **2014**, *148*, 45.
- [75] Hurford, A.; Helfenstein, P.; Hoppa, G.; Greenberg, R.; Bills, B. *Nature* **2007**, *447*, 292–294.
- [76] Andrews, B.; Anderson, A. *J. Chem. Phys.* **1981**, *74*, 1534–1537.
- [77] Kvick, Å.; McMullan, R.; Newton, M. *J. Chem. Phys.* **1982**, *78*, 3754–3761.
- [78] Bolduan, F.; Jodl, H.; Loewenschuss, A. *J. Res. Nat. Bur. Stand. A* **1976**, *80A*, 143–166.
- [79] Bass A.M. and Ledford Jr., A.; Laufer, A. *J. Res. Nat. Bur. Stand. A* **1976**, *80A*, 143–166.
- [80] McGonagle, D.; Ziurys, L.; Irvine, W.; Minh, Y. *Astrophys. J.* **1990**, *359*, 121–124.
- [81] Halfen, D.; Apponi, A.; Ziurys, L. *Astrophys. J.* **2001**, *561*, 244–253.
- [82] Bach, W.; Breuer, H. *Faraday Discuss. Chem. S.* **1974**, *58*, 237–243.

- [83] Kawasaki, M.; Kasatani, K.; Hiroyasu, S.; Shinohara, H.; Nobuyuki, N. *Chem. Phys.* **1983**, *78*, 65–74.
- [84] Hisatsune, I. *J. Phys. Chem.* **1961**, *65*, 2249–2253.
- [85] Rieley, H.; Colby, D.; McMurry, D.; Reeman, S. J. *Phys. Chem. B* **1997**, *101*, 4982–4991.
- [86] Yabushita, A.; Inoue, Y.; Senta, T.; Kawasaki, M.; Sato, S. *J. Chem. Phys. A* **2004**, *108*, 438–446.
- [87] Rieley, H.; McMurry, D.; Haq, S. *Faraday Trans.* **1996**, *92*, 933–939.
- [88] Dixon-Warren, S. J.; Jackson, R.; Polanyi, J.; Rieley, H.; Shapter, J.; Weiss, H. J. *Phys. Chem.* **1992**, *96*, 10983–10994.

Experimental Methods

This chapter gives a brief summary of concepts relevant to the experiments. The information presented here will give context to results in later chapters and summarize the theory behind key experimental apparatus detailed in Chapter 3.

2.1 Time-of-Flight Mass Spectrometry

Mass spectrometry (MS) was first implemented using sector mass spectrometers. These required careful alignment and machining to ensure that the material of interest was directed along the correct path. Size restrictions existed because of the use of magnetic fields. By exploiting the Lorentz force law, material within a magnetic (or electric) field is deflected different amounts based on their mass-to-charge ratio, m/q . Mass spectrometers using electric fields were initially limited by design flaws that limited mass resolution. In 1955, Wiley and McLaren described an improved two-stage time-of-flight system that was able to collect mass spectra quickly and efficiently. This allowed for increased mass resolution and detection of a range of masses in a short time, which paved the way for its widespread use in laboratories [1]. Because of its ease of use, mass spectrometry has been utilized in a variety of applications: matrix-assisted laser desorption-ionization (MALDI), chromatography, electrospray ionization systems, fragment characterization, etc. [2].

Time-of-flight (TOF) MS exploits the relationship between mass and energy such that molecules of different masses can be separated out and detected. An example of a two-stage system is diagrammed in Figure 2.1.

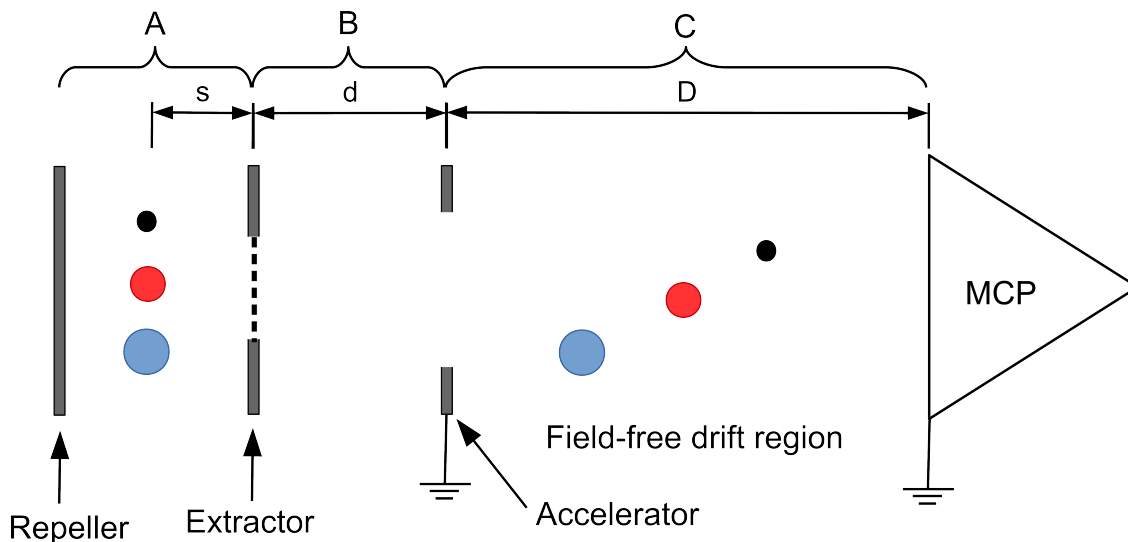


Figure 2.1: A schematic of a linear two-stage Wiley-McLaren TOFMS system. Material enters the region between repeller and extractor plates initially kept at the same voltage (A). If necessary, the material is ionized (this can be done by electron impact ionization, photoionization, etc). Subsequently, the voltage is dropped on the extractor plate and ionized material is extracted and further accelerated by a grounded third plate into a field-free drift region (C). Ionized material of different masses can be differentiated by flight times, with more massive ions arriving after lighter ions (relative mass is indicated by size in the diagram).

Molecules of interest enter a region between two plates, referred to as a “repeller” and an “extractor.” Because of the nature of TOFMS, detected material must be ionized: either material enters the the extraction region as ions, or it is ionized in that region; common ionization techniques include photoionization and electron impact bombardment. Then, an electric field accelerates ions to a field-free region. The accelerating pulse ensures that ions leave the electric-field region with the same kinetic energy. This results in the ions having velocities that are a function of their charge (q) and mass (m). Given sufficient drift time, the ions separate according to the relationship m/q and are collected by a detector. This relationship between mass and drift time can be

defined mathematically for the two-stage TOFMS system depicted in Figure 2.1, which is a schematic of the approach used in this dissertation. The advantage of a two-stage system will be addressed in Section 2.1.2.

Particles enter the ionization region with an initial kinetic energy, U_0 . There, material is ionized via an ionization process, which is electron impact ionization for our apparatus. The ions gain kinetic energy proportional to the distance it travels in an electric field. As such, we can state the total kinetic energy of a charged particle in a two-stage TOF system as

$$U_{\text{tot}} = U_0 + qsE_s + qdE_d \quad (2.1)$$

where s and d are the path lengths in the ionization and acceleration regions (A and B in Figure 2.1, respectively) and E_s and E_d are the magnitudes of the electric fields in those regions. There is no term representing the drift region (C in Figure 2.1) because it is field free, and thus does not contribute kinetic energy. Time can be introduced by using

$$\text{K.E.} = \frac{1}{2}mv^2 = \frac{1}{2}m \left(\frac{d}{t} \right)^2 \quad (2.2)$$

where m is the mass of the particle, v is the velocity of the particle, and t is the flight time in a specific region. In this way, the flight time for a charged particle in TOFMS is defined as

$$T(U_0, s) = T_s + T_d + T_D \quad (2.3)$$

Therefore, each ion with a unique m/q will have a characteristic flight time, where each flight time term can be defined with respect to its mass, travel distance, and kinetic energy.

Because of the relationship between time and mass inherent in Equation 2.2, each component in Equation 2.3 will have a $\sqrt{m/q}$ term. Therefore, the total flight time of a particle is proportional to the square root of its mass-to-charge ratio, with constants dependent on the factors of a specific system. Combining this relationship with parameters of a specific TOF instrument, a mass spectrum can be measured quickly and easily with high resolution. Furthermore, it is possible to detect a range of masses all at once

instead of selecting one mass at a time for detection as with other instruments, such as quadrupole mass analyzers. A system can be set up to collect entire mass spectra in very short time windows with fast triggering of the ionization-extraction electronics. The work detailed in this dissertation employs this method in order to investigate a plume of material as it evolves in time; the specifics of the arrangement are described in Chapter 3, Section 3.5.

2.1.1 Jacobian

When converting a time-of-flight spectrum to a mass spectrum, it is necessary to use a Jacobian transformation. This is because when solving for mass in the aforementioned relationship, there is a t^2 term. Thus, when converting from time space to mass space, a Jacobian transformation is required to ensure that the peak areas remain the same. The equation used to get a good fit with data in the time domain is as follows:

$$m = At^2 + Bt + C \quad (2.4)$$

where A , B , C are fitting parameters. The B and C terms are very small, indicating that deviations from the theoretical relationship between t and \sqrt{m} are minor. While it may appear that a direct conversion from time to mass is possible, it is important to note that data collected is *signal per unit time* [3]. If a direct conversion was carried out, the intervals in the time-of-flight spectrum would not be evenly spaced in the mass spectrum. Thus, we employ the following relationship

$$f(t)dt = g(m)dm \quad (2.5)$$

By using this relationship in conjunction with Equation 2.4, we can determine the term needed to perform a Jacobian transformation.

$$\frac{dm}{dt} = 2At + B \quad (2.6)$$

$$g(m) = f(t) \frac{dt}{dm} = f(t) \frac{1}{2At + B} \quad (2.7)$$

2.1.2 Resolution

The above relationship between flight time and m/q is true for an idealized “point” ionization and assumes that the material has the same initial kinetic energy while traveling in the same direction. In an ideal TOFMS, there is an ionization “region” where only material ionized at the center with no other deviations will follow Equation 2.3 exactly. Our system further confounds the ideal scenario as molecules desorb with various trajectories and kinetic energies. Because of this, there is a range of possible kinetic energies for each mass, which will result in ions of the same m/q ratio arriving at the detector at slightly different times. The distribution of flight times results in a broadening of mass peaks which limits the mass resolution. The three factors affecting TOFMS resolution are due to time, space, and kinetic energy distributions of the ionized material [2]. Each of these come into play in our experimental approach, and as such will be described briefly herein.

Time distributions occur when ions of the same mass form at different times with the same kinetic energy. This can happen because material in a Wiley-McLaren TOFMS is ionized for a specific amount of time, t_i , and desorbing material can enter the ionization region at any time during this window. Because of this, ionized particles will travel through the drift region with a discrete time difference. Mass resolution is defined by the following equation:

$$\frac{\Delta m}{m} = \frac{2\Delta t}{t} \quad (2.8)$$

This relationship can be exploited to increase mass resolution by increasing the flight time, which is done with low accelerating voltage and/or long drift path lengths.

The afore-mentioned ionization region contributes to spatial distribution of ions. For instance, given a rectangular ionization region as shown in Figure 2.2, ions will be extracted from the entire width of the rectangle, l . Based on Equation 2.1, material in the ionization region that is closest to the extractor grid will gain less kinetic energy than material located at the other extreme of the ionization region. Clearly this spread of kinetic energies due to the ionization region width, l , will give a range of flight times.

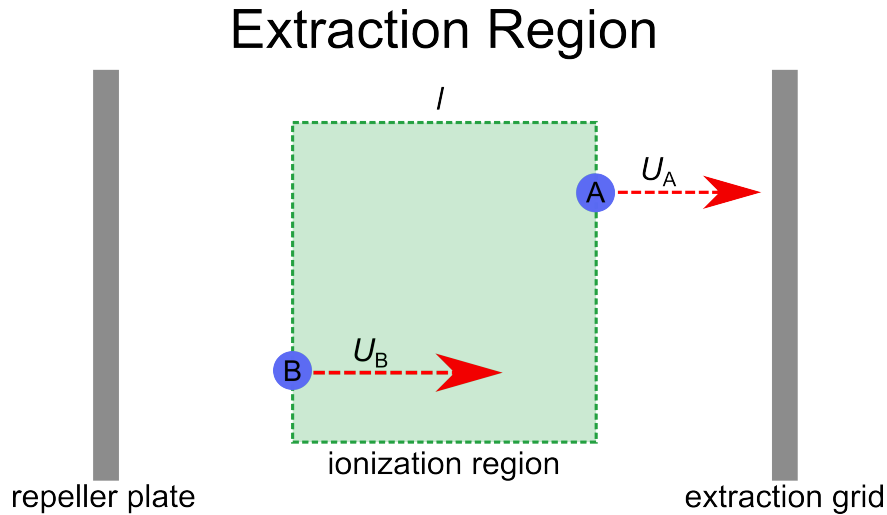


Figure 2.2: Two particles of the same mass, A and B, are ionized in a finite ionization region with a width of Δl . The flight path can therefore differ by a range of $\pm\Delta l/2$; in this case, particle A will have a shorter flight path than particle B. However, particle B will gain more kinetic energy than particle A. This means that there will be a point in space where particle B will pass particle A.

However, the difference in flight path distances must be taken into account. Ions leaving the extraction region with the least kinetic energy will have a flight path of length D_0 ; ions leaving the extraction region with the most kinetic energy will have a flight path of length $D_0 + l$. Since ions with more kinetic energy have a longer flight path, their flight time will be increased accordingly. Furthermore, this results in a point along the flight path where more energetic ions will pass less energetic ions; this is referred to as space focusing. In a well-designed system, this point (referred to as the *space focus plane*, which is independent of mass) occurs at the detector so as to minimize the effect of a finite ionization region. However, the location of this plane in a one-stage system is fixed at a short distance from the extraction region, resulting in a short drift time and poor mass resolution. A two-stage system addresses this issue by adding a second extraction region, which allows for the location of the space focus plane to be chosen by careful selection of extraction and repeller plate voltages [2, 4].

Another way that a range of kinetic energies can be introduced is via the initial velocity distribution of particles in the ionization region. This is a contributing factor

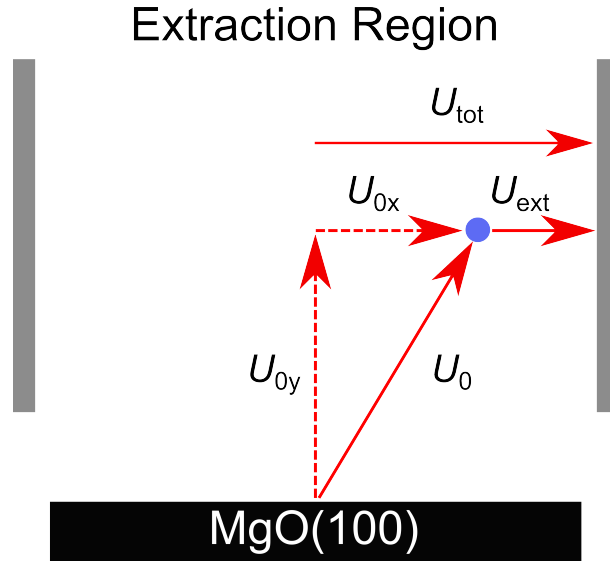


Figure 2.3: A particle trajectory, depicted as a blue circle, with initial kinetic energy U_0 . Only the component in the direction of extraction will affect the overall kinetic energy of the extracted particle, U_{tot} .

in the system discussed by this dissertation as material is leaving a surface with a wide range of velocities. When a particle enters the ionization region with a nonzero velocity, the kinetic energy component in the direction of the direction of extraction will contribute to the total kinetic energy of the particle; this is diagrammed in Figure 2.3. Thus, the total kinetic energy of the particle when it leaves the ionization region will be a sum:

$$U_{\text{tot}} = U_{\text{ext}} + U_{0x} \quad (2.9)$$

Instead of kinetic energy only being imparted by the extraction process, U_{ext} , the initial kinetic energy component along the extraction trajectory, U_{0x} , also contributes. The variation in U_{0x} will result in a range of U_{tot} values. This issue is hard to address in a linear TOFMS as increasing drift length increases peak width. Ions can also have trajectories in the opposite direction of the extraction path, which means that while they will be accelerated to the same kinetic energy as other ions of the same mass, they will have a longer flight time because of their turn-around time in the extraction region.

An additional issue that is particularly relevant to this work is that of velocity distributions affecting velocity resolution. The approach used for experiments described herein allows for multiple complete TOF spectra to be taken in quick succession; this process will be discussed in more detail in the following chapter. A rough approximation of material velocity can be made by using the extraction time (which is in increments of 10 μs) in conjunction with the 2.5 cm flight path from the substrate to the ionization region. However, there are two obfuscating factors: the finite dimensions of the ionization region (Figure 2.2) and the temporal length of the ionization process. The former case will be discussed first. The ionization region in our TOFMS has a length of ~ 1.2 cm along the path from the substrate to the ionization region. Therefore, the flight path of material that is detected in a single extraction can range from 1.9-3.1 cm. For the 10 μs extraction, the velocity spread is 1200 m/s. The second confounding factor is the process of ionization. It is not instantaneous: our apparatus is set to ionize material for 7 μs . As such, the material in the 10 μs extraction has a range of flight times (3-10 μs) that result in a velocity spread of ~ 5800 m/s assuming an average flight path of 2.5 cm. Thus, calculated velocities of material arriving in each extraction of our pulsed TOFMS system are only a rough approximation.

2.2 Laser-Induced Desorption

Using lasers to remove material from surfaces has a wide variety of applications in many different fields, such as medicine, material sciences, and astrophysics [5–7]. Referred to as laser ablation or laser-induced desorption (LID), this process can elucidate relationships between materials on a molecular level. By carefully choosing a wavelength that excites a material of interest, energy can be introduced to that material via laser radiation. This can result in removal of material, transfer of energy to non-absorbing species, extreme heating of the substance, dissociation and/or reaction of the material [8]. Several theories have been put forth with respect to a mechanism for ablation, and the debate continues; some of the most popular models will be presented in this

section. While there isn't a quantitative match between the material presented in this section and results reported in Chapters 4 and 5, qualitative descriptions are valuable for interpreting trends. It should be noted that ablation and desorption are used interchangeably by some groups, but differentiated by others. In the latter case, ablation refers to a more violent removal of material than desorption; an attempt will be made to keep language used by the literature discussed consistent.

A model for the effects of laser ablation was first suggested by J. F. Ready in 1965 [9]. It presented a quantitative look at heat transfer in metals and posited that there was a different mechanism for long and short laser pulses. While these calculations were based on very high laser intensities ($\sim 10^8$ W/cm² compared to ≤ 10 W/cm² for our approach), the findings are instructive to discuss. One of the most impressive results from the derived equations was the extreme temperature gradients ($\sim 10^8$ deg/cm) that could be induced on short time scales (10^{10} deg/s) with laser heating. Also, the shape of the laser pulse was found to have a significant effect: shorter, higher power pulses resulted in a higher surface temperature than a longer, lower pulse of the same total energy. Instead, the latter pulse would result in a smaller temperature gradient and a larger penetration depth. Another result of interest is that as thermal conductivity of the material decreases, the peak surface temperature increases with a decreased depth of penetration.

Laser ablation, with a particular focus on ultraviolet matrix-assisted desorption processes (UV-MALDI), has been modelled in the microscale by Zhigilei and Garrison [10–12]. They utilized a “breathing sphere” model that approximates internal degrees of freedom to allow for internal energy conversion to translational motion. A differentiation between desorption and ablation is made: desorption is defined as a process where chiefly monomers desorb from a surface, whereas ablation results in larger clusters of material being released via photoabsorption. It is possible to move from the desorption regime to the ablation regime by increasing laser fluence; the crossover point in these simulations was at 0.7 mJ/cm². However, the fraction of small clusters and monomers

will *increase* in the ablation regime with increasing laser fluence, so they are not only indicative of a desorption mechanism.

The overall ablation process is as follows. Laser radiation tuned to excite molecules in a film is absorbed. This energy quickly degrades to heat in the form of translational motion. However, the temperature rises faster than the system can mechanically relax, so there is a significant increase in pressure. Once the pressure gradient exceeds the mechanical strength of the material, individual molecules and/or clusters are ejected. Rapid heating of the confined material can force the material to temperatures above the boiling point. This can result in a “phase explosion”, where the excited material is quickly converted to a hot, gaseous fluid. Such a phase explosion contributes additional pressure to the system that has already experienced heating at constant volume.

There were a few notable trends in the molecular dynamics (MD) simulations of laser ablation [11]. The average velocity decreased in relation to the depth of the plume, indicating that collisions play a significant role in the redistribution of energy as material is ablated. This leads to a range of “stream velocities” that require an adjusted Maxwell-Boltzmann distribution to properly account for. Non-absorbing species (in this case, analyte molecules) have a similar average velocity to the absorbing species (matrix molecules). This follows from the phenomenon of entrainment, which has been experimentally observed by several groups [13–15].

An opposing view of laser ablation put forth by Perez and coworkers [16] challenges the existence of a phase explosion. They argued that while phase explosion, deemed “nontrivial” fragmentation, is possible with ultrashort laser pulses (\leq ps scale), nanosecond pulses cannot trigger such a transformation. Instead, a slower expansion of material and efficient thermal conduction inhibit this process and ablation causes a “trivial” fragmentation.

Their MD simulations used classical Lennard-Jones potential interactions and “carrier” atoms that absorb energy (photons) and transfer it to surrounding material. Modelling a 4 μ m-thick sample ablated with a 2.5 ns pulse, they found 3 unique regions

within the film where effects were dominated by the amount of inertial confinement. At the surface, a region of weak inertial confinement, material is free to expand into vacuum when irradiatively heated. The material can pass the melting point into a supercritical state that generates void nucleation and subsequent clusters (trivial fragmentation) [17, 18]. Farther down in the heated film, homogeneous nucleation occurs during isochoric heating and triggers a phase explosion (though different in character to that described by Zhigilei). In the depths of the material, thermal diffusion from effective cooling begins to hamper expansion. In this region, heterogeneous nucleation is the dominant mechanism that results in the ejection of thick pieces of material (hundreds of nm).

Adsorbate desorption mechanisms fall into two categories: thermal and nonthermal [19]. Thermal mechanisms are due to irradiative heating and the detected signal pattern reflects those seen in temperature-programmed desorption. It has a Maxwell-Boltzmann shape, is sensitive to surface temperature, and has a long tail. Nonthermal mechanisms are due to photoprocesses and are independent of surface temperature. A combination of these mechanisms results in the removal of material. The process studied in this dissertation differs from the typical ablation system. Instead of homogeneously heating a sample with laser radiation, the goal of experiments detailed in this dissertation was to implant energy in a spatially selective way. Specifically, a layer embedded within a film absorbs radiation, which decays to heat in picoseconds. Heat can then transfer to surrounding material. Furthermore, a pressure gradient may be introduced depending on if a phase change occurs within the absorbing region. As such, the processes involved will not result in simple removal of material from the surface and cannot easily be described by typical ablation mechanisms. The proposed mechanism for our system will be described in detail in Chapters 4 and 5.

Chapter References

- [1] Wiley, W.; McLaren, I. *Rev. Sci. Instrum.* **1955**, *26*, 1150–1157.
- [2] *Time-of-Flight Mass Spectrometry*; Cotter, R. J., Ed.; American Chemical Society: 1994.
- [3] Mooney, J.; Kambhampati, P. J. *Phys. Chem. Lett.* **2013**, *4*, 3316–3318.
- [4] Guilhaus, M. *J. Mass. Spectrom.* **1995**, *30*, 1519–1532.
- [5] Edwards, G. *Laser Photonics Rev.* **2009**, *3*, 545–555.
- [6] Lippert, T. *Plasma Process. Polym.* **2005**, *2*, 525–546.
- [7] Livingston, F.; Smith, J.; George, S. *Anal. Chem.* **2000**, *72*, 5590–5599.
- [8] Ho, W. In *Desorption Induced by Electronic Transitions*, Betz, G., Varga, P., Eds.; Springer-Verlag: Berlin, 1990.
- [9] Ready, J. J. *Appl. Phys.* **1965**, *36*, 462–468.
- [10] Zhigilei, L.; Kodali, P.; Garrison, B. *Chem. Phys. Lett.* **1997**, *276*, 269–273.
- [11] Zhigilei, L.; Kodali, P.; Garrison, B. *J. Phys. Chem. B* **1998**, *102*, 2845–2853.
- [12] Zhigilei, L.; Garrison, B. *Rapid Commun. Mass Sp.* **1998**, *12*, 1273–1277.
- [13] Beavis, R.; Chait, B. *Chem. Phys. Lett.* **1991**, *181*, 479–484.
- [14] Huth-Fehre, T.; Becker, C. *Rapid Commun. Mass Sp.* **1991**, *5*, 378–382.
- [15] Pan, Y.; Cotter, R. *Org. Mass Spectrom.* **1992**, *27*, 3–8.
- [16] Perez, D.; Lewis, L.; Lorazo, P.; Meunier, M. *Appl. Phys. Lett.* **2006**, *89*, 141907.
- [17] Lorazo, P.; Lewis, L.; Meunier, M. *Phys. Rev. Lett.* **2003**, *91*, 225502.
- [18] Perez, D.; Lewis, L. *Appl. Phys. A* **2004**, *79*, 987–990.
- [19] Chuang, T. *Surf. Sci. Rep.* **1983**, *3*, 1–105.

Experimental Apparatus

Now that a review of the relevant experimental methods has been dispensed with, this chapter describes how each concept is put into practice for data collection. The experimental chamber is discussed first, followed by a description of sample preparation, and finally details about the instruments and methods used for each experimental technique are provided.

3.1 Ultra-High Vacuum System

All experiments were carried out in a 3-tier stainless steel ultra-high vacuum (UHV) chamber that can reach pressures of $<3 \times 10^{-10}$ Torr. This ensures high sample quality, as monolayer formation from background gases takes several hours under these conditions. Chamber pressure is monitored using a nude ion gauge (Granville-Phillips 330). The chamber is pumped using a turbomolecular pump (Leybold TurboVac, 600 L/s) that is backed with a mechanical roughing pump (Welch Model 1397). The 3 tiers are structured such that different experimental analyses can be carried out in different levels of the chamber. The top tier (labeled Tier 3 in Figure 3.1), where the surface manipulator is attached to a gate valve (MDC GV-4000M), is set up to accommodate FTIR spectroscopy and TPD experiments. It includes a residual gas analyzer (SRS RGA 300) and has two ports with calcium fluoride (CaF_2) windows to accommodate the path of the IR beam from an FTIR spectrometer to an external detector (LN_2 -cooled Nicolet InSb

detector). The main part of the chamber is divided into upper and lower sections (Tier 2 and Tier 3, respectively), where the upper section is used for laser-induced “eruption” experiments detailed in this dissertation. Tier 2 includes a window for introducing laser radiation, two leak valves (MDC ULV-150), as well as a linear time-of-flight mass spectrometer. Tier 3 was previously used for molecular beam scattering experiments, but is no longer in use. It houses a third leak valve that is used for dosing additional test species during film growth.

To maintain UHV pressure after introduction of water to the chamber, which sticks to the stainless steel walls and raises the base pressure of the system through outgassing, the chamber had to be “baked” at regular intervals (bake-out temperatures can be found in the appendix of reference [1]). This was done with heating tape that was wrapped around the chamber and controlled with variable transformers (Staco-Variac 3PN1010). The temperature of the chamber was raised to $\sim 110^\circ\text{C}$ for 2-3 days; the temperature was monitored with K-type thermocouples that were attached at various points on the chamber. In order to maintain low pressure during the week, a heat lamp (Osram 650 W, Model 64535) installed inside the chamber and plugged into a Variac was left on during the night to speed up outgassing.

3.2 Surface Manipulator

The top tier of the UHV chamber is equipped with a surface manipulator that is attached to an xyz translational stage and enables rotation in the xy -plane (Kurt Lesker, modified by McAllister Technical Services and repaired by VG). It has a 600 mm range in the z direction (VG Omniax Translator, z slide module) and a 25 mm range in both the x and y directions (VG Omniax Translator, xy stage module). Furthermore, it can rotate 360° around the z -axis via a differentially-pumped feedthrough system (VG Rotary Feedthrough, DPRF 25H). The manipulator consists of a sheathed stainless steel reservoir that is silver-brazed to a copper block to which the sample holder is attached, shown in Figure 3.2. Liquid nitrogen is poured into this reservoir, which is open to

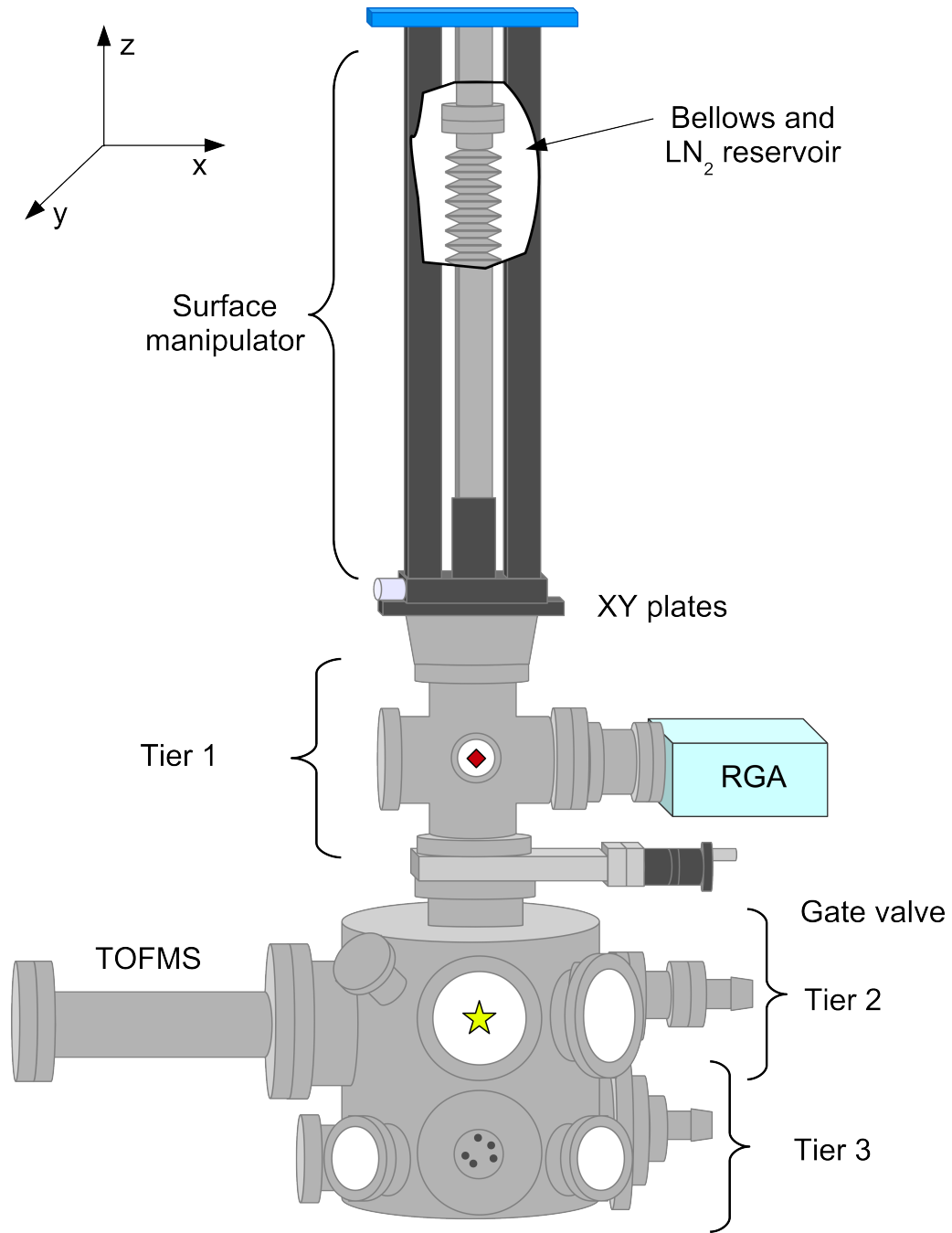


Figure 3.1: An external view of the UHV chamber (not to scale). Key sections are labeled. The surface manipulator provides xyz translation capabilities. The window through which UV radiation enters for a typical experiment is designated with a star. The diamond indicates the FTIR pathway.

atmosphere on one end, to achieve cryogenic temperatures of <110 K. With good thermal contact between the copper block and surface holder, temperatures as low as 96 K are possible. Even lower temperatures can be reached by bubbling helium through the liquid nitrogen. Using this method, surface temperatures of ~ 90 K can be reached.

3.3 Surface Holder and MgO Surface

The surface holder consists of two machined pieces of copper and a piece of copper foil that holds the MgO(100) surface, which are diagrammed in Figure 3.2. The two pieces of machined copper are attached to the copper block at the end of the stainless steel liquid nitrogen reservoir by three screws. Ceramic washers (McAllister Technical Services, size 4-40) and a ceramic spacer (USC machine shop, dimensions given in reference [1]) ensure that the two sides are electrically isolated from each other. A sapphire disc (Esco Products, 0.040 in. thick, 0.75 in. diam.) is sandwiched between the machined pieces and the copper block at the end of the surface manipulator. The disc acts as an electrical insulator and a “thermal switch”. The thermal conductivity of sapphire increases as its temperature decreases, peaking around 30 K [2]. This allows for efficient cooling of the surface by the LN₂ reservoir. In contrast, heating is also efficient as the thermal conductivity of the sapphire drops dramatically while it is heated, which thermally isolates the hot surface from the cold copper block. This is necessary to ensure that the surface can be heated effectively via a tantalum wire; this heating method will be described later.

The copper foil (ESPI Metals, 0.012 in. thick) was cut to roughly 14×10 mm, with an arm extending along the length of the substrate that could be bent around an arm of one of the machined copper pieces. A 6×6 mm opening was cut in the foil to allow radiation to pass through the MgO surface once it was in the holder; this was necessary for performing transmission FTIR experiments. This holder design was adjusted from a previous design to ameliorate a thermal gradient on the surface [3]. The side of the substrate nearest the copper arm in contact with the LN₂ reservoir was several Kelvin

cooler than the far side, resulting in a “cold” side of the surface and a “hot” side of the surface. By extending the arm of the holder along an entire side of the MgO surface instead of having an arm that only extended halfway along the side, the temperature gradient was reduced significantly. While increasing the amount of material used for the surface holder could slow heating and cooling times, no significant change in either were noted after the design change.

A length of tantalum wire (ESPI Metals, 0.015 in. diam.) was glued to the back of the holder with ceramic glue (Aremco 835M), encircling the window, which acts as a heater. The wire was encased in segments of ceramic rod (Omega ORX-020132) to prevent shorting of the circuit. The ends of the wire were inserted in small holes in the machined copper pieces (Figure 3.2) and secured with small stainless steel screws. Electrical current can be introduced to the wire through two leads that are attached to the machined copper pieces. Outside the chamber, ~ 8 A are provided from a power supply (Hewlett-Packard 6259B) for rapid resistive heating. With this arrangement, temperatures from 90-600 K can be reached.

MgO(100) was chosen as a substrate because it transmits $>80\%$ of radiation between $2,000\text{--}30,000\text{ cm}^{-1}$, which enables transmission FTIR spectroscopy. The MgO(100) substrate was prepared by cleaving it on both sides from a larger piece ($10 \times 10 \times 300$ mm, fine-ground polish, MTI Corporation) in dry air to obtain a fresh, smooth surface. This was later verified by atomic force microscopy (AFM), as shown in Figure 3.3. Polished surfaces are undesirable for an experimental substrate because small amounts of foreign material are left behind by the polishing process. The MgO substrate was clamped in the copper foil, and a K-type thermocouple was affixed using ceramic glue to the “hot” side opposite the arm that attaches to the copper holder. This ensured that temperature measurements were an upper bound.

After a fresh surface is made, it is left with oxygen vacancies. These vacancies are filled once the surface has been installed in the UHV chamber by adding an oxygen atmosphere of 10^{-7} Torr and heating the surface to 600 K for 1 hour. If this is not done,

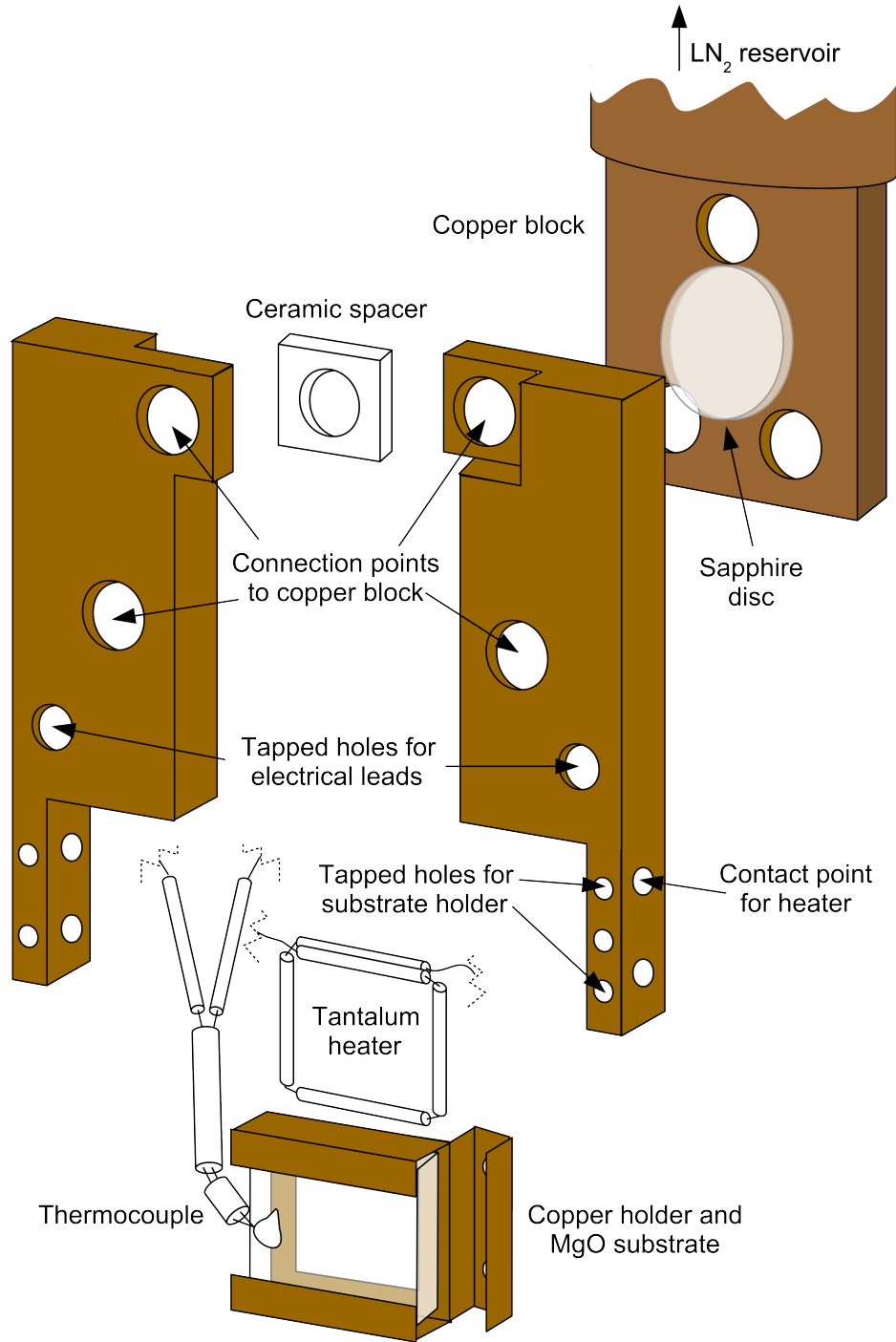


Figure 3.2: An exploded view of the substrate holder and associated components. Two machined copper pieces are electrically isolated from each other by a custom ceramic spacer and attached to the copper block with long screws fixed with flat and ceramic hat washers on each side. Two 18-gauge copper wires are screwed to the machined pieces to allow for current to flow through the tantalum heater that is bonded to the back of the substrate holder. A thermocouple is glued to the “hot” side of the MgO substrate and connected to a wire threaded through the LN₂ reservoir sheath.

the vacancies may be filled with hydroxyl groups, which will change the nature of the MgO(100) surface and its interactions with adsorbates [4, 5]. It is important to fill the oxygen vacancies after the baking procedure has finished: CO and CO₂ that outgasses from the walls of the chamber can react with the hot tantalum wire to form tantalum carbide [6]. This can reduce the heater's lifetime and increase the amperage needed for reasonable heating rates.

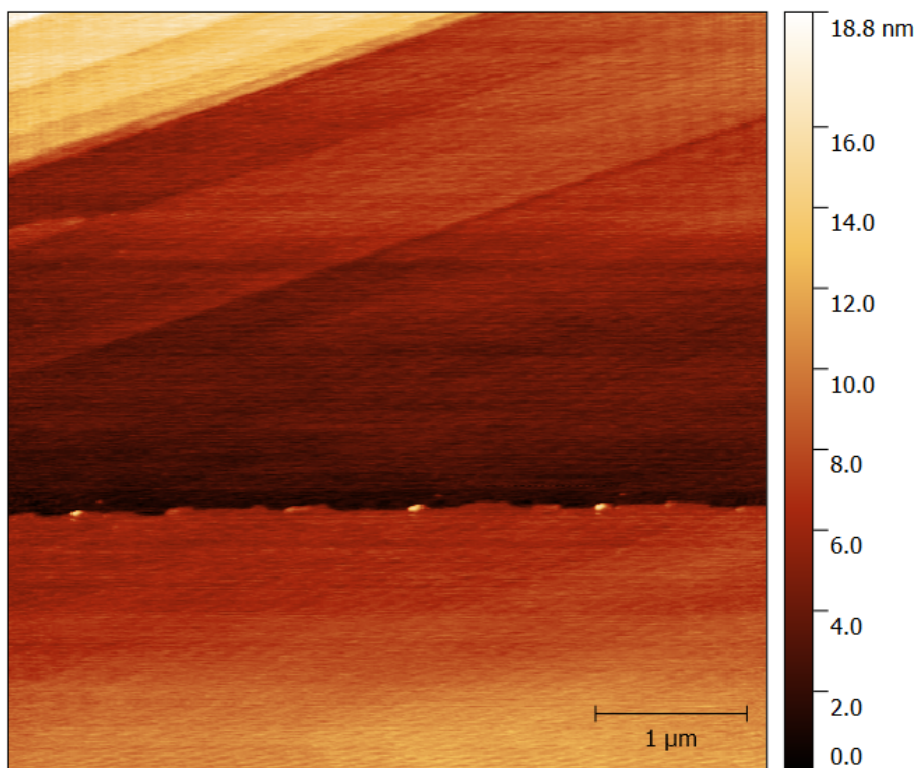


Figure 3.3: An AFM image of a cleaved MgO(100) surface. The surface is quite flat and unblemished, with terraces as the main visible feature along with a slightly larger aberration.

3.4 Sample Growth

All films were grown on a MgO substrate that was cleaned of background gases which may have condensed between experiments. This was ensured by heating the

surface to ~ 200 K to desorb water and NO_2 layers. Water samples (Macron Fine Chemicals, UHPLC-grade) were degassed with a freeze-pump-thaw cycle that was repeated until no bubbles were visible upon thawing. Nitrogen dioxide (Aldrich, $\geq 99.5\%$ purity) purity was monitored by visual inspection upon freezing of the sample. A pure white solid indicated high purity; a blue tinge was evidence of N_2O_3 contaminant. To remove N_2O_3 , O_2 was added in excess to the sample vessel and left to react with NO contaminant. The sample was then frozen with LN_2 , and the remaining O_2 was pumped off.

All materials except for NO_2 were introduced to the UHV chamber via background dosing. Three high-precision leak valves (MDC ULV-150) are affixed to the middle and bottom tiers of the chamber to allow for dosing of multiple chemicals. The leak valves were opened until the ionization gauge (Granville-Phillips 330) read a specific pressure, and then the leak valve was left open for a predetermined amount of time to grow a film of a known thickness. The pressures and times were determined previously in this lab [3] and corroborated by the calibration procedure described in the following section. Based on the calibration for ASW, at 2×10^{-7} Torr, a monolayer (ML) of material is deposited every three seconds. Because it is difficult to define what a "monolayer" is for N_2O_4 , its thickness is reported in Langmuirs. A Langmuir (L) is defined as exposure to 10^{-6} Torr for one second.

Because of the catalytic reaction of NO_2 with metal surfaces that forms NO, a different dosing method had to be designed that minimized contact with the stainless steel interior of the UHV chamber. A 1 cm diameter \times 25 cm long glass tube was cemented to a custom stainless steel piece (USC machine shop) that could be affixed to the interior face of a leak valve with stainless steel screws. By rotating the surface position, we could achieve directed dosing. Initially, this pathway had to be passivated to ensure that NO_2 , not NO, was the majority species entering the vacuum chamber. This was accomplished by opening the NO_2 line leak valve slightly (10^{-8} Torr) and monitoring the NO/ NO_2 ratio with the RGA until it had stabilized. Despite the position being

irrelevant for background dosing, the surface was rotated to face the NO_2 doser at the beginning of the growth sequence for all films that contained N_2O_4 to ensure a quick and consistent dosing process.

3.4.1 Calibration Using TPD

In order to quantitatively determine film thickness as a function of dosing time, it is necessary to conduct a TPD experiment of a monolayer of H_2O to compare to the bulk. The H_2O monolayer desorbs at a higher temperature than the bulk (240 K compared to 165 K [7]), so the spectral feature can be isolated for integration. Once the value for a monolayer is known, different dosing times can be analyzed and integrated for comparison, and thickness can be calculated. However, definitively detecting the monolayer proved to be more difficult than expected, and another calibration method using TPD had to be devised.

TPD experiments were carried out using an SRS RGA 300 with an attached nose cone (USC machine shop). A fine mesh was affixed to the ~ 8 mm opening of the nose cone with ceramic glue (Aremco 835M); this ensured that only material that entered the nose cone could be ionized and detected. Notches were added to the edge of the nose cone to aid pumping efficiency. This greatly reduced a long tail that was observed in initial spectra collected with the old nose cone design. The surface was lowered to the main chamber and H_2O films were grown at ~ 100 K. This was necessary to obtain results representative of film growth for typical experiments, as films grown when the surface was in the upper chamber desorbed approximately half as much material with the same dosing times as when grown in the main chamber, where films are grown for typical experiments. The surface was then raised to the upper tier and oriented towards the end of the nose cone, at a distance of 4 mm. A custom LabView program collected signal while the surface was heated to approximately 300 K at a rate of 1-2 K/s.

A representative set of TPD spectra are shown in Figure 3.4a. The multilayer desorption peak reproducibly desorbed around 180 K, which is consistent with TPD data

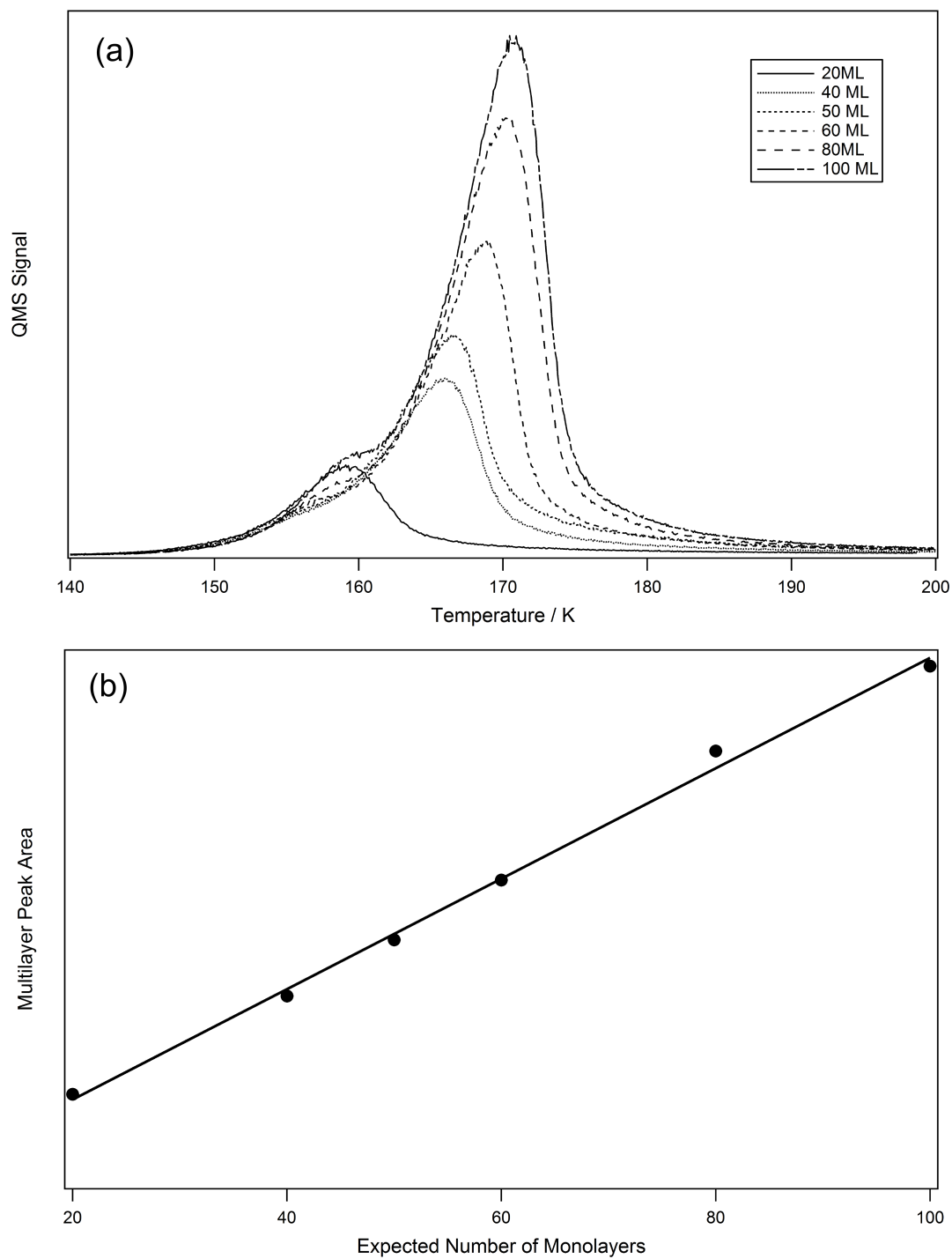


Figure 3.4: (a) TPD spectra from ASW films (20-100 ML) grown in standard dosing position (Tier 2). The bulk ASW desorption occurs at 165 K, with a crystallization peak that appears at 160 K. (b) Integrated areas from the plots in (a) compared to previously calibrated film thicknesses.

published by the groups of Kay and Goodman [7–10]. The dosing times compared to expected film thicknesses showed a linear trend (Figure 3.4b), which was consistent with previous calibrations done in the lab.

3.4.2 Directed Dosing vs. Background Dosing

The limitations of working with NO₂ due to its reactivity with stainless steel surfaces led to the inclusion of directed dosing apparatus. Water and other nonreactive species were still dosed via back-filling the chamber to avoid cross-contamination of dosing lines. As growth was measured assuming a calibration curve based on background dosing pressures, it was necessary to determine the growth difference between dosing methods. Quantitative measurements of films are possible using FTIR; however, direct measurement of NO₂ is impractical with our equipment as the only absorption peak within the detection range is a very weak combination band [11]. Water was chosen as an acceptable analogue for NO₂ as both species have unit sticking coefficients at 100 K [12, 13]. Films were grown by back-filling the chamber and via the direct pathway at 2×10^{-7} Torr for 5 minutes, which is equivalent to 60 L (100 ML based on the previously discussed calibration). The FTIR spectra of the films grown from each pathway were collected and the area of the broad OH stretch absorption peak centered at 3200 cm⁻¹ for each was calculated. The raw spectra are shown in Figure 3.5.

To account for material dosed on the back side of the MgO substrate, the area of the background spectrum was divided in half. This value was then subtracted from the direct dosing spectrum. Using the adjusted peak areas, the direct dosing peak was a factor of 1.7 larger than the background dosing peak.

3.5 Time-of-Flight Mass Spectrometer

In order to measure a mass spectrum in our UHV chamber, material must be ejected from the surface of the MgO substrate. This is accomplished by irradiating the surface

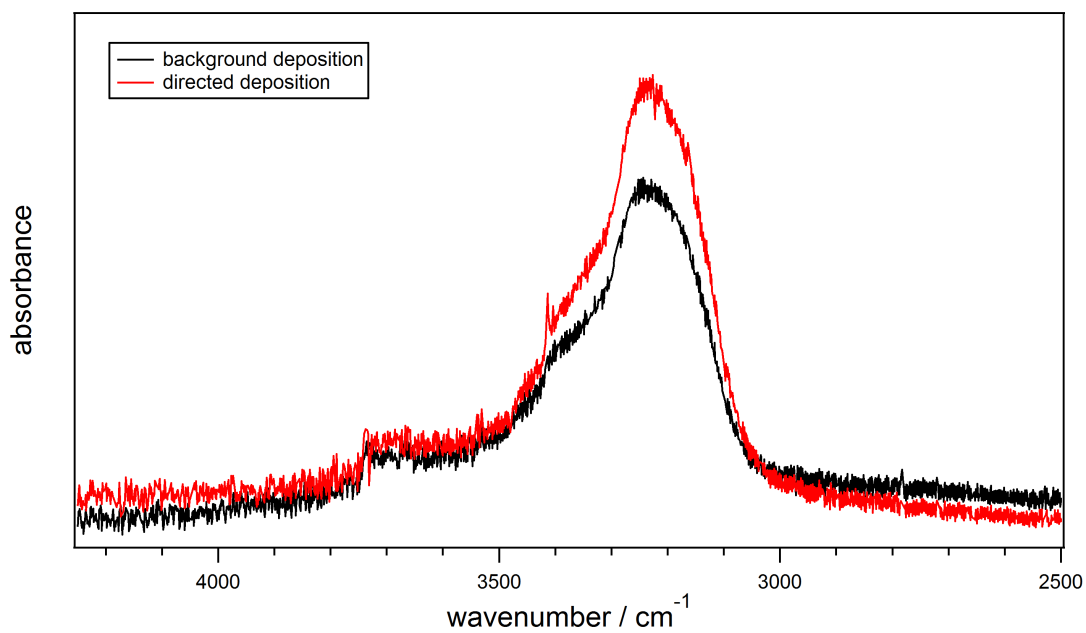


Figure 3.5: FTIR spectra of ASW grown by background and directed dosing, each at 2×10^{-7} Torr for 5 minutes (equivalent to 100 ML for background deposition). Removing the contribution of material that grows on the back side of the MgO substrate (see text for discussion of this calculation), directed dosing increases film thickness by a factor of 1.7 when compared to background dosing.

with a Nd:YAG laser (Continuum 9010, 1064 nm, 10 ns pulse) triggered at 10 Hz. The third or fourth harmonic is generated to give 355 or 266 nm radiation that is collimated to ~ 3 mm using a telescope. The radiation is used either at this diameter to irradiate the whole surface or focused with a 50 cm CaF₂ lens to a diameter of ~ 0.3 mm at the MgO surface. The frequency is also reduced from 10 Hz to 1 Hz using an optical chopper wheel (ThorLabs MC1000) to enable a higher sampling rate with the analog-to-digital converter. The radiation then enters the UHV chamber through a CaF₂ window and strikes the MgO substrate normal to the plane of the substrate and orthogonal to the flight path of ionized material (entrance port is indicated by a star in Figure 3.1). The substrate is located approximately 2.5 cm from the center of the ionizing region of the time-of-flight mass spectrometer.

Our time-of-flight mass spectrometer (TOFMS) was custom-made by Jordan TOF Products and is a two-stage linear Wiley-McLaren-style mass spectrometer [14]. Upon irradiation, ablated material enters the extraction region parallel to two plates that are held at 1800 V. A fraction of the material in this region is ionized by a continuous stream of 70 eV electrons. After 7 μ s, the voltage on the extractor plate is dropped to 1550 V, and ions are extracted for 3 μ s into the acceleration region, where a third accelerator plate is grounded. The voltage difference results in the ions being accelerated into a 48 cm-long field-free drift region. Voltages were chosen to optimize mass resolution around $m/q = 18$. Ions are detected by a multi-channel plate (MCP) and signals are amplified with a fast pre-amplifier (SRS D-300 MHz) and then converted using an analog-to-digital card (Gage CS 8500, 8 bit, 512k samples, triggered at 10 Hz).

The TOFMS can be pulsed at rates up to 200 kHz; for these experiments, it is triggered at 100 kHz, which results in a complete mass spectrum every 10 μ s. During one laser pulse, a sequence of mass spectra is collected, which is referred to herein as a "temporal profile". By adjusting the sampling rate, mass spectra can be collected over a 300, 600, or 1200 μ s window (30, 60, or 120 total mass spectra). However, increasing the length of the temporal profile window results in a slight decrease in resolution.

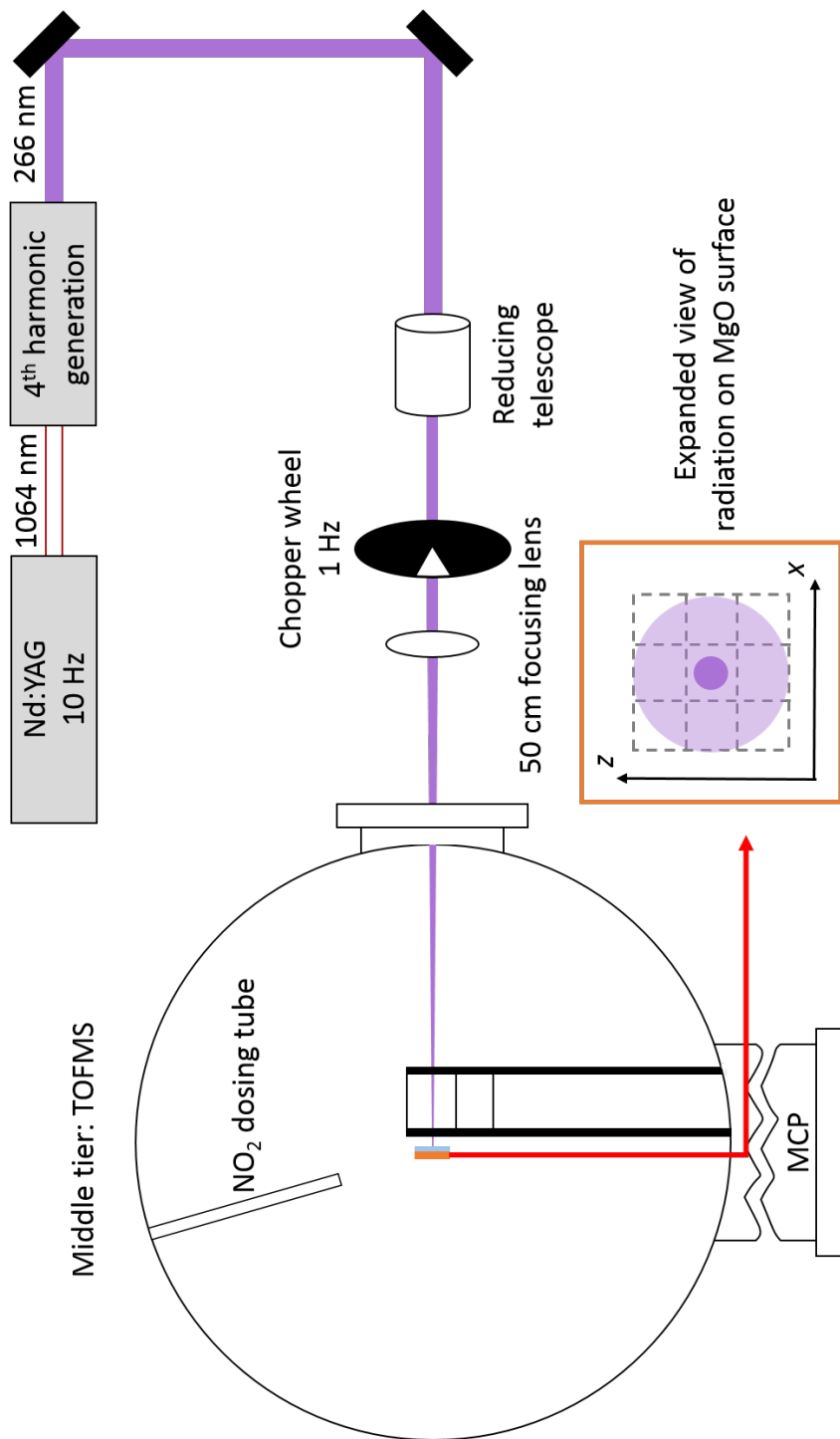


Figure 3.6: A schematic representation of the TOFMS experiment. The fourth harmonic from a Continuum Nd:YAG is used. The beam waist is reduced to 3 mm using a telescope. The radiation enters the chamber and excites the film at normal incidence. Released material is ionized, extracted, and then detected using a multi-channel plate (MCP) at a rate of 100 kHz. The set-up shown is with focused radiation, which allows for 9 individual “experiments” on one film via translation in the xz plane, as indicated by the grid. These data can be averaged to improve S/N. By removing the 50 cm lens, a larger area can be irradiated (shown in light purple) to allow FTIR experiments of the ablated film.

Spectra are collected either from nine 0.3-mm-diameter spots on the MgO(100) surface or a single ~ 3 mm-diameter spot centered on the surface (Figure 3.6). Multiple shots on the same surface are possible because of the minimal lateral transfer of energy during a laser pulse [15]. While the electronic excitation of the film via irradiation decays to heat on a picosecond time scale, the diffusion of that heat through a film is not as rapid. Thermal diffusion length in a surface is defined by

$$L_{\text{tm}} = (2\kappa\tau_L)^{1/2} \quad (3.1)$$

where κ is the thermal diffusivity of the material and τ_L is the laser pulse length [16]. Thermal diffusivity of amorphous ice can be estimated as

$$\kappa_a = \frac{v\lambda}{3} \quad (3.2)$$

with v equal to the velocity of sound and λ is the phonon mean free path [17]. Using a velocity of 3×10^5 cm s⁻¹ and a mean free path of 10 Å gives $\kappa_1 \approx 10^{-2}$ cm²/s. Using this value along with our pulse length of 10 ns results in a thermal diffusion length of 45 nm. Even assuming a κ value based on crystalline ice, whose maximum reported value is 0.4 cm²/s at 100 K and can be considered an upper limit [18], the thermal diffusion length is 0.9 μm. Thus, translating the surface 1 mm in the xy -plane allows for irradiation of essentially undisturbed material, and multiple laser passes can occur on one film. The 3×3 grid pattern shown in Figure 3.6 was the typical radiation pattern for each film to maximize data collection without getting too close to the copper holder. In contrast, irradiating the same spot multiple times results in a more complex set of data as the first laser pulse irreversibly alters the ASW film (this will be discussed further in Chapter 4). As such, subsequent shots on that spot are interacting with a film with an ill-defined morphology.

When nine spots are irradiated on a single film, it allows for the temporal profiles to be averaged together. By averaging the spectra, the signal-to-noise (S/N) can be greatly improved and film irregularities and fluctuations in laser energy have less of an impact on data collection. However, the S/N is high enough that individual temporal

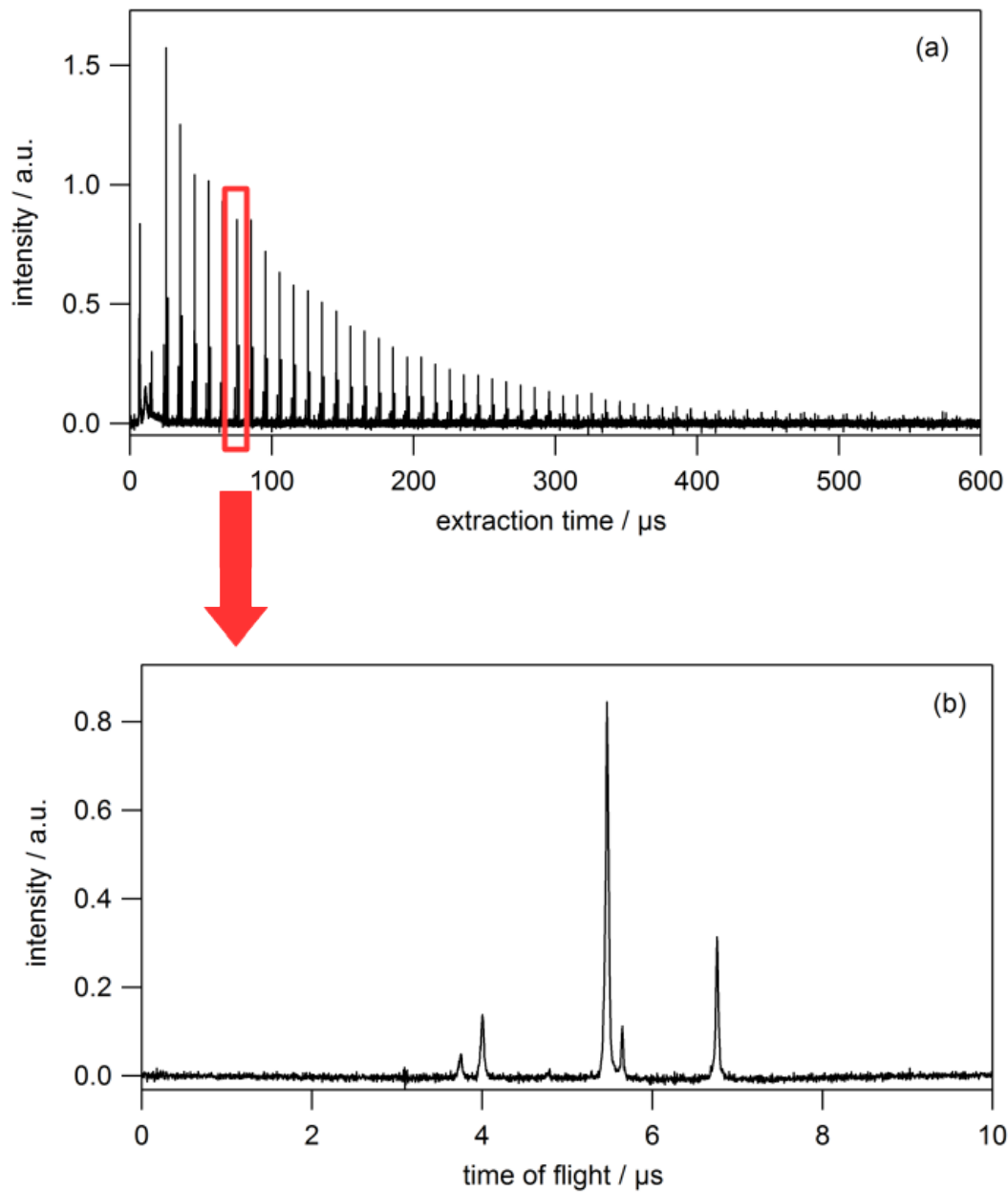


Figure 3.7: (a) An example of a full temporal profile. It is the average of data collected from eight individual spots from a film of 80 L of N_2O_4 ablated with focused 1.0 mJ radiation. Each 10 μs segment represents a full mass spectrum, shown as (b), of a segment of the plume of material that desorbs from the surface. The data can be analyzed as a full temporal profile or as individual mass spectra.

profiles can still be used for analysis. An example of a temporal profile is shown in Figure 3.7a. These profiles can be broken down into the individual mass spectra that are taken every 10 μs . Each mass spectrum can be thought of as representing the make-up of a specific section of the plume (Figure 3.7b). In this way, the shape of the temporal profile gives information about the speed and amount of material leaving the surface, and individual mass spectra give insight into the make-up of the plume at different times after the initial laser pulse.

3.6 Time Synchronization

As stated previously, we trigger the TOFMS at 100 kHz. In order to synchronize this with the firing of the Nd:YAG laser, we have a set of four low-jitter digital pulse generators (SRS DG535) daisy-chained together as shown in Figure 3.8. This is an improved set-up from a previous iteration that only used three pulse generators where the TOFMS trigger had a jitter of ± 160 ns. Because of this, the flight times would vary from experiment to experiment. By using four pulse generators, we reduced the jitter in the TOFMS with respect to the laser pulse by a factor of 10 (± 10 ns) and improved experiment-to-experiment timing stability. This also increased confidence in peak assignments due to the decreased variability in flight times for specific masses.

A brief summary of the triggering mechanism follows: the TOFMS pulse generator runs at 100 kHz, acts as the master, and sets the internal clock for the other three pulse generators. The output of the TOFMS pulse generator triggers a second pulse generator that effectively runs at 10 Hz due to the delay settings (Table 3.1) It externally triggers the flash lamps of the Nd:YAG laser. A third pulse generator is triggered off of the flash lamps pulse generator. It also effectively runs at 10 Hz, but it controls Q-switching of the laser which is triggered after a 364 μs delay to optimize the energy output. Finally, the fourth pulse generator controlling the optical chopper wheel is triggered off of the TOF pulse generator and runs at 100 Hz.

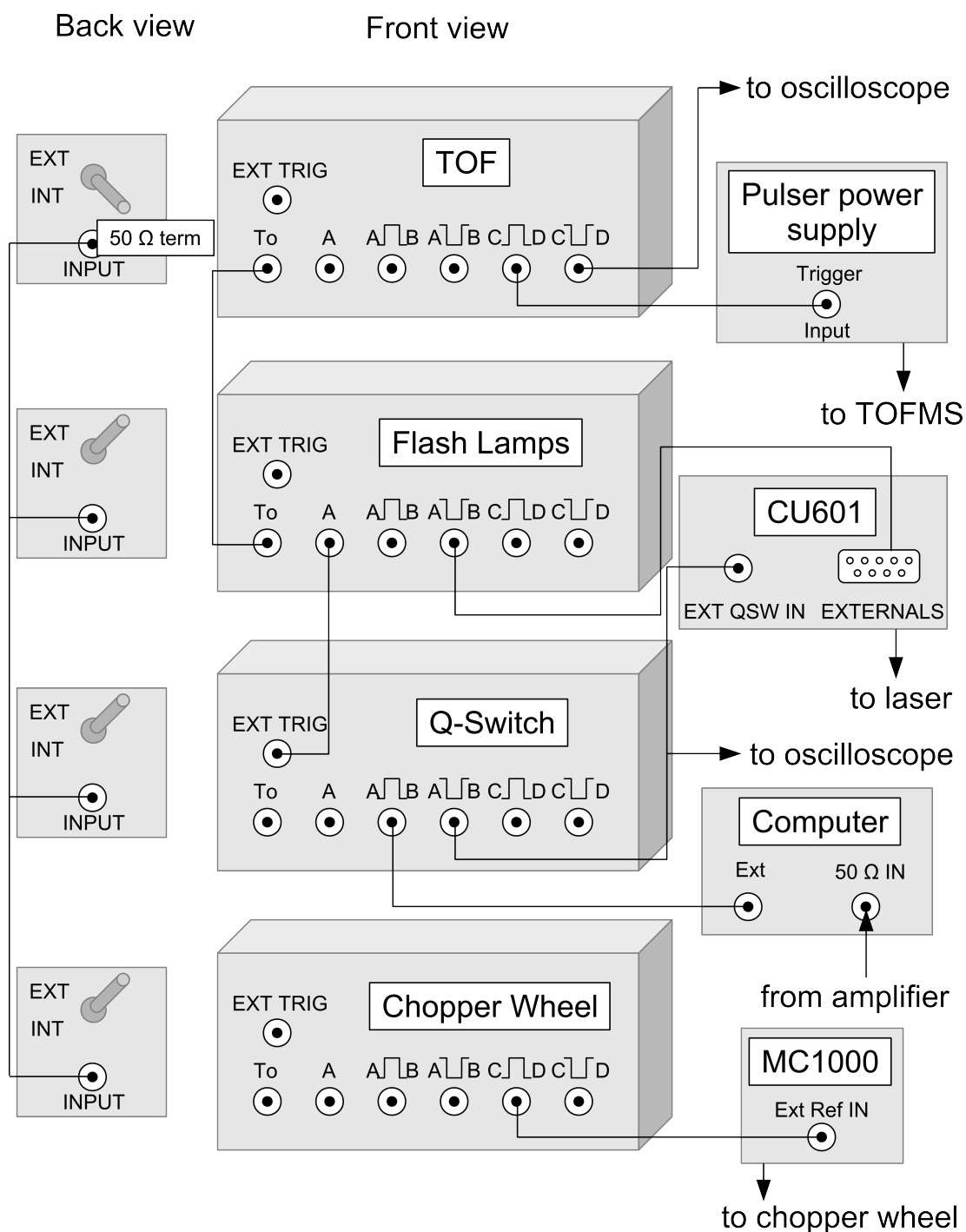


Figure 3.8: A schematic of the four SRS DG535 Digital Delay/Pulse Generators that control the triggering for the TOFMS, chopper wheel, and Nd:YAG laser flash lamps and Q-switch; only necessary connections and switches have been depicted for clarity. Refer to Table 3.1 for individual pulse generator settings.

Table 3.1: Timing settings for each pulse generator used in the timing set-up. Note: all of the pulse generators are triggered at 100 kHz except for the pulse generator triggering the optical chopper, which has a repetition rate of 100 Hz. Refer to labels from Figure 3.8.

	A=T+	B=A+	C=A+	D=T+	AB
TOFMS	0	500 ns	0	0	50 Ω , TTL
Flash lamps	62.1 μ s	10 μ s	0	99.995 ms	High Z, TTL
Q-switch	324 μ s	10 μ s	0	0	High Z, TTL
Chopper wheel	0	10 μ s	0	9.995 ms	High Z, TTL

3.7 FTIR

A Nicolet Protegé 460 spectrometer is located next to the top tier of the UHV chamber and was used in conjunction with an external InSb detector (Nicolet 860) for all experiments detailed in this dissertation. The IR beam was directed and focused through the surface (which was moved to the top tier for data collection) with a flat mirror and a parabolic mirror and then refocused on an indium antimonide (InSb) detector with a second parabolic mirror. The entrance and exit windows on the FTIR tier are CaF₂ to allow for transmission of the IR beam. A wire-grid polarizer (Moletron, 93-98% purity) was sometimes placed in the IR beam path to prevent saturation of the detector. The optics and detector are housed in opaque, lidded plexiglass boxes that are purged with dry N₂ to decrease absorption due to background gases (e.g. CO₂, water vapor). Purge gas for the external boxes and the FTIR bench was provided by a dry air gas generator (Whatman, FT-IR 75-62) that filtered H₂O and CO₂ from a house compressed air line.

Spectra were measured using OMNIC software to collect 200 scans per spectrum at a 1 cm⁻¹ resolution over the range 1850 to 7000 cm⁻¹. With these settings, the system was sensitive enough to detect <10 ML of ASW on the MgO substrate. FTIR was used for checking dosing procedures as well as film changes from heating and irradiation.

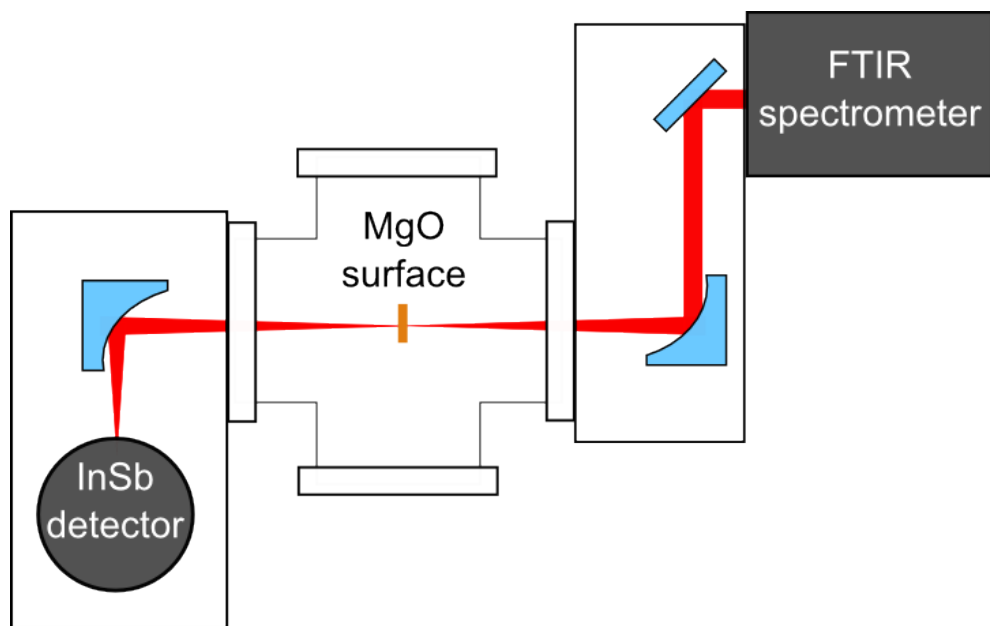


Figure 3.9: A schematic of the top chamber tier, showing the FTIR pathway. Radiation from the detector is directed and focused through the surface using flat and parabolic mirrors. It is then focused on a liquid nitrogen-cooled InSb detector with a second parabolic mirror. All external optics are encased in plexiglass boxes that are purged with dry air.

For irradiation experiments, a background spectrum was collected in Tier 1, the surface was moved to Tier 2 for dosing, it was then moved back to Tier 1 for an initial spectrum, then moved back down to Tier 2 to be irradiated, and then moved up to Tier 1 for the final spectrum.

Chapter References

- [1] Suchan, M. M. Molecule-Surface Interactions in HCl/MgO and Water/MgO Systems., Ph.D. Thesis, University of Southern California, 2001.
- [2] Slack, G. A. *Phys. Rev.* **1962**, *126*, 427–441.
- [3] Malyk, S. Transport and Guest-Host Interactions in Amorphous and Crystalline Ice., Ph.D. Thesis, University of Southern California, 2009.
- [4] Korolik, M.; Suchan, M.; Johnson, M.; Arnold, D.; Reisler, H.; Wittig, C. *Chem. Phys. Lett.* **2000**, *326*, 11–21.
- [5] Knözinger, E.; Jacob, K.; Hofmann, P. *J. Chem. Soc. Faraday Trans.* **1993**, *89*, 1101–1107.
- [6] Chrysanthou, A.; Grieveson, P. *Mat. Sci. Eng. A* **1995**, *194*, L11–L14.
- [7] Hawkins, S.; Kumi, G.; Malyk, S.; Reisler, H.; Wittig, C. *Chem. Phys. Lett.* **2005**, *404*, 19–24.
- [8] Kim, Y. D.; Stultz, J.; Goodman, D. W. *J. Phys. Chem. B* **2002**, *106*, 1515–1517.
- [9] Günster, J.; Liu, G.; Stultz, J.; Krischok, S.; Goodman, D. W. *J. Phys. Chem. B* **2000**, *104*, 5738–5743.
- [10] Stirniman, M. J.; Huang, C.; Smith, R. S.; Joyce, S. A.; Kay, B. D. *J. Chem. Phys.* **1996**, *105*, 1295–1298.
- [11] Mélen, F.; Pokorni, F.; Herman, M. *Chem. Phys. Lett.* **1992**, *194*, 181–186.
- [12] Dixon-Warren, S. J.; Jackson, R.; Polanyi, J.; Rieley, H.; Shapter, J.; Weiss, H. *J. Phys. Chem.* **1992**, *96*, 10983–10994.
- [13] Brown, D.; George, S.; Huang, C.; Wong, E.; Rider, K.; Smith, R.; Kay, B. *J. Phys. Chem.* **1996**, *100*, 4988–4995.
- [14] Wiley, W.; McLaren, I. *Rev. Sci. Instrum.* **1955**, *26*, 1150–1157.
- [15] Burgess, D.; Stair, P.; Weitz, E. *J. Vac. Sci. Technol., A* **1986**, *4*, 1362–1366.
- [16] Matthias, E.; Reichling, M.; Siegel, J.; Käding, O.; Petzoldt, S.; Skurk, H.; Bizenberger, P.; Neske, E. *Appl. Phys. A* **1994**, *58*, 129–136.
- [17] Smoluchowski, R. *Astrophys. J.* **1981**, *244*, L31–L34.
- [18] Hobbs, P. V., *Ice physics*; Oxford: Clarendon Press: 1974.

Effects of Buried Heat in Amorphous Solid Water

Films

Previous experiments done in this lab had been carried out using IR radiation to excite amorphous solid water; as such, there was an element of the unknown to how NO_2 would interact with radiation with our experimental approach. As we would be exploring a new system and method of energy transfer to ASW films, extensive testing and characterization of the system was carried out. Important data trends with various combinations of N_2O_4 and ASW are summarized in this chapter, and a model for morphological change and transport in ASW is presented. The process of fine-tuning signal collection is also documented herein.

4.1 Introduction

Amorphous solid water (ASW) has been the subject of intense study since its original discovery in 1935 [1]. It remains fascinating to the scientific community due to its unusual structure and characteristics, such as its heat capacity behavior and high viscosity at low temperatures, that continue to elude understanding [2]. ASW has come under further scrutiny as it became apparent that H_2O is an abundant molecule in the interstellar medium (ISM), and the corresponding cold temperatures necessitated that it would commonly exist in the solid phase [3]. ASW is present in diverse astronomical

environments, from the surface of Enceladus to dust grain mantles, the latter of which it is believed to be the main component. In the ISM, ASW is subject to a variety of energy sources that can trigger morphological changes: chemical and thermal processing, gas phase bombardment, and UV radiation [4]. As such, an understanding of fundamental properties of this substance is important for basic scientific inquiry as well as for gaining insight into chemical processes in the universe.

Many studies have addressed the unique changes that occur in ASW when it undergoes morphological changes from thermal heating [5–7]. Previous work done in our lab has investigated ASW changes using infrared radiation as an energy source. We found that IR absorption in an ASW film initiated efficient ejection of water monomer and small clusters, as well as the preferential release of guest species [8]. In the experiments documented in this chapter, we wanted to elucidate morphological changes and molecular transport when stress was exerted by a guest molecule. Specifically, the electronic excitation of N_2O_4 was exploited to introduce a very hot layer of material within an ASW film, which could then disrupt the surrounding matrix. A broad absorption band due to an electronic transition centered around 250 nm allows for easy excitation with the fourth harmonic of a Nd:YAG laser (10 ns duration, 266 nm, 10 Hz) that can then degrade to heat on a ps time scale [9, 10]. This combination gives a facile way to investigate the effect of heat in a buried stratum, though interpretation proved to not be trivial.

While these experiments were conducted with microscale films (~ 100 -1000 nm), they may provide some qualitative insight into macroscale events. A specific example is Enceladus, a moon of Saturn that is believed to have a liquid water ocean located underneath a thick solid water crust. This theory is based on detection of “plumes” of molecules (H_2O is the dominant molecule, along with CO_2 , NH_3 , HCN , CH_2O , CO , H_2 , and CH_4) that erupt from the surface along the “tiger stripes” located on the south polar terrain [11, 12]. It is believed that tidal stresses provide enough thermal energy to maintain a liquid ocean. When extreme pressure and heat is generated during the

cyclic ebb and flow of this system, the liquid water forces its way through fissures in the upper ASW layer and escapes.

The material presented in this chapter covers a thorough review of experiments conducted with this system. Films were grown via vapor deposition between 95 and 110 K, which resulted in a low-density ASW film. Subsequent UV photolysis of a N_2O_4 layer creates a hot fluid that then contributes to a temperature and pressure gradient within the film. If covered by a layer of ASW, N_2O_4 forces its way through fissures to escape to vacuum, scraping water monomer from the wall during transport.

4.2 Experimental

A schematic of the experimental apparatus used for irradiation of all ASW/ N_2O_4 films discussed in this chapter is shown in Figure 3.6 in the previous chapter. Experiments were conducted in an ultra-high vacuum (UHV) chamber (3×10^{-10} Torr) using pulsed 266-nm radiation (10 Hz, 10 ns) in conjunction with a high-repetition time-of-flight mass spectrometer (TOFMS) from Jordan TOF Products. The UHV chamber has multiple tiers capable of different types of experiments; these specifications have been documented thoroughly elsewhere [8, 13]. Briefly, the top tier allows for temperature-programmed desorption (TPD) and Fourier transform infrared (FTIR) spectroscopy, and the middle tier houses the equipment for TOF mass spectrometry. The latter two methods are those used to obtain the data in this chapter.

A MgO(100) substrate was used for all experiments. The MgO surface was obtained by cleaving a crystal on both sides in dry N_2 . The $0.8 \times 10 \times 10$ mm substrate was then transferred to the UHV chamber. Once vacuum was achieved, oxygen vacancies in the MgO substrate were filled by backfilling the chamber with O_2 (10^{-8} Torr) and annealing the surface to 600 K for an hour. This procedure has been shown to produce a high quality MgO(100) surface [14].

The substrate was clamped in copper foil (0.012 in. thick) with a 6×6 mm square cut-out for radiation to pass through. It was then attached to the arm of one of two

electrically-isolated copper blocks that were mounted onto a copper-capped stainless steel cold finger on a LN₂ reservoir (Kurt Lesker, altered by McAllister Technical Services). With this configuration, the surface could be cooled to <100 K with LN₂ or 90 K by bubbling He through the LN₂. The temperature was monitored using a K-type thermocouple glued (Ceramabond 835-M, Aremco Products) to one side of the MgO surface. A tantalum wire cemented to the back of the copper housing of the surface was used for resistive heating. The cryostat was fitted with bellows and was capable of *xyz* translation and 360° rotation.

Liquid samples were kept in glass containers with Teflon stopcocks connected to a glass and Swagelok gas-handling manifold with an attached vacuum line. H₂O samples (Macron Fine Chemicals, UHPLC-grade) were degassed with a freeze-pump-thaw process. NO₂ (Sigma-Aldrich, ≥99.5% purity) purity was checked by freezing the sample and noting the presence of a pure white solid. The most common contaminant was N₂O₃ due to excess NO, which would give a blue cast to the solid [15]. This was addressed by adding O₂ to the sample to react with NO contaminant. After 4-12 hours, the sample was frozen (NO₂ freezing point = -11°C) and the remaining O₂ was pumped off to leave pure NO₂, evidenced by the observation of a pure white solid when frozen.

All H₂O/N₂O₄ films were grown at 100 K. All species were introduced to the surface using background dosing except for NO₂. Because of its catalytic reaction with metal surfaces, a 1 cm ID × 23 cm long glass tube was affixed to a precision leak valve for directed dosing. The surface was rotated from the TOFMS position such that the end of the tube was approximately 4 cm away and normal to the surface. After heating the surface to ~200 K to remove impurities and recooling to 100 K, each layer was dosed sequentially to avoid mixing of the species within layers. Upon completion of dosing, the surface was rotated back to TOFMS position as shown in Figure 3.6. Directed dosing grew films at a faster rate than background dosing; however, background pressure was used as an indication of dosing rate. A conversion factor of 1.7 to account for this difference was calculated from TPD experiments used to adjust all N₂O₄ thicknesses

reported herein (refer to Section 3.4.2 in Chapter 3 for a detailed description of this calculation).

Ultra-violet radiation (266 nm) was generated by pumping second- and fourth-harmonic crystals with 1064 nm radiation from a Q-switched Nd:YAG laser (Continuum PL9010, ~500 mJ, 1 ns) with a 10 Hz repetition rate. The beam was reduced from 8 mm to 3 mm in diameter using a telescope and reduced to 1 Hz with an optical chopper wheel (ThorLabs MC1000). It was then focused to ~0.3 mm beam diameter at the substrate using a 50 cm CaF₂ lens.

The TOFMS, externally triggered at 100 kHz to produce a mass spectrum every 10 μs, consisted of a linear two-stage Wiley-McLaren type extraction with three electrode plates and an electron impact ionizer. Once the film was irradiated, the plume of material leaving the substrate entered the ionizing region parallel to the repeller and extraction plates. The plates were initially held at 1800 V while the molecular plume was bombarded with 70 eV electrons from an electron beam positioned ~25 mm from the surface. The positive ions formed in this region were extracted every 10 μs by dropping the potential on the extractor plate to 1550 V for 3 μs. Ions were then accelerated by a grounded third plate into the 48 cm-long field-free drift tube. Ions were detected at the end of the drift tube by a multi-channel plate (MCP, 3100-3200 V) connected to a fast pre-amplifier (SRS D-300 MHz). The amplified current from the MCP was recorded on a computer with an analog-to-digital converter (Gage CS 8500, 8 bit, 512k samples). Spectra were collected using a custom LabView program (National Instruments) and further processed using IGOR Pro (WaveMetrics). The set of 30-120 individual mass spectra collected during a single laser pulse is referred to in this chapter as a “temporal profile”.

Nine spots in a three by three grid were irradiated per surface to give nine individual temporal profiles. This gave the option of an averaged spectrum to improve signal-to-noise and to reduce the effect of laser energy fluctuations and film irregularities. Because of the limited diffusion of energy in the surface perpendicular to the laser

beam, moving the laser position by 1 mm irradiated an “undisturbed” section of the film [16].

All FTIR spectra were collected using a Nicolet Protegé 460 spectrometer and a LN₂-cooled InSb detector. Spectra were measured using OMNIC software over the span of 1850-7000 cm⁻¹ with a 1 cm⁻¹ resolution and averaged over 200 scans. The IR beam was collimated using an iris to a 2 mm beam diameter to ensure that it only sampled the part of the surface that was irradiated. To collect an FTIR spectrum, the surface was raised to the top tier to collect a background. The surface was then lowered to the middle tier for the dosing procedure and then raised again to collect a baseline FTIR spectrum. After the surface was lowered again, the 50 cm CaF₂ focusing lens was removed to give a 3 mm-diameter beam centered on the surface. The surface was irradiated and raised to take a final spectrum.

4.2.1 Changing to UV: Using NOCl as a Test Species

Initially, the laser was reconfigured to generate 532 nm radiation via a second harmonic generation (SHG) crystal, as this wavelength is within the wide absorption band of NO₂ and was assumed to be capable of initiating desorption [17]. However, no signal was seen, and review of the literature revealed that it was very unlikely that any NO₂ would be present on the MgO surface; instead, it would all condense as the dimer, N₂O₄ [18]. To address this, a third harmonic generation (THG) crystal was installed to produce 355 nm radiation, which is absorbed by N₂O₄ [17]. After thorough testing, we were once again unable to get signal with this wavelength. This was not due to not enough N₂O₄ condensing on the MgO substrate; desorption was proven to be facile when hitting the copper holder and FTIR spectra of the surface showed the characteristic combination peak at 2960 cm⁻¹ (Figure 4.1a). The ease of signal achieved from the copper holder is likely the result of substrate-mediated processes that have been observed by other groups using metal substrates [19]: UV electrons excite valence

electrons in the substrate, which can cause a temperature spike and induce thermal desorption, among other processes.

Since we were only able to detect the presence of N_2O_4 and not the amount due to the range of our InSB detector (all N_2O_4 fundamental peaks fall below 1700 cm^{-1} [20]), a switch was made in the absorbing species. NOCl was chosen as an ideal candidate due to its similar absorption spectrum in the UV [22] and familiarity with its characteristics due to past use in this lab [23–25].

NOCl was synthesized by condensing NO and Cl_2 in a 2:1 ratio under cryogenic conditions, with NO in slight excess, in a glass vessel using a vacuum line. The mixture was left to sit for 24 hours at room temperature to ensure complete reaction. A freeze-pump-thaw purification procedure was carried out using a pentane slush ($-131\text{ }^\circ\text{C}$) to remove any excess NO. Finally, the dosing line was passivated using the same method as described previously for NO_2 , except mass 65 was monitored for saturation.

Signal was initially detected after dosing 24 L, but it was very small. Once again, coverage was confirmed using FTIR spectroscopy (Figure 4.1b), so dosing problems were not the culprit. Despite trying different combinations of coverage, laser energy, and radiation spot size, the signal size did not increase. Because of this, we switched to 266 nm radiation by installing a fourth harmonic generation (FHG) crystal in an attempt to increase the absorption, and thus, signal. This did result in increased signal, and so after some fine-tuning, NO_2 was reintroduced.

N_2O_4 signal remained small, and so various dosing combinations were tried: N_2O_4 on MgO, N_2O_4 on ASW, N_2O_4 codeposited with ASW, and ASW- N_2O_4 “sandwich.” None of these experiments had a significant improvement in signal, so a sequential measurement of laser energy was carried out after each optic. We found that laser energy was being decreased 10-fold due to a mislabeled mirror and a damaged CaF_2 lens that was absorbing most of the radiation. After replacing the lens, mirror, and optimizing the alignment, we were able to get significant signal. Subsequent experiments

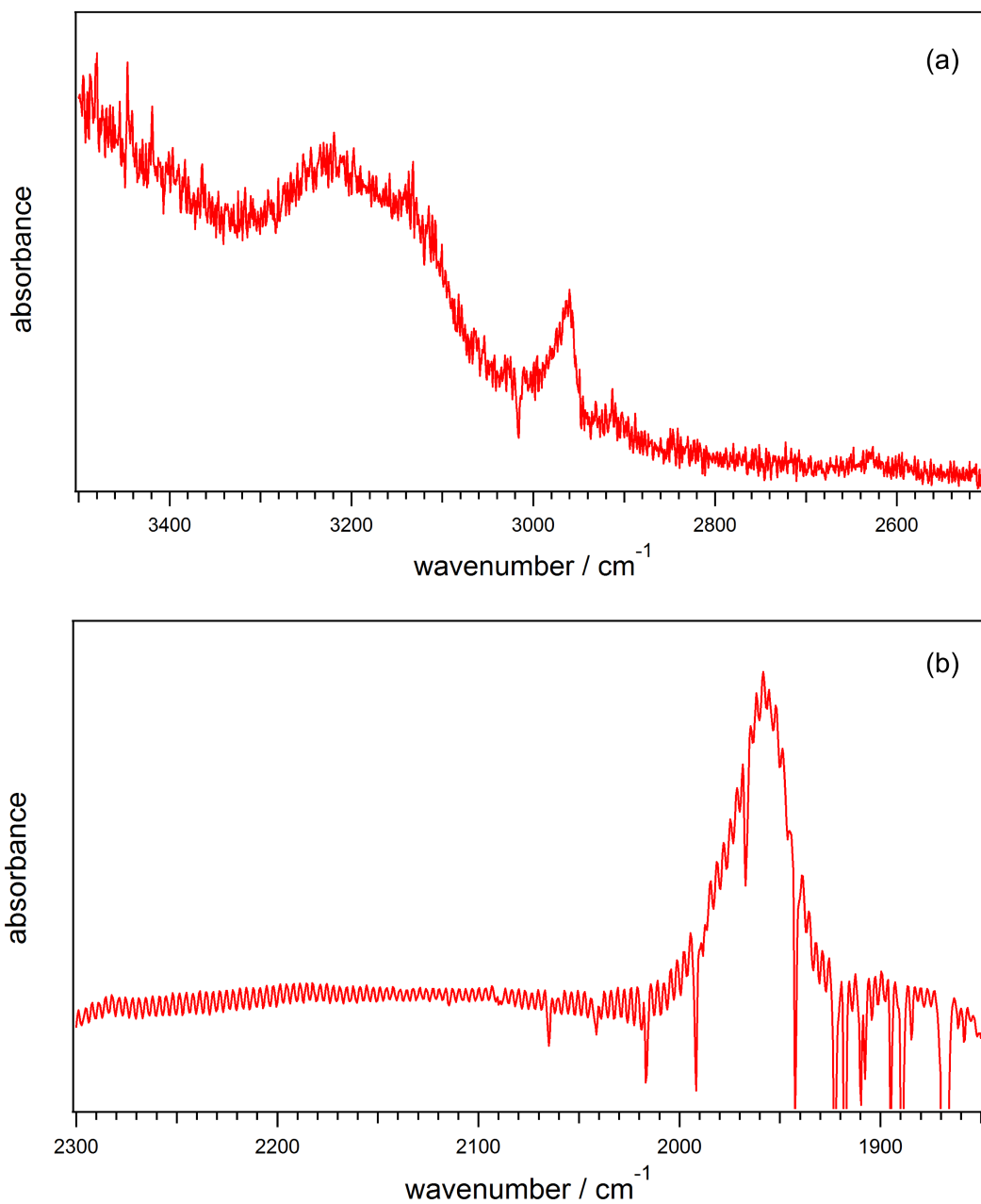


Figure 4.1: (a) FTIR spectrum of 100 L of N₂O₄. The sharp peak at 2960 cm⁻¹ is a weak combination band [20]. All fundamental bands for N₂O₄ are below the detection range of the InSb detector used in these experiments (cutoff at 1850 cm⁻¹), so this small peak was the only indication of the presence of N₂O₄ on the surface. However, it was distinct and reproducible. (b) FTIR spectrum of 110 L of NOCl (negative peaks are due to decrease in water vapor signal on the experimental time scale). The peak centered at 1955 cm⁻¹ is the N–O bond stretching mode [21]. We did not detect any other peaks associated with NOCl. While this particular peak is also representative of NO only, our surface was not cold enough to condense NO [18]. Furthermore, we were able to desorb fragments of NOCl successfully with UV radiation.

were carried out with N_2O_4 and the experimental set-up described in the the previous section.

4.3 Results

266-nm radiation was used to irradiate N_2O_4 /ASW films of various compositions and thicknesses, and single-shot and multi-shot experiments were carried out. Time-of-flight mass spectra were collected during irradiation, and FTIR spectroscopy was used to monitor the films before and after irradiation. Interpretation of this data required the collection of individual spectra for all molecules involved: N_2O_4 , NO_2 , NO , and H_2O . These spectra, along with their implications, are presented in Section 4.3.1. Following a definition of terms, the subsequent sections each present a set of data with a specific variable analyzed to characterize this system. The individual trends contributed to development of a model for fissure formation presented in Section 4.4. All TOF mass spectra and temporal profiles are the result of one pulse on a film; averaging was carried out for spot-to-spot data, not shot-to-shot (e.g., the first and second pulse data are not averaged together).

4.3.1 Standard Spectra and Data Analysis

Analysis of TOF spectra involves comparisons between individual spectra as well as accounting for individual species' contributions. In order to make such comparisons with confidence, it was necessary to collect the mass spectra with our apparatus for all experimentally-introduced molecules instead of relying on spectra published in the literature. By collecting spectra with our equipment, we avoid errors due to a difference in experimental method. The spectra obtained are shown in Figure 4.2. It was trivial to record spectra for H_2O , NO_2 , and NO by leaking vapor/gas into the UHV chamber while triggering the TOFMS. In contrast, the mass spectrum of N_2O_4 was not found in the literature, despite references to its existence [26]. This is due to the gas phase

equilibrium of $2\text{NO}_2 \rightleftharpoons \text{N}_2\text{O}_4$ where NO_2 is heavily favored at room temperature, as well as the weak N–N, which makes a gas phase spectrum of pure N_2O_4 essentially impossible to achieve through standard means. Therefore, it was necessary to devise a different method for collecting the mass spectrum of N_2O_4 .

The method chosen to obtain a “pure” spectrum of N_2O_4 was to do a thermal desorption of a condensed film. As the energy needed for desorption is 0.47 eV [27] and the bond strength of the N–N bond is 0.55 eV [28], it is safe to assume that the material that desorbs at 155 K has N_2O_4 as the majority species. This is because in order for NO_2 to enter the gas phase during sublimation, it would need enough energy to break the N–N bond and then desorb as NO_2 . Such a scenario is energetically unfavorable at 155 K, the desorption temperature of N_2O_4 . The mass spectrum for N_2O_4 is also presented in Figure 4.2; a thorough search of the literature indicates that this is the first direct measurement of the cracking pattern of this molecule.

It is apparent in Figure 4.2b that 70 eV electron impact ionization of N_2O_4 results in a maximum mass at 46 amu (NO_2^+). N_2O_4^+ isn't expected to be a stable parent ion, since ionization of an electron from the HOMO results in loss from the N–N bonding orbital. However, N_2O_3^+ was reported to be a stable parent ion [26, 29], but was notably absent in all spectra collected. Because the only species present in the N_2O_4 spectrum are identical to those produced by NO_2 (NO_2^+ , NO^+ , O_2^+ , O^+ , and N^+), determining parentage of molecules in TOF mass spectra presented a challenge. What *does* differentiate between these two species is the signal ratio between molecules from the cracking pattern. Therefore, an important number to define is the ratio between the areas of the NO^+ and NO_2^+ peaks, which we have termed R_N . NO_2^+ can only be a product from cracking of NO_2 or N_2O_4 , whereas NO^+ can result from NO , NO_2 , and N_2O_4 . As NO is most likely due to NO_2 photolysis, its contribution to R_N can be considered negligible and parentage from NO_2 and N_2O_4 can be assumed. Furthermore, this ratio is unique for NO_2 and N_2O_4 , as shown in Figure 4.2a and b, and thus can give insight into the nature of the material that is desorbing. Two very different ratios are obtained for NO_2

and N_2O_4 , which are 3.1 and 0.9, respectively. This large difference allows for some statements to be made about the parent ions.

Table 4.1: 70 eV ionization cross sections for detected molecules. All values obtained from the NIST database [30], except for N_2O_4 , which was computed from the equation given in [31].

Molecule	ionization cross section (10^{-16} cm^2)
N_2O_4	7.34
NO_2	3.53
NO	2.81
N_2	2.51
O_2	2.41
O	1.36
H_2O	2.28

There were concerns about molecular collisions with the electrodes in the ionization region due to the wide angle of desorption. Such collisions could result in dissociation of the dimer to form NO_2 and skew the results. To address this, an alternative repelling electrode was designed with a narrow slit parallel to the substrate to allow through only molecules that were desorbing close to a normal trajectory from the surface. The first design was made symmetrical to avoid a large distortion of the electrical field during extraction (Figure 4.3a). However, this had the unintended consequence of *increasing* the number of molecular collisions (observed as an increase in NO^+ signal), as material would hit the flap on the opposite side of the ionization region from the surface and subsequently be extracted. This was made apparent by an increase in R_N from 0.9 to 1.0 in all experiments involving the first electrode design. The electrode was modified such that material could more easily escape the ionization region, shown in

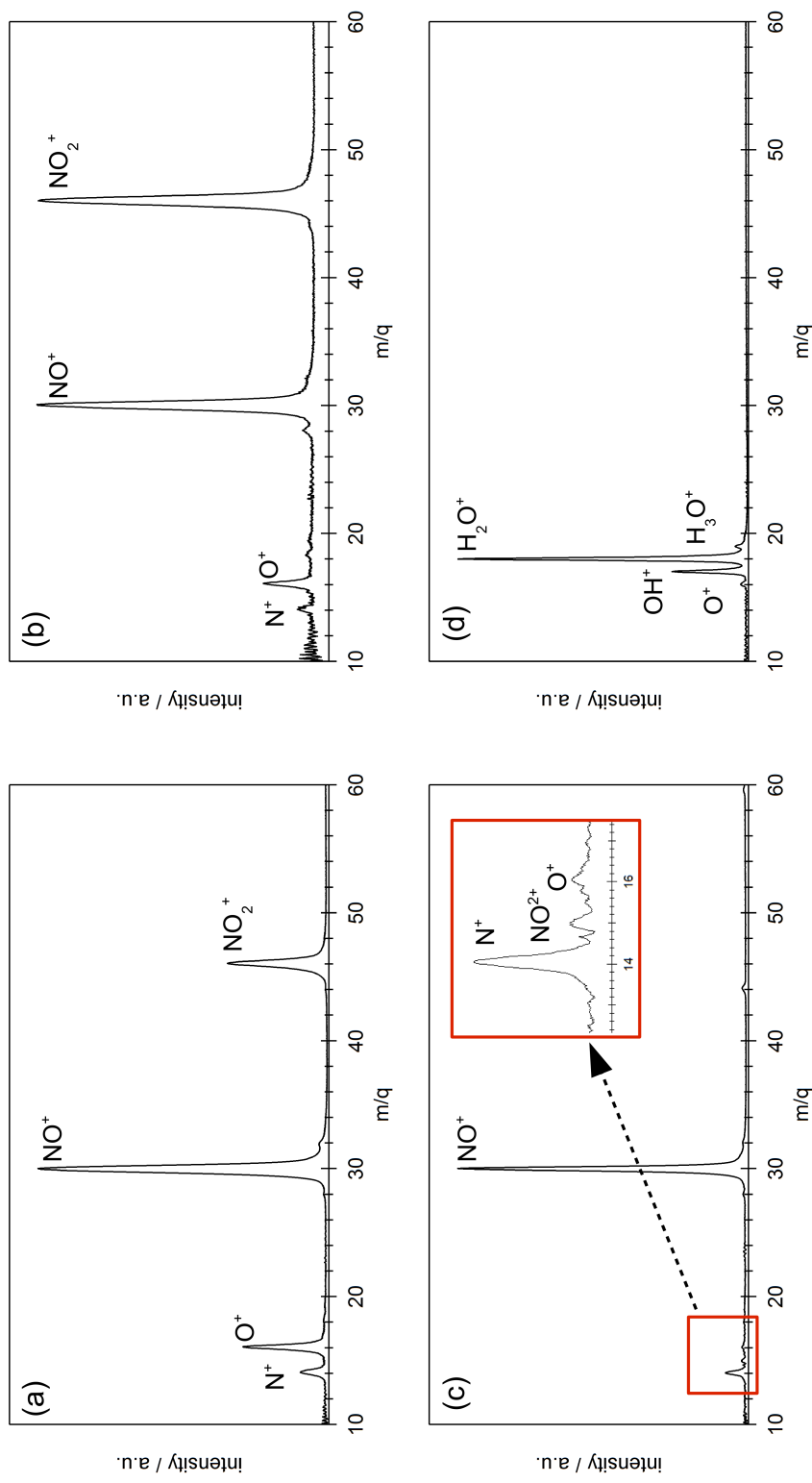


Figure 4.2: Mass spectrum of NO_2 , N_2O_4 , NO , and H_2O obtained from our experimental apparatus. All ratios given are based on peak areas. (a) 300 K NO_2 leaked into the UHV chamber gives $\text{NO}^+/\text{NO}_2^+ = 3.18$, $\text{O}^+/\text{NO}_2^+ = 0.58$, and $\text{N}^+/\text{NO}_2^+ = 0.19$. (b) 300 K NO leaked into the chamber gives $\text{O}^+/\text{NO}^+ = 0.01$ and $\text{N}^+/\text{NO}^+ = 15$ is a distinctive feature of NO electron impact ionization. (c) 300 K H_2O leaked into the chamber gives $\text{OH}^+/\text{H}_2\text{O}^+ = 0.27$, $\text{O}^+/\text{H}_2\text{O}^+ = 0.02$, and $\text{H}^+/\text{H}_2\text{O}^+$ (not shown) = 0.07. (d) The spectrum obtained via N_2O_4 sublimation at ~ 155 K gives $\text{NO}^+/\text{NO}_2^+ = 0.9$, $\text{O}^+/\text{NO}_2^+ = 0.1$, and $\text{N}^+/\text{NO}_2^+ = 0.02$. Neither N_2O_3^+ or N_2O_4^+ ($76 m/q$ and $92 m/q$, respectively) was detected (not shown).

Figure 4.3b. The resulting spectrum resembled those that had been taken with the standard electrode, indicating that spectra collected under typical conditions were reliable. Therefore, the original electrode from Jordan TOF Products was reinstalled and used for all data presented in this dissertation.

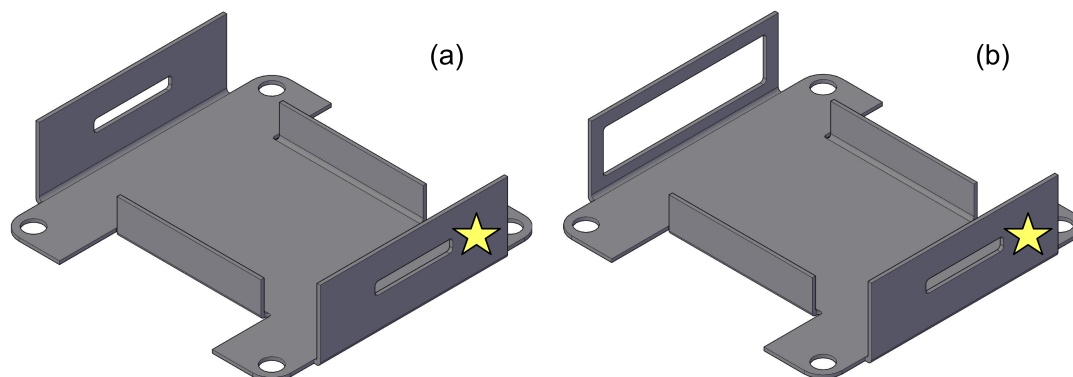


Figure 4.3: (a) The initial design for a TOFMS electrode to minimize the effect of molecular collisions with the plates. (b) Improved design for a TOFMS electrode to allow material to pass out of the ionization region. The stars designate the openings parallel to the substrate through which desorbing material would enter the ionizing region.

To better understand the interactions between N_2O_4 and ASW, sets of experiments were designed and carried out to see how different variables affected the TOFMS signal. These sets of data will be discussed individually in the following sections and will contribute to a cohesive model described in Section 4.4.

4.3.2 ASW Spacer

The starting point for irradiation experiments after getting sufficient signal was dosing a thin film of N_2O_4 on a bare MgO surface and then introducing an ASW "spacer" underneath. Representative data are shown in Figure 4.4.

There was an overall increase in NO_x^+ species signal due to the addition of an ASW film underneath the N_2O_4 layer. Integrating the peak areas of all NO^+ and NO_2^+ peaks in the temporal profiles gives a 75% increase in detected material with an ASW spacer compared to without. Such an increase in signal of the absorbing species points to

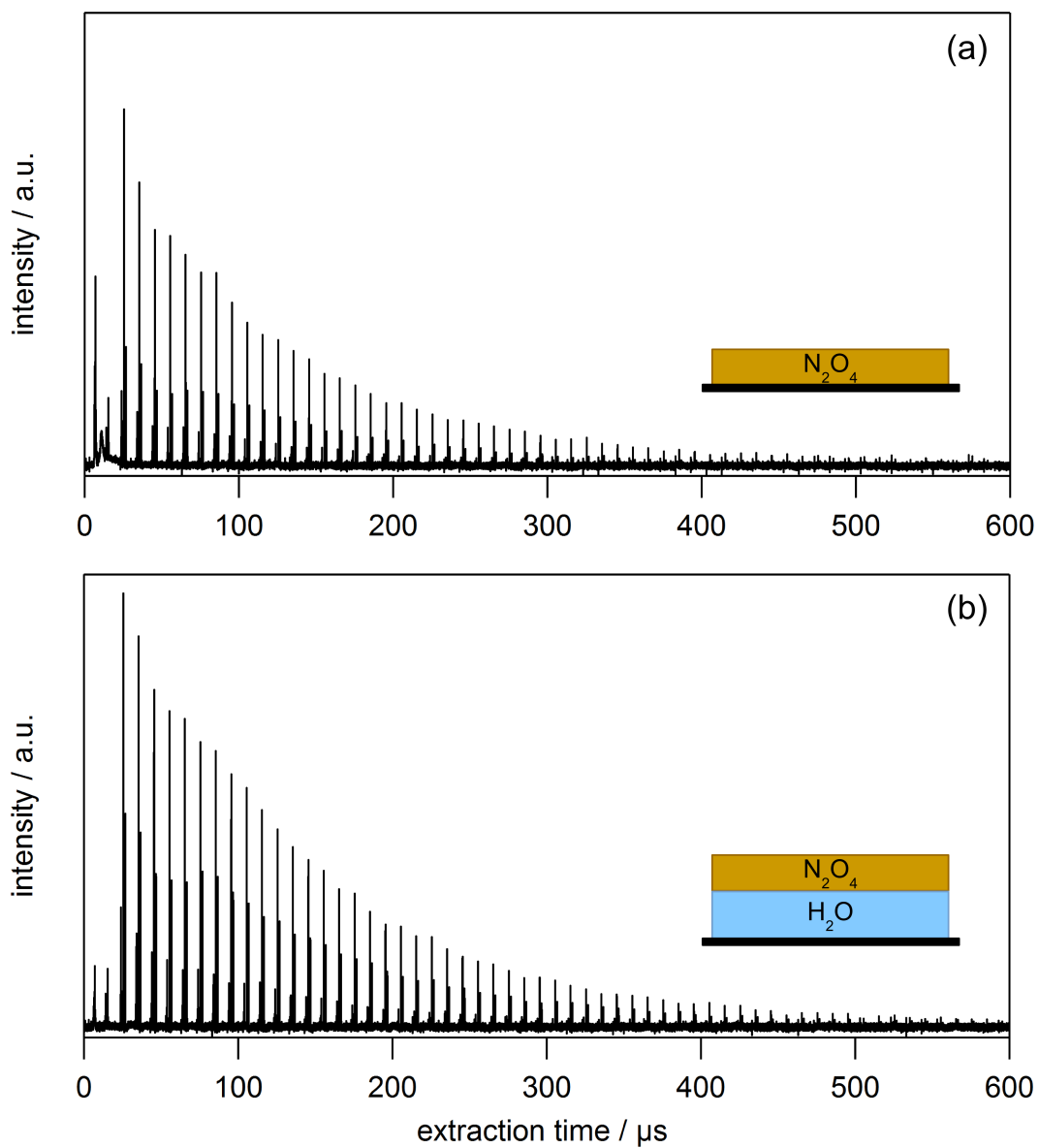


Figure 4.4: Temporal profiles of NO_x^+ signal with and without an ASW spacer, with cartoon depictions of deposition films. Both films were irradiated with a focused 266 nm, 1.0 mJ beam. (a) 80 L N_2O_4 deposited on a bare MgO substrate. (b) 80 L N_2O_4 deposited on 300 ML ASW.

an improvement in energy transfer efficiency. To explain this phenomenon, a brief discussion of thermal properties of the experimental materials is needed.

Magnesium oxide acts as an excellent thermal conductor in our experimental apparatus. At 100 K, MgO has a thermal conductivity of ~ 250 W/mK [32]. When energy is introduced to the N_2O_4 film via laser radiation, it is quickly “drained away” due to the MgO substrate being an efficient thermal conductor. In contrast, ASW is a very poor thermal conductor, whose thermal conductivity is ~ 1 W/mK [33–35]. When ASW is between the N_2O_4 film and the MgO substrate, it acts as a thermal barrier and a slower decay of heat in the absorbing layer results. Because of this, more N_xO_y species can successfully leave the substrate.

Investigation of the individual mass spectra reveals that only derivatives of N_2O_4 are present in significant quantities, as shown in Figure 4.5; almost no mass 18 (indicative of H_2O^+) is detected for films dosed with an ASW spacer unless very high fluences are used (>1.0 J/cm²).

This contrasts with results from Yang and Gudipati[36], who developed a method for removing species underneath an absorbing film. In their experiments, they started with a film of D_2O mixed with polyaromatic hydrocarbons (PAHs) and then a layer of H_2O on top. Using IR radiation to excite the O–H stretch of the top layer of water, they were able to remove the underlayer of D_2O and PAHs. In our case, little to no material is being removed from the ASW layer. Thermally, we are unlikely to remove material because any heat entering the ASW layer is dissipated too quickly for any water molecules to desorb. The other possible mechanism would be a “shockwave”, as described by Yang and Gudipati. As we are dosing very thin layers of the absorbing species (<200 nm) compared to Yang et al (~ 3 μ m), this mechanism may be too small to contribute detectable signal with our current experimental method.

Another feature of these data is the overall shape of the temporal profile. The shape of the NO_x^+ temporal profiles in Figure 4.4 is characteristic of an unobstructed pathway to vacuum. While the modulation of the NO^+/NO_2^+ ratio across a temporal profile

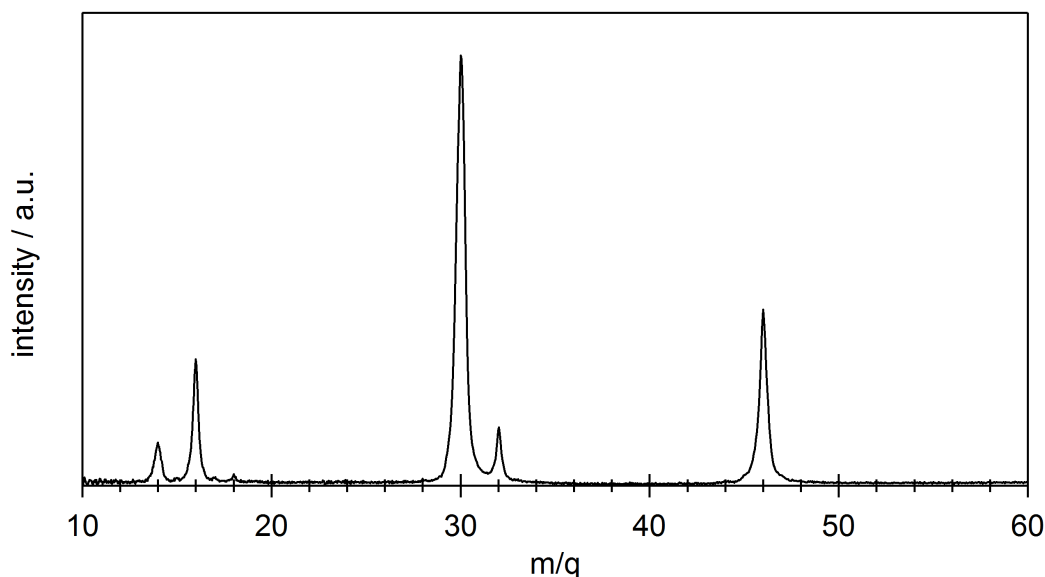


Figure 4.5: Averaged mass spectrum from extractions 2-11 (20-110 μs) of data from Figure 4.4b. All species detected can be attributed to N_2O_4 irradiation and cracking. There is a slight bump at mass 18, but it is insignificant in comparison to the other peaks and compared to previous experiments conducted by this lab.

differs for various N_2O_4 and ASW spacer thicknesses, the qualitative shape remains the same. This will become significant when discussing trends with obstructed pathways, *i.e.* a layer of material over a N_2O_4 layer.

The first extraction of the temporal profile shown in Figure 4.4 that yields a resolved mass spectrum is the 20 μs extraction. Assuming a molecule leaves at the surface at $t = 0$ and using 20 μs as an approximation of travel time to the ionization region gives a molecular speed of $\sim 1.2 \times 10^5$ cm/s. More careful calculations cannot be made because the large ionization region obfuscates exact travel time. In contrast, material detected in the final extraction (travel time = 300 μs assuming $t = 0$) has a speed of 8×10^3 cm/s. Given these speeds, a NO_2 molecule in the first extraction with signal has a kinetic energy of 2800 cm^{-1} , whereas in the final extraction it has a kinetic energy of 12.5 cm^{-1} . Low kinetic energies for the later extractions are believed to be from the

tail of a warm distribution: the material in the final extraction represents 1% of the total material detected.

It is important to determine the identity of material that leaves the substrate. The ratio R_N has already been established in Section 4.3.1 and can be used to determine the dominant species in the ionization region. It is obvious from qualitative inspection of the NO_x^+ peaks that R_N starts off high and then decreases in later extractions and levels off. The average value of R_N at later times is 0.95, which is very close to the value of 0.9 found for N_2O_4 . Clearly, the source of material detected in the late time extractions is predominantly N_2O_4 with a small contribution from NO_2 .

4.3.3 N_2O_4 Thickness

The next trend examined was that of N_2O_4 thickness: we wanted to determine the point at which the amount of N_2O_4 irradiated gave enough signal to be detected without flooding our UHV system with NO_2 from long dosing times. This set of data is shown in Figure 4.6. The relatively linear trend shows that with increasing thickness, more material is being removed instead of a constant amount. It is assumed that there must be some point of saturation where the amount of material leaving the surface would level off, but that point is >100 L. This trend is indicative of the high fluence being used, but may also be a result of the heat gradient induced by the MgO heat sink. By increasing the overall thickness of the irradiated film, cooling rates are slower and may enable more N_2O_4 to leave the substrate.

4.3.4 Laser Energy

Laser energy may seem like a trivial trend to examine as logic would dictate that with higher fluence, the amount of desorbing species would increase until the absorption is saturated. This trend was indeed verified, as shown in Figure 4.7.

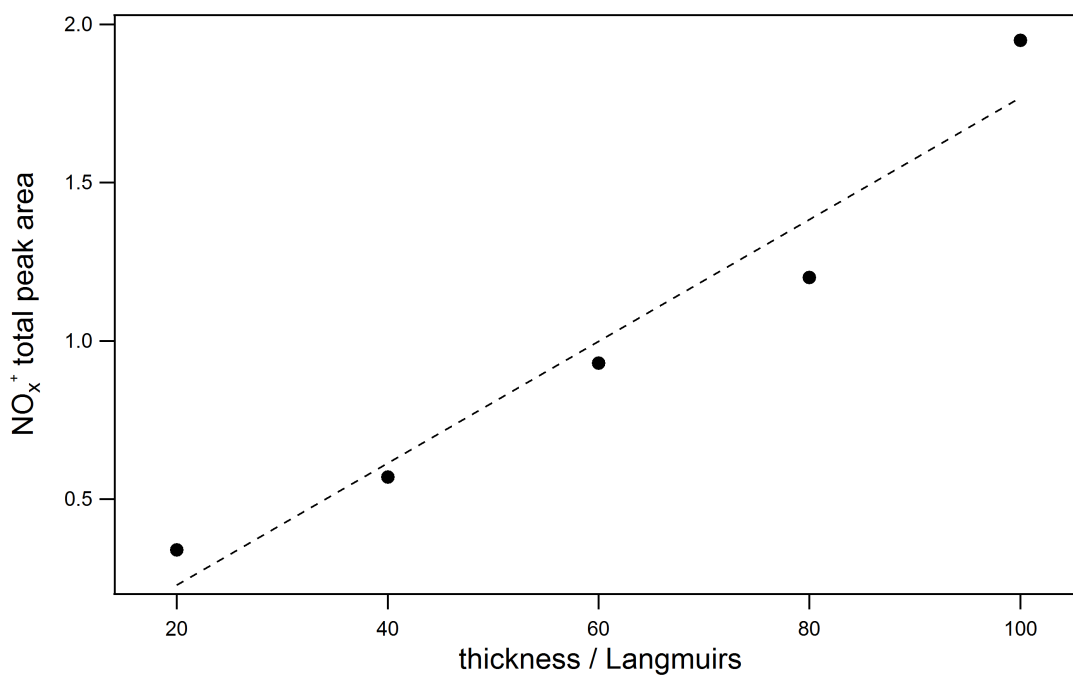


Figure 4.6: Sum of peak areas for NO^+ and NO_2^+ signals from laser ablation of 20-100 L N_2O_4 films grown on 300 ML of ASW. The signal increases with increasing thickness, indicating that absorption within the film hasn't been saturated in the range of thicknesses studied.

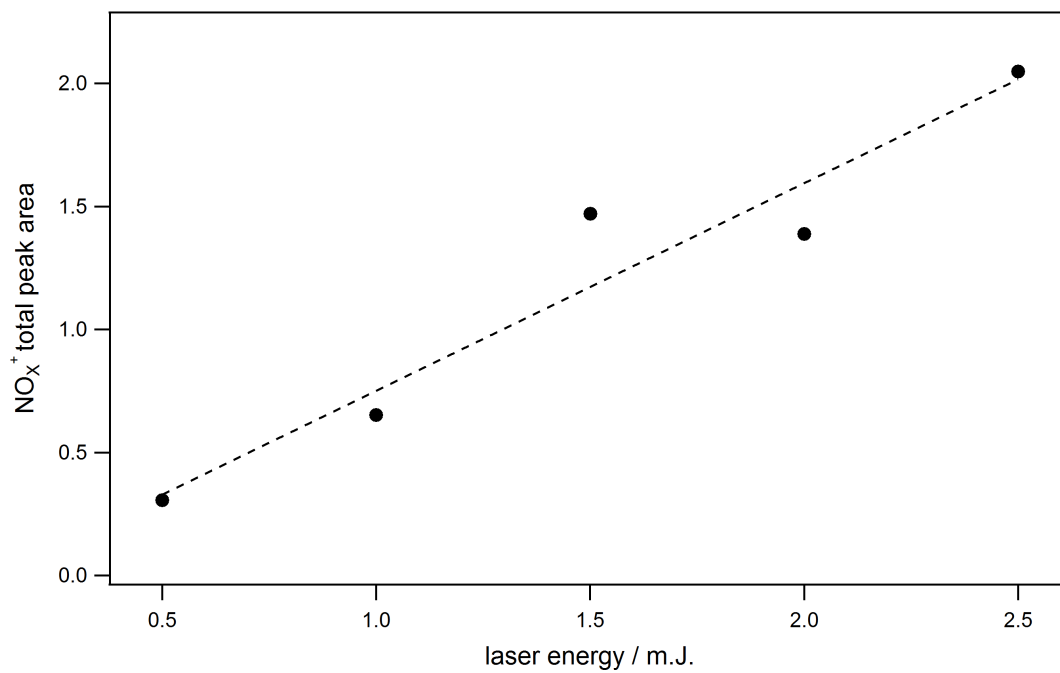


Figure 4.7: Sum of peak areas for NO⁺ and NO₂⁺ signals from laser ablation of 80 L N₂O₄ dosed on 300 ML H₂O. The signal generally increases with increasing laser energy.

Besides the most obvious result, there are some other trends that result from increased laser energy. One is the appearance of a very small peak at mass 18 that corresponds to H_2O^+ . This is significant as it shows that as more energy is introduced to the film, more mixing occurs at the ASW/ N_2O_4 interface. This allows for a small amount of the ASW underlayer to escape with the hot N_2O_4 fluid.

Another trend of note is the change in the R_N value with increasing energy. As discussed previously, R_N is a way of characterizing the fraction of material leaving the surface as N_2O_4 or NO_2 . Representative R_N values for the laser energies studied are summarized in Table 4.1. For all laser energies used with bare N_2O_4 films, R_N is at a maximum in the first extraction where resolved signal is detected (20 μs) and then decays and levels out at later extractions. In contrast, the maximum R_N value increases with increasing energy, with $R_N = 4.0$ for a laser energy of 2.5 mJ. This is above the R_N value of 3.1 calculated for the NO_2 gas phase spectrum. This reveals that there is a higher proportion of NO^+ being detected than if a majority of the material leaving the surface was NO_2 . The most likely source for the excess NO^+ is the presence of NO as a photoproduct after the initial irradiation. NO production would logically increase with increasing laser fluence, thus increasing the value of R_N .

The average R_N reached for the tail of the temporal profile also increases with increasing laser energy, topping out at 1.8. This is likely due to increased production of NO_2 as a photoproduct. At the lowest energy, the R_N is almost the same as that for N_2O_4 thermal desorption, which shows that that make-up of the plume is mostly N_2O_4 . While it seems extremely unlikely that excited material leaves the surface after ablation as N_2O_4 , this may be indicative of N_xO_y that has undergone collisions in the dense fluid that leaves the surface to reform the N_2O_4 dimer, resulting in the long tail. Furthermore, N_2O_4 molecules that absorb radiation can heat surrounding molecules that get carried out as the dimer (entrainment). With increasing laser energy, more NO_2 is formed. Also, higher energy collisions may be less likely to result in recombination by the time

the plume enters the ionization region. This would result in a higher proportion of NO^+ and a higher R_N value.

Table 4.2: R_N values for different laser energies at different extraction times. The changing ratio indicates that different species are the result of the desorption process, such as collisions; a consistent value would indicate all species are due to a fragmentation process that occurs in the ionization region.

Laser Energy (mJ)	R_N				
	20 μs	50 μs	100 μs	150 μs	200 μs
0.5	1.7	1.4	1.1	1.1	1.1
1.0	2.0	1.5	1.3	1.2	1.2
1.5	2.8	2.0	1.6	1.6	1.5
2.0	3.6	2.4	1.8	1.8	1.8
2.5	4.0	2.4	1.9	1.8	1.8

Lastly, increasing the laser energy results in the growth of a lumpy peak in the first extraction. This peak was observed in several experiments and was initially dismissed as sodium ions from light reflections. However, closer inspection of the signal revealed that it had structure; analysis of this will be discussed in the following section. The presence of this peak wasn't always consistent, but followed the general trend of increasing in size with increasing laser energy.

4.3.5 Multiphoton Effects

As just discussed, a broad peak with structure was often detected in the first extraction of experiments with N_2O_4 films without any material on top. Because of the timing set-up of our experiment, the first extraction contains material that has not been subjected to electron bombardment. As such, all material detected in the first extraction consist of molecules that are ionized during the laser ablation process. This was confirmed by conducting TOFMS experiments without the electron gun and still detecting

a fast, broad peak. Furthermore, the material must be leaving the surface at extremely high energy to be detected in the first 10 μs after the laser pulse. Assuming a distance between the surface and the nearest edge of the ionization region is 2.5 cm, the slowest speed for this material would be 2500 m/s.

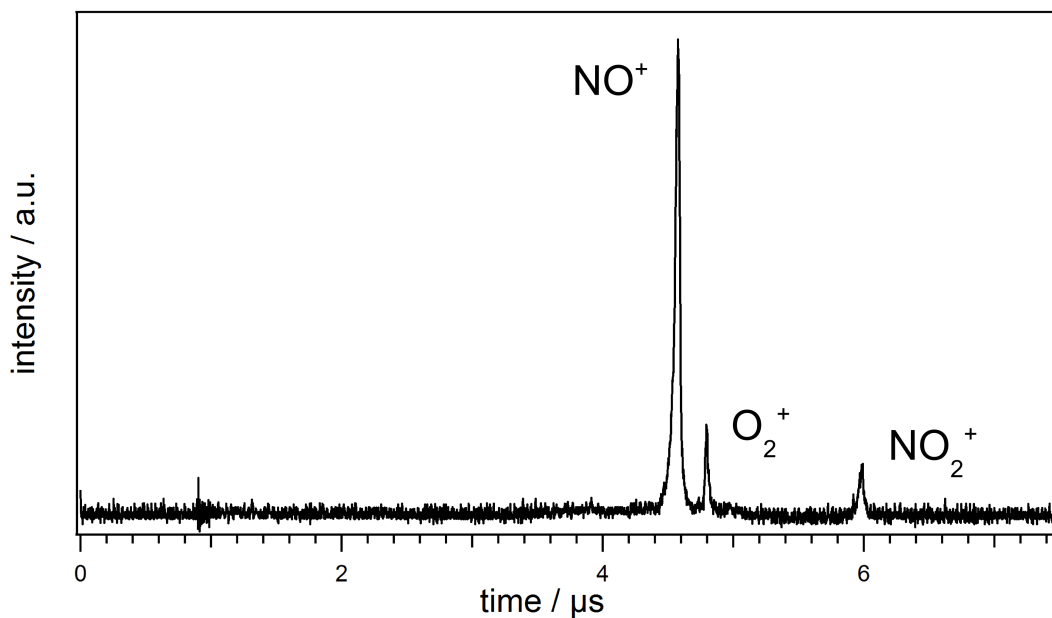


Figure 4.8: A representative resolved TOF spectrum of the fast ions from the first extraction. The spectrum has been shifted to account for the 2 μs delay. The peaks are labeled with probable species assignments.

Our typical TOFMS timing scheme was not sufficient to resolve the fast ion peak and instead was continuously extracting the material over the 3 μs extraction pulse. This was addressed by shortening the extraction time to 1 μs and introducing a 2 μs delay to select the “middle” of the fast ion plume. The ions present are NO^+ , NO_2^+ , and the recombination product O_2^+ . NO^+ is the dominant species by far, illustrating that this material is the result of multi-photon absorption. As stated previously, when N_2O_4 absorbs a UV photon, it will split into two excited monomers. In order to produce ionized NO, the NO_2 monomers would need to absorb another photon in a 1+1 REMPI-type process. The presence of this material speaks to the high fluence of the laser and how much energy is being introduced to the film. Detection of O_2^+ in this initial region

is also illuminating. As a recombination product, it needs to form from collisions of O atoms released from cracked N_2O_4 or NO_2 . In order for such collisions to occur, the material leaving the surface must be part of a dense fluid.

4.3.6 ASW Upper Layer Thickness

We were interested in how efficient the energy transfer would be between N_2O_4 and ASW. As the ASW underlayer absorbed the energy with little change, the next step was to make N_2O_4 /ASW “sandwiches.” These consisted of an ASW film with a layer of N_2O_4 dosed on top, and then another layer of ASW. This would also give us the ability to spatially select regions within the ASW to deposit energy, which was a unique approach to investigating energy transfer in ASW. While there is the possibility of diffusion of N_2O_4 into the porous ASW, it is most likely small enough to consider N_2O_4 a segregated layer. Furthermore, while reactions between ASW and N_2O_4 can occur, no product species (e.g. HNO_2 and HNO_3 [37, 38]) were detected by either TOFMS or FTIR spectroscopy. This agrees with N_2O_4 photodesorption experiments conducted by other groups [26, 39].

These data provided a wealth of insight into transport, as well as morphological changes in the ASW film. It was expected that increasing the thickness of the top ASW layer would result in decreased overall signal until no more N_2O_4 could escape because its transport through the ASW film would be quenched. Instead, we were able to dose 2400 ML of ASW on top of a 80 L N_2O_4 layer without seeing a noticeable decrease in signal. Also, there was a large water signal with a long tail that was present with every thickness tested. The thickest sandwiches will be discussed first.

For experiments carried out with a 2400 ML ASW top layer, very stochastic behavior was recorded in the temporal profile (Figure 4.9). Instead of the characteristic peak and decay seen with exposed N_2O_4 and thinner sandwiches, there are “bursts” of water monomer out to >1 ms. These molecules cannot be leaving the surface at $t = 0$ because the kinetic energies would be too low; this simple fact is illustrated by Figure 4.10. For

instance, a water molecule detected at $200 \mu\text{s}$ would have a kinetic energy $<10 \text{ cm}^{-1}$ if it left the surface at $t = 0$. This would clearly not be enough energy to escape the 100 K surface.

The only viable options to explain this result are: 1) the surface of the film loses thermal contact with the MgO and material is able to evaporate after $t = 0$; 2) very large water clusters are released and are detected as monomers due to evaporation in the ionization region; or 3) the fluid entering vacuum is so dense that collisions are frequent and the path of the material from the substrate to the ionization region is increased due to following a circuitous route. Due to the very fast transfer of heat to the substrate, the first option is considered implausible. The presence of large water clusters was appealing as it has been observed by other groups working on similar systems [40, 41], but we saw no evidence of smaller clusters (including the protonated dimer) in any of the experiments except for codeposition of N_2O_4 with ASW. As we know we are capable of detecting water clusters containing up to nine molecules [8], it seems unlikely that we wouldn't detect smaller clusters if we were releasing large clusters. Large clusters also do not fit with the isotope exchange detected when introducing a layer of D_2O (see Chapter 5). Instead, we believe the third option is the best fit with these data and will be presented as a potential mechanism.

When N_2O_4 is subjected to UV radiation, it heats up quickly and will break into two NO_2 molecules [9, 10]. In the case of a sandwich, this results in a trapped, very hot layer that is under extreme pressure. The hot N_2O_4 fluid mixes with the ASW immediately above it and creates fractures and crevices in the porous ASW through which it can now escape. As the N_2O_4 shoots up the fractures, it scrapes the walls and mixes with the surrounding water molecules. Once the fluid escapes, it can collide with the plumes of material escaping from neighboring fissures.

The fissures created through this mechanism are robust, as evident when comparing the first and second shot incident on the same spot. Example temporal profiles are shown in Figure 4.11. Rows 1-3 are data collected from sandwiches with upper ASW

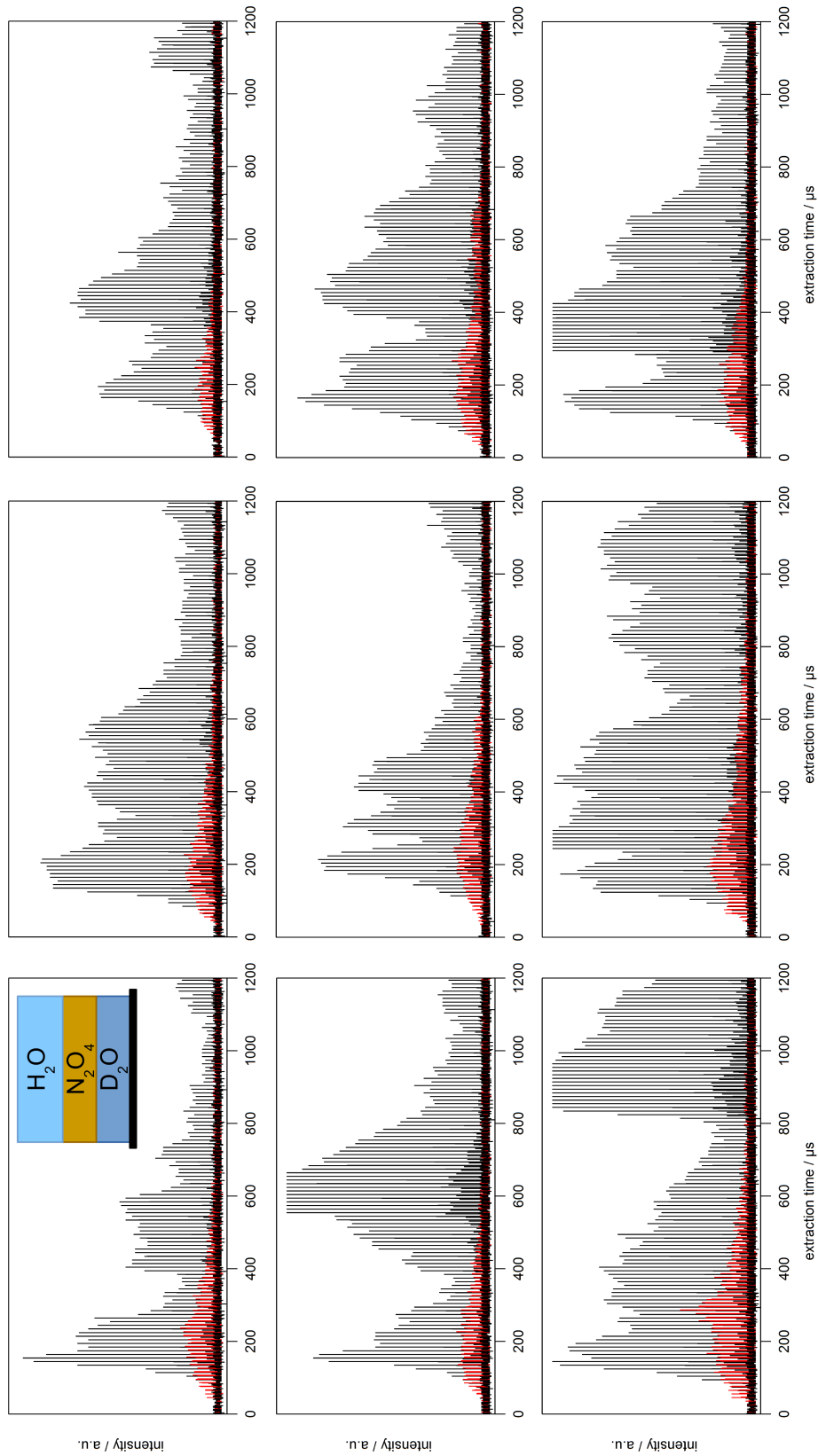


Figure 4.9: Nine first-pulse temporal profiles from a single 300 ML $D_2O/80$ L $N_2O_4/2400$ ML H_2O sandwich (1.0 mJ focused radiation, configuration shown in cartoon, depicted on common scale). For clarity, water signal is shown in black and NO_x^+ signal is shown in red. The irregularity of the water signal, particularly at long times, is indicative of nonthermal processes. The amount of signal at long times is considerable. It should also be noted that the NO_x^+ signal does not exhibit this behavior and decays with time.

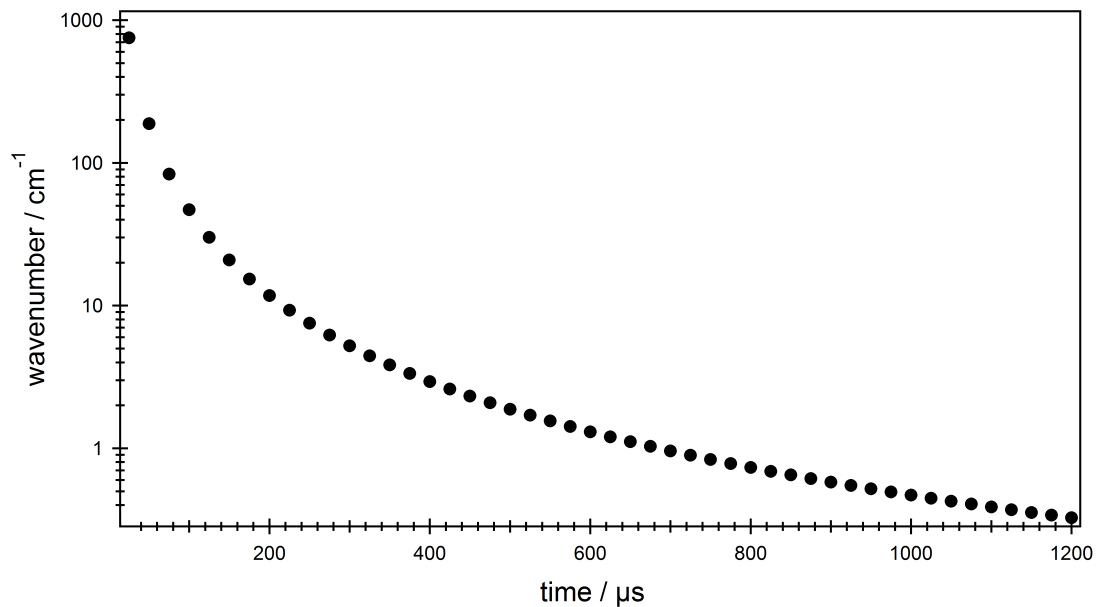


Figure 4.10: A water monomer's kinetic energy compared to its flight time, assuming the molecule left the surface at $t = 0$.

layer thicknesses of 600, 1200, and 2400 ML. The structure of the water monomer temporal profile after radiation incident on a sandwich (Figure 4.11) has a lumpy shape. The NO_x^+ peaks that arise from N_2O_4 , NO_2 , and NO (henceforth referred to as N_xO_y) have a different temporal profile form. The shapes of the temporal profile are revealing about transport of species through the ASW film.

The first pulse on a fresh film has a large water signal with a delayed and small NO_x^+ signal (black and red, respectively). The second pulse on the same spot results in a much larger NO_x^+ signal and a small, delayed water signal. The first pulse temporal profile reveals that the N_2O_4 is impeded by the upper ASW layer, resulting in a slower arrival time and fewer N_xO_y species escaping. As the fissures have formed during the first pulse, N_xO_y can easily escape during the second laser pulse without impediment as indicated by the fast arrival time and increased signal. Furthermore, less water monomer is liberated from the film with subsequent shots. Comparing the second pulse temporal profile with that of exposed N_2O_4 , shown in Figure 4.5, reveals similarities in

shape. This indicates that N_xO_y species from the second shot (and those following) are able to leave the film via an unobstructed path.

A quantitative comparison between first and second shot data can be made by examining R_N values for both profiles, shown in Figure 4.13; these values also reflect similarities. After the first few extractions, R_N averages out close to unity for first pulse data. This is much lower than the value for NO_2 , 3.1. We can conclude with some confidence that N_2O_4 is the dominant species leaving the film. The second shot R_N averages are slightly higher, which means that NO_2 has increased its contribution to the plume leaving the substrate. This is especially apparent in the first 10 extractions, where R_N values are very high. If we make the assumption that NO_2 is produced from photodissociation of gaseous N_2O_4 during the length of the laser pulse (10 ns), this would point to N_2O_4 being located near the surface on subsequent pulses.

FTIR was also utilized to get a rough estimate of how much water was being removed after ablation. Detecting material removal after a single pulse was not possible with the current InSb detector and fluence conditions. To ensure that we were only measuring depletion of the top ASW layer, D_2O was used for the bottom spacer. The laser beam waist was increased to 3 mm to ablate a sufficient area for FTIR measurements. As such, laser fluence was approximately an order of magnitude smaller than typical experimental conditions.

After 70 pulses on the center of the surface, there was a 14% decrease in the O–H peak (Figure 4.14a). It is also noteworthy that the O–D peak is practically identical in intensity before and after irradiation; this is consistent with our previously discussed results investigating the role of the ASW underlayer. Examination of the individual temporal profiles from this series of data show no evidence of a D_2O^+ peak ($m/q = 20$). There was also no observable increase in crystallinity of the ASW film, so morphological changes appear to be limited to the growth of fissures and any changes in crystallinity must be very small.

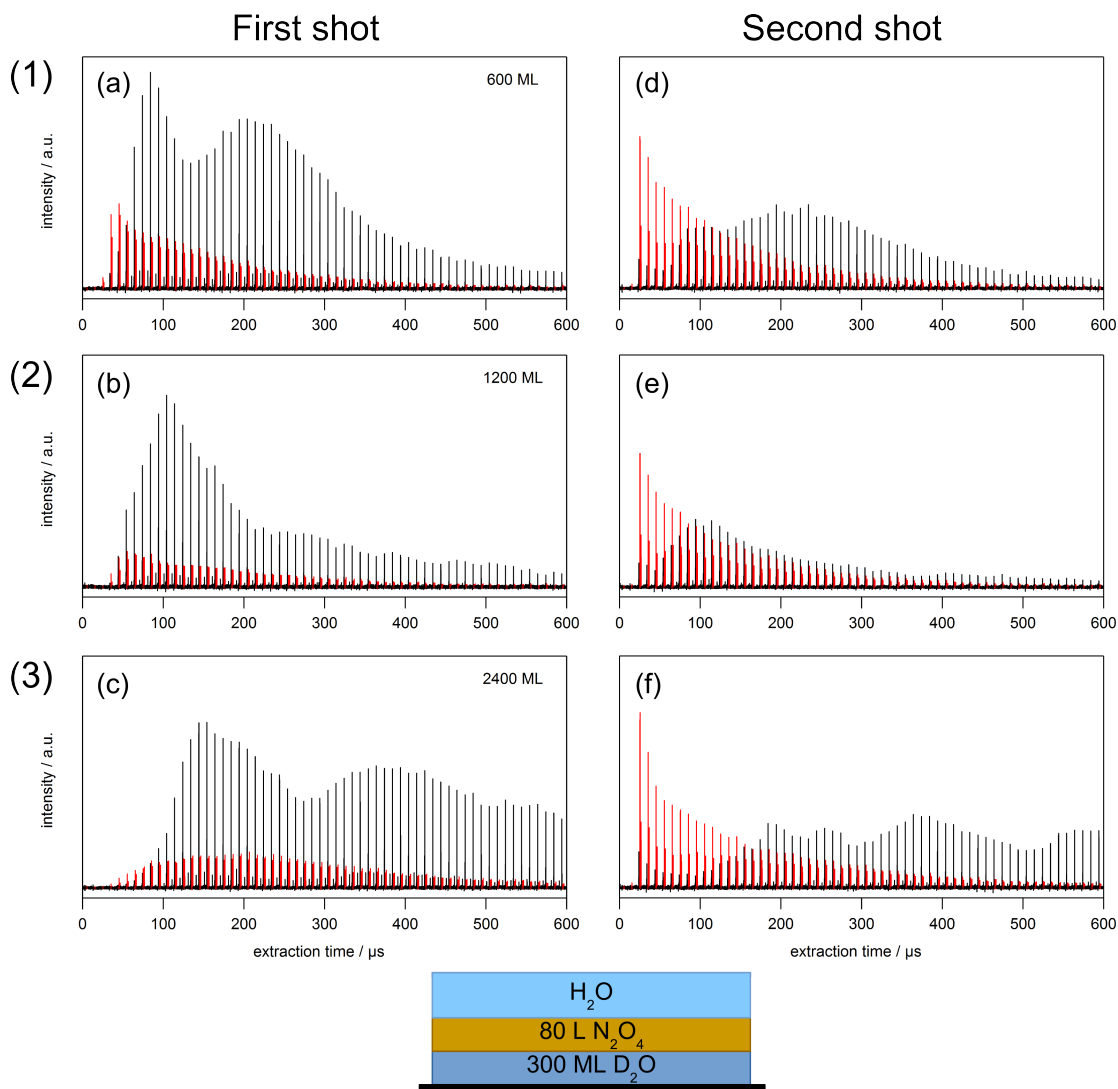


Figure 4.11: Temporal profiles comparing first and second incident pulses for upper H₂O layer thickness: (1) 600 ML, (2) 1200 ML, and (3) 2400 ML. Each profile is the average of nine individual profiles (1 mJ, 266 nm). Red peaks designate NO⁺ and NO₂⁺. Black peaks denote H₂O⁺, OH⁺, and H⁺. All temporal profiles are on the same ordinate scale. The lower ASW layer is 300 ML of D₂O and the N₂O₄ layer is 80 L (sample composition shown at bottom).

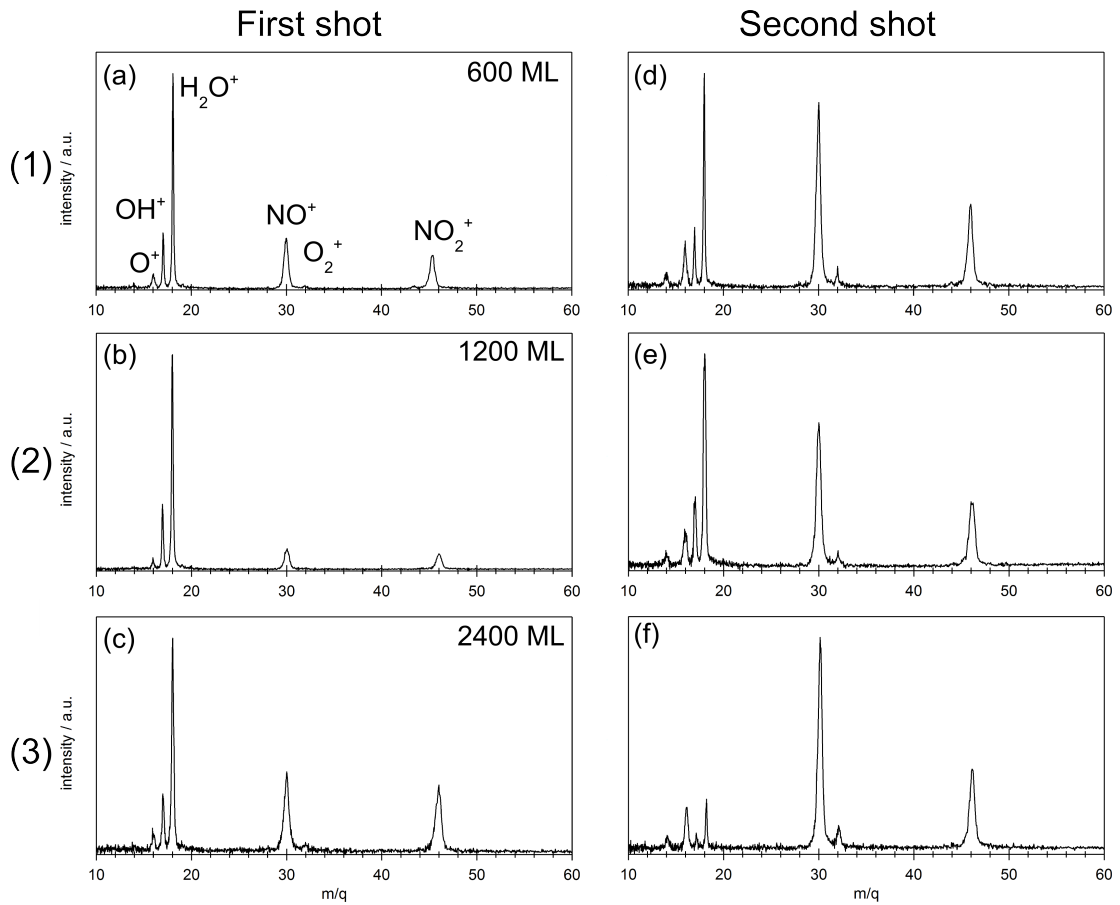


Figure 4.12: Mass spectra representing the 100 μs extraction from each temporal profile in Figure 4.11; refer to the caption of that Figure for composition details. The peaks in spectrum (a) have been labeled with ion assignments for clarity.

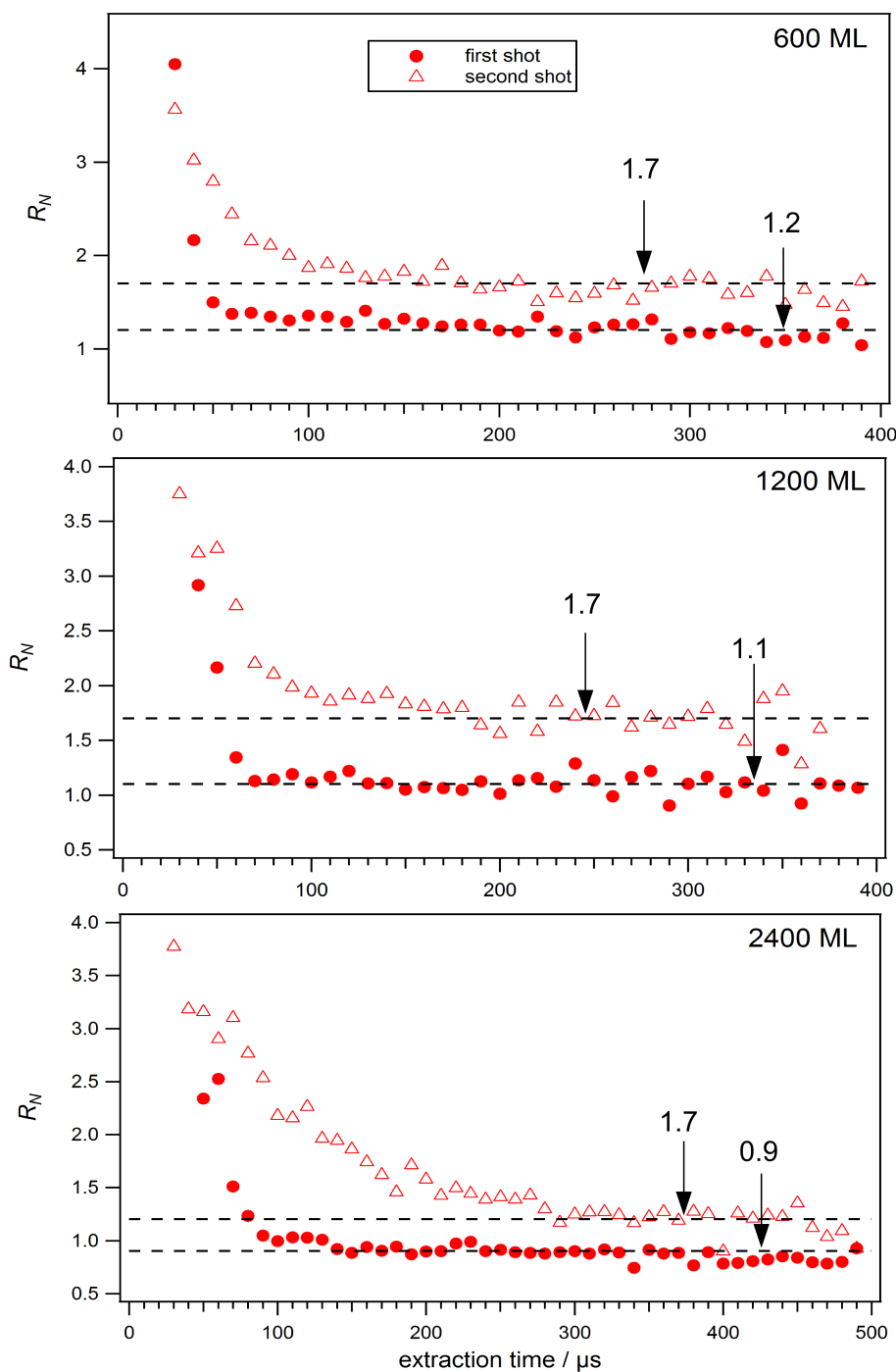


Figure 4.13: Plots of R_N for each extraction with good S/N from each temporal profile in Figure 4.11; refer to the caption of that figure for composition details. After the initial extractions, first pulse R_N values (filled circles) level off around unity. Second pulse R_N values (open triangles) follow the same qualitative trend but level off at higher values, indicating the presence of N_2O_4 in the surface region.

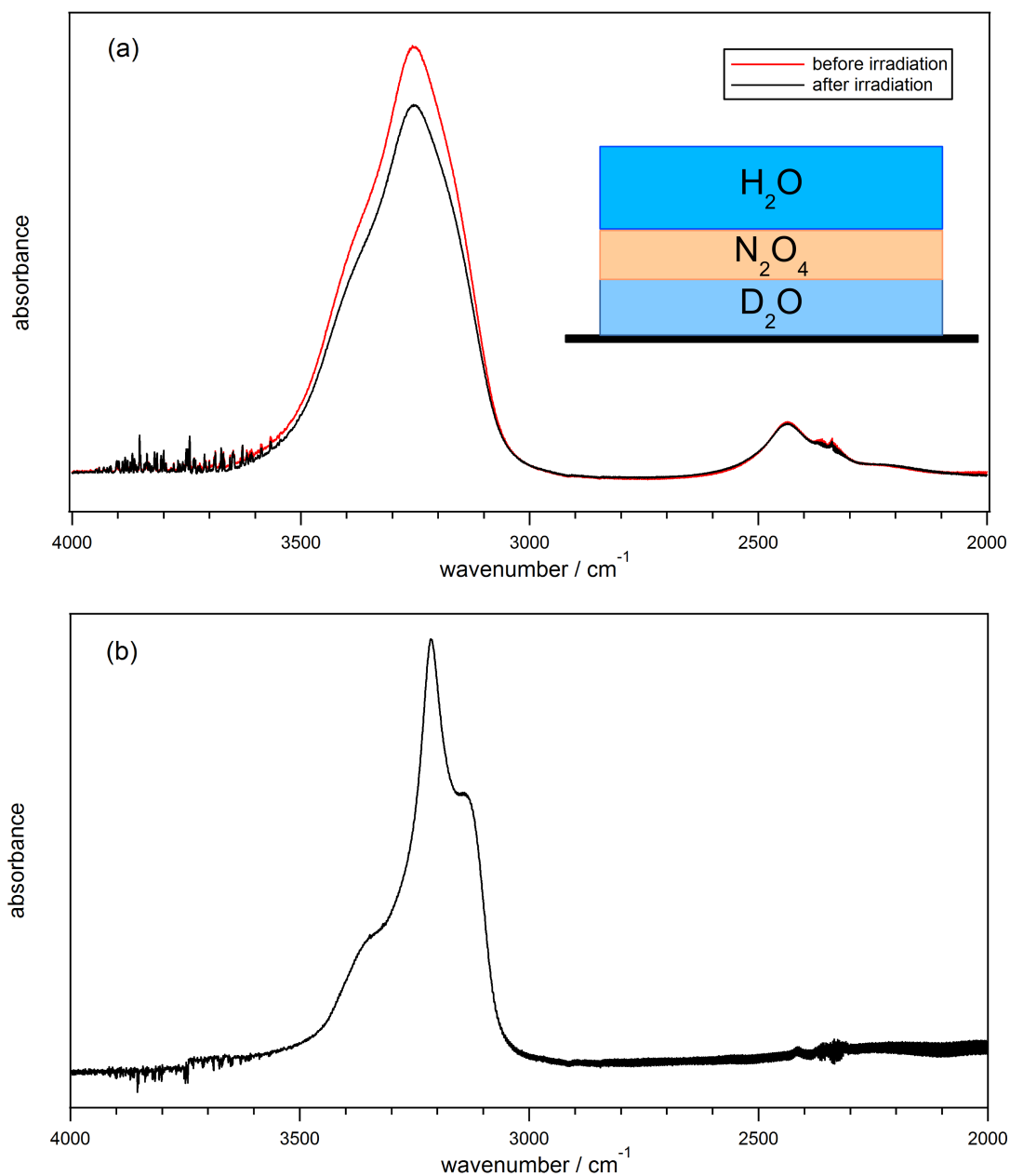


Figure 4.14: (a) Overlaid FTIR spectra of a 300 ML D₂O/80 L N₂O₄/2400 ML H₂O sandwich (configuration depicted in figure) before and after 70 shots of 6 mJ radiation. A 3 mm beam waist was used to ensure that a reasonable area was available for FTIR measurements. The red line represents the spectrum of the undisturbed film; the black line is the spectrum collected after irradiation. The O–D stretch peak centered at 2435 cm⁻¹ is virtually unchanged, but the O–H peak centered at 3250 cm⁻¹ is reduced by 14%. (b) 2400 ML of H₂O was annealed at 165 K for 10 minutes to induce crystallization and is shown for comparison. The “after” spectrum in (a) did not show any observable increase in crystallinity despite the prolonged exposure to laser radiation.

Another interesting feature of this data set was the presence of NO_x^+ signal in mass spectra even in the 70th pulse. Instead of removing all absorbing species after a few laser pulses, thin layers are removed. This is further evidence of the efficient cooling of the film via the MgO surface. While a hot fluid is created throughout the depth of the absorbing species when a film is irradiated, a gradient is quickly established that results in the recondensation of material at the bottom of the absorbing layer. In this way, the top of the N_2O_4 layer is removed with each pulse, but material gets more difficult to remove as the depth of the absorbing layer is probed.

4.3.7 High Fluence vs. Low Fluence

Almost all experiments conducted in this lab involving irradiation of ASW or species in ASW have used high-fluence beam arrangements. A majority of the experiments discussed in this dissertation were carried out using a 50 cm CaF_2 lens to focus the laser beam waist to <0.5 mm in conjunction with laser pulse energies of 1.0-3.0 mJ, giving a laser fluence at the surface of $\sim 1\text{-}3$ J/cm². In comparison, the few published papers that have looked at N_2O_4 photodesorption have used laser fluences almost a factor of 10 smaller [18, 29, 39]. Because we were seeing a “long tail” feature that other labs had not seen, the laser set-up was changed to accommodate low fluence. The CaF_2 lens was removed from the beam path, and the beam was trimmed to a 1 mm beam waist using an iris. Due to the larger beam size, a grid of four spots was used instead of nine to ensure that each laser pulse was incident on an undisturbed section of the deposited film.

The first comparison must be made between the R_N ratios for high fluence vs. low fluence. Low fluence experiments have a much higher population of NO_2^+ , as shown in Figure 4.15. Another noticeable feature in the low fluence data is impact of an ASW spacer. With low fluence, the signal increase is even more significant at around 600%. This strengthens the argument that ASW is acting as an effective insulator to the thermal properties of MgO.

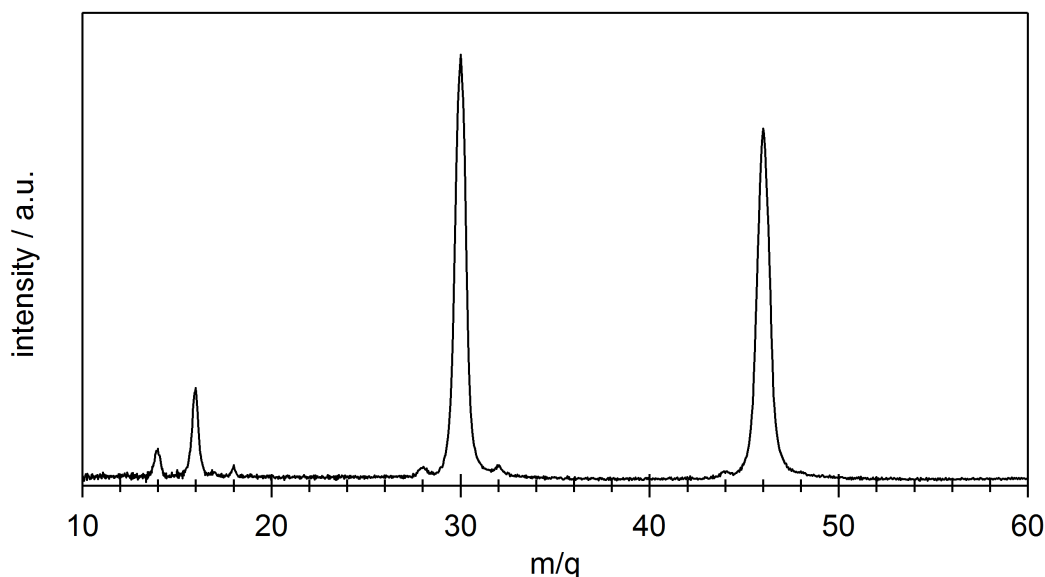


Figure 4.15: Averaged mass spectrum from extractions 2-11 (20-110 μs) of data from a low fluence experiment (0.2 J/cm^2) with the same film composition as Figures 4.4b and 4.5 (300 ML ASW/80 L N_2O_4). The difference in the $\text{NO}^+/\text{NO}_2^+$ ratio compared to Figure 4.5 is striking.

Finally, an ASW/ N_2O_4 sandwich was also subjected to low fluence. We were able to detect small signal, but it was very slow and was never the result of the first laser pulse incident on a film. This was revealing about the nature of N_xO_y species' escape from under the top ASW layer. As discussed in the previous section and further fleshed out in Section 4.4, the proposed mechanism for escape is travel of hot N_xO_y species through ASW channels and out into vacuum. In the low fluence situation, this is clearly not happening after one pulse. Instead, the N_2O_4 is only able to travel a certain distance up through the ASW layer before recondensing on walls and/or forming plugs in the channels, preventing escape. Then, on subsequent shots, N_2O_4 is able to escape because it is closer to the surface of the ASW. Tellingly, the shape of the temporal profile resembled that of exposed N_2O_4 such as in Figure 4.4, which follows from the proposed mechanism. Furthermore, this indicates that there is a fluence cut-off for N_2O_4 escape from sandwiches; determining this boundary requires further experimentation.

4.3.8 N₂O₄ Codeposition

Past experiments in this lab involved a codeposition of ASW and another species [8]. However, ASW was the absorbing species, resulting in a relatively uniform initial distribution of energy throughout the irradiated area. In those experiments, we typically saw protonated clusters along with protonated monomer. In contrast, clusters had not been detected in experiments using N₂O₄ as the absorbing species. We were also interested in seeing if N₂O₄ signal would decrease due to isolated NO₂ molecules depositing at lower concentrations.

A representative mass spectrum is shown in Figure 4.16. With codeposition of a ~1:2 ratio of N₂O₄ to ASW (based on Langmuirs), the first evidence of protonated clusters was detected. The ablation mechanisms laid out by Perez and Lewis [42] provide a likely explanation for this result. When the N₂O₄ is deposited in a single layer, it results in a high-energy environment that should only give monomers. The small presence of clusters in the codeposition experiments indicates that a slightly “softer” desorption process is occurring. Also, decreasing the ratio to 1:9 still gave significant N_xO_y signal after irradiation. This indicates that H₂O does not significantly inhibit dimer formation; indeed, dimerization may be encouraged within the pores of ASW.

It is worthwhile to note that products due to chemical reaction, such as HNO₃, are still not detected despite codeposition allowing for maximum interaction between N₂O₄ and H₂O. This is apparent from the absence of any peak at mass 62. We tentatively conclude that if chemical reactions occur within the film, the concentration of product species is small.

4.4 Discussion

Little previous work has been done on photodesorption of ASW via a dopant molecule. One system that was looked at in depth by the group of M. R. S. McCoustra was that of UV-irradiated benzene and water [43–45]. Their set-up included a sapphire

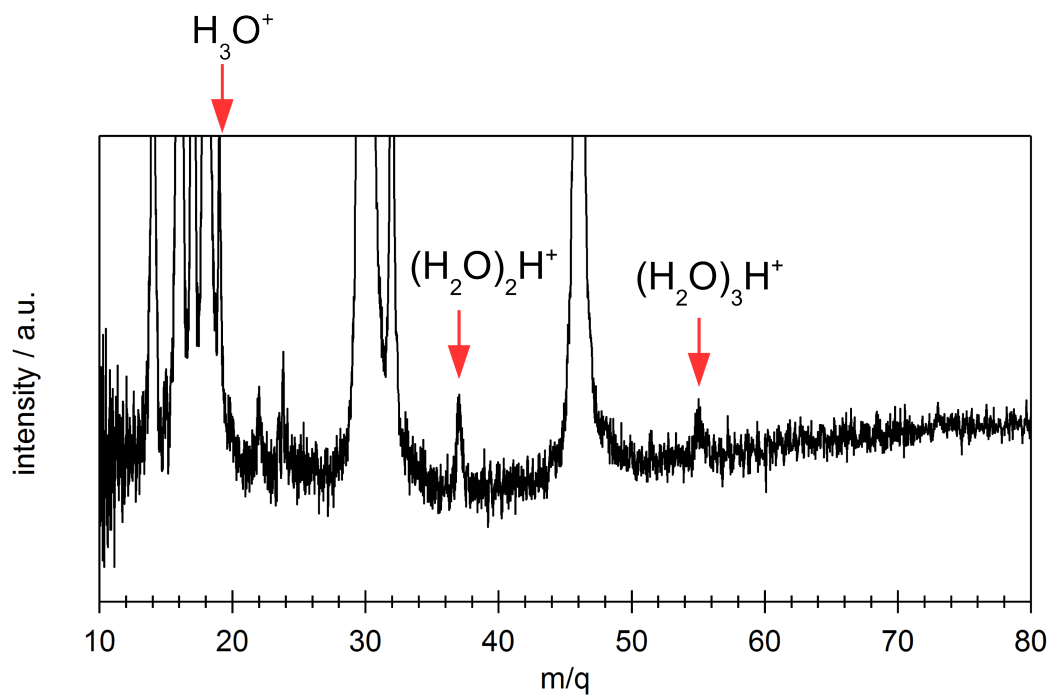


Figure 4.16: Expanded mass spectrum of 80 L N_2O_4 codeposited with 240 ML of ASW and irradiated with focused 1.0 mJ radiation. Five first-shot experiments from the film have been averaged to improve S/N. While small, clusters up to the protonated water tetramer were visible. No protonated species were detected in any of the experiments where N_2O_4 was deposited as a discrete layer. It is also important to note that there is no signal at $m/q = 62$, which would indicate the presence of NO_3^+ .

surface and thinner layers of material (several nm thick compared to hundreds in the present work). Based on their results, they defined three processes for photo-induced desorption: direct absorbate-mediated, indirect absorbate-mediated, and substrate mediated (this process was due to their sapphire substrate absorbing slightly in the UV). As MgO does not absorb in the UV, we can ignore the last process and focus on the first two. In the case of direct absorbate-mediated desorption, it is simply defined: material that is excited by the incident radiation desorbs. When applied to our system, N_2O_4 is desorbed via this mechanism as the 266-nm radiation excited the afore-mentioned electronic transition. Indirect absorbate-mediated desorption, on the other hand, is when energy is transferred from the excited molecules to molecules nearby in the film. This process describes the H_2O desorption that we see (though the interpretation of this is much more complicated than this definition implies).

Putting together a model for the data presented in this chapter that reconciles the various observables into a cohesive whole was a daunting task. It is important to begin with a summary of the key findings from the previous sections. Heating N_2O_4 multilayers grown on a 100 K MgO(100) substrate with 266-nm radiation results in desorption of material. While the 266-nm irradiation of gaseous N_2O_4 results in photolysis and the production of NO_2 with translational and internal energy, the dense environments of our systems favor recombination accompanied by the evolution of heat on a short time scale. Therefore, N_2O_4 and its surroundings are heated by the laser pulse. The efficient removal of material is increased when the N_2O_4 layer is grown atop an ASW layer because the ASW acts as a thermal insulator between the absorbing material and the substrate. Exposed N_2O_4 has a qualitatively different temporal profile than buried N_2O_4 , which can be examined quantitatively by looking at the value of R_N as defined in Section 4.3.1.

At high fluence ($\geq 1 \text{ J/cm}^2$), the presence of an ASW film on top of the N_2O_4 doesn't significantly impede the desorption of N_xO_y species. Despite increasing the upper ASW layer to thicknesses of 2400 ML, desorption of N_2O_4 was robust. It was determined that

the NO_x^+ species detected originated from N_2O_4 due to the small R_N values that resembled that of the pure N_2O_4 mass spectrum. Accompanying N_2O_4 desorption was water monomer, which differed from previous experiments conducted in our lab that detected protonated water clusters. The total signal of water monomer increased with increasing ASW thickness, which was counter to expectations. The lack of protonated clusters points to a different mechanism for material release into vacuum. Our system also differs from the widely studied “molecular volcano” peak that is also associated with ejection of molecules from ASW [6, 46]. The latter occurs after homogenous thermal heating of ASW and embedded species until the crystallization temperature is reached. The experiments presented in this dissertation involve extremely rapid, pulsed heating of a layer of material on or embedded in ASW, which triggers transport of hot fluid to vacuum.

Finally, low fluence ($<0.2 \text{ J/cm}^2$) radiation instigates desorption of N_xO_y species, but only after 2 or 3 laser pulses incident on the same area. The set of data taken as a whole reveals that excited material escapes to vacuum via cracks in the ASW film. A cohesive model is described below, starting with a discussion of the unusually long time scales measured.

4.4.1 Time Scales

It was surprising when we first measured significant signal at $300 \mu\text{s}$; it was even more surprising when the time scale was expanded to 1.2 ms and signal was still considerable. The “lumpy” character of the water monomer temporal profile for thick sandwiches was also intriguing in its variability in structure, as well as its reproducibly lumpy character. It was clear that H_2O molecules couldn’t have enough energy to leave the surface at $t = 0$ and arrive in extractions after even $50 \mu\text{s}$. For a water molecule arriving in the 1.2 ms extraction assuming no collisions, the kinetic energy would be 0.33 cm^{-1} . Another possibility would be that water monomer leave the film at $t > 0$. This desorption mechanism would require a loss of thermal contact with the 100 K

MgO substrate, which was determined to be unlikely after heat calculations were conducted [47]. Finally, the release of large clusters could produce bursts of signal at longer times because they will have long transit times and may evaporate in the beam. However, the complete absence of even the protonated dimer in any mass spectra (excepting the codeposition experiments) refutes this mechanism. Instead, we propose that water molecules undergo collisions before entering the ionization region. Many collisions would result in a complicated flight path from the surface to the ionization region, which is detected as a long flight time. This is consistent with a high fluid density regime and a high density of fissures, which is expanded on in the next section.

4.4.2 Fissures

An intriguing result is the temporal profile of N_xO_y signal in a sandwich film comparing the first laser pulse to subsequent pulses on the same location. The profile for the first pulse incident on sandwiches with an upper layer thickness >600 ML shows a delay in the release of material, with a signal maximum from N_xO_y at 100-150 μ s. Such a distribution is logical, as the impeding layer of ASW would sap energy from the escaping N_xO_y species as they create pathways to escape to vacuum. The formation of fissures is favored because ASW must maintain its macroscopic column density. The profile of N_xO_y from the second and subsequent laser pulses resembles that of exposed N_2O_4 films upon irradiation. This demonstrates that once fissures are formed, they do not collapse or become plugged. As such, they are accessible pathways for transport of the remaining N_2O_4 to vacuum when excited by subsequent pulses incident on the same spot. Fissures must also be relatively direct pathways from the N_2O_4 layer to vacuum, as too many twists and turns would result in N_2O_4 freezing out on the walls.

The hot fluid released from fissures can collide with material released from neighboring fissures (Figure 4.17). The density of fissure openings per unit area in combination with the density of the fluid released necessitates the occurrence of collisions. We can assume that the hot fluid traveling through fissures is dense as low density fluid

would easily freeze to the walls and be unable to escape to vacuum in any significant amount. Collisions above the film will change the trajectories of species, giving a spatial inhomogeneity in the ionization region. Such an environment would explain the characteristic lumps seen at long times in temporal profiles.

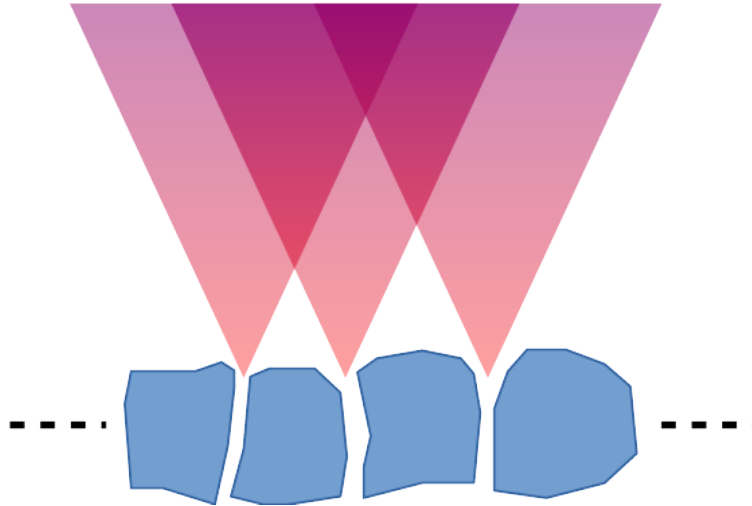


Figure 4.17: A cartoon depiction of how material expelled from neighboring fissures may interact.

Increasing the thickness of the upper ASW layer does not significantly impede the escape of N_xO_y species. However, it does increase the amount of water that enters vacuum upon irradiation. This follows from the fact that the heated fluid must travel over a longer fissure pathway. As the fluid travels through fissures, it scrapes the walls and frees water monomer.

Low fluence experiments still exhibit material release, but require two or more laser pulses to instigate release. While this clearly points to a fluence threshold that needs to be achieved in order for material to escape the film in one pulse, the fact that material can still be desorbed points to arrested transport within the ASW after termination of the laser pulse. Otherwise stated, hot N_2O_4 moves upward in the film, but does not have enough energy to complete the journey to vacuum and recondenses at a higher level in the film. A second (or third) laser pulse allows for continued transport and escape of material that has already moved nearer the surface of the ASW layer.

Hot fluid is able to reach vacuum with a single laser pulse at high fluence. Due to the high thermal conductivity of MgO, cooling efficiency is high enough that any material left in the fissures after the cessation of a laser pulse would quickly recondense in the film. Based on the assumption that material that escapes the film must do so before the end of the laser pulse, a rough calculation can be made of minimum fluid speed. Given a 1000-nm thick ASW layer, hot fluid travelling through fissures must have a speed of 100 m/s or more in order to escape the film. With thinner samples, lower speeds are necessary for transport from the buried layer to the surface and so more N_xO_y can escape to vacuum. This is consistent with the observed decrease in N_xO_y signal for sandwiches with increasing upper ASW layer thickness.

4.5 Conclusions

An experimental technique has been presented for studying energy transfer in layered films of ASW and N_2O_4 that gives insight into molecular transport. 266-nm focused radiation excited an electronic transition in N_2O_4 which quickly degraded to heat. Uncovered N_2O_4 was desorbed with ease; covered N_2O_4 in a “sandwich” configuration created structural changes in the upper ASW layer and induced the ejection of water monomer along with release of N_xO_y species.

The nature of the data prevents the development of a definitive, quantitative model. However, a qualitative understanding of the results is presented that reconciles the experimental trends uncovered in this study. Building a robust quantitative model would require further investigations in the laboratory, coupled with computational simulations, which is left as future work.

To summarize, the model presented in this chapter is as follows: Laser heating of a buried N_2O_4 layer creates fissures in the upper ASW layer to enable transport to vacuum. Dense fluid escapes through these fissures without freezing on the walls, resulting in jets of material spewing out of the film. The creation of fissures is irreversible, as evidenced by continued removal of N_2O_4 after the first laser pulse. Increasing the

thickness of the upper ASW layer does not significantly impede the escape of N_xO_y species; it does increase the amount of water that enters vacuum upon irradiation due to greater fissure area. Long tails of material detected at unphysical times after the initial laser pulse are the result of molecular collisions above the film surface. Such collisions occur due to the prevalence of fissures combined with the high density of the escaping fluid.

To probe these morphological changes more effectively, some equipment changes will need to be implemented for increased detection abilities. Furthermore, generating fissures of known dimensions would be valuable. Preliminary experiments using gold nanoparticles have been attempted and may help progress understanding of this system.

Chapter References

- [1] Burton, E.; Oliver, W. *Nature* **1935**, *135*, 505–506.
- [2] Angell, C. *Annu. Rev. Phys. Chem.* **2004**, *55*, 559–583.
- [3] Hama, T.; Watanabe, N. *Chem. Rev.* **2013**, *113*, 8783–8839.
- [4] Burke, D.; Brown, W. *Phys. Chem. Chem. Phys.* **2010**, *12*, 5947–5969.
- [5] May, R.; Smith, R.; Kay, B. J. *Phys. Chem. Lett.* **2012**, *3*, 327–331.
- [6] May, R.; Smith, R.; Kay, B. J. *Chem. Phys.* **2013**, *138*, 104501.
- [7] May, R.; Smith, R.; Kay, B. J. *Chem. Phys.* **2013**, *138*, 104502.
- [8] Rebolledo–Mayoral, O.; Stomberg, J.; McKean, S.; Reisler, H.; Wittig, C. J. *Phys. Chem. C* **2012**, *116*, 563–569.
- [9] Bach, W.; Breuer, H. *Faraday Discuss. Chem. S.* **1974**, *58*, 237–243.
- [10] Kawasaki, M.; Kasatani, K.; Hiroyasu, S.; Shinohara, H.; Nobuyuki, N. *Chem. Phys.* **1983**, *78*, 65–74.
- [11] Hurford, A.; Helfenstein, P.; Hoppa, G.; Greenberg, R.; Bills, B. *Nature* **2007**, *447*, 292–294.
- [12] Porco, C.; DiNino, D.; Nimmo, F. *Astron. J.* **2014**, *148*, 45.
- [13] Hawkins, S.; Kumi, G.; Malyk, S.; Reisler, H.; Wittig, C. *Chem. Phys. Lett.* **2005**, *404*, 19–24.
- [14] Korolik, M.; Suchan, M.; Johnson, M.; Arnold, D.; Reisler, H.; Wittig, C. *Chem. Phys. Lett.* **2000**, *326*, 11–21.
- [15] Andrews, B.; Anderson, A. J. *Chem. Phys.* **1981**, *74*, 1534–1537.
- [16] Loparo, J.; Roberts, S.; Tokmakoff, A. J. *Chem. Phys.* **2006**, *125*, 194521.
- [17] Vandaele, A.; Hermans, C.; Simon, P.; Carleer, M.; Colin, R.; Fally, S.; Mérienne, M.; Jenourvriër, A.; Coquart, B. *J. Quant. Spectrosc. Radiat. Transfer* **1998**, *59*, 171–184.
- [18] Dixon-Warren, S. J.; Jackson, R.; Polanyi, J.; Rieley, H.; Shapter, J.; Weiss, H. J. *Phys. Chem.* **1992**, *96*, 10983–10994.
- [19] Hasselbrink, E.; Jakubith, S.; Nettesheim, S.; Wolf, M.; Cassuto, A.; Ertl, G. *J. Chem. Phys.* **1990**, *92*, 3154–3169.

- [20] Mélen, F.; Pokorni, F.; Herman, M. *Chem. Phys. Lett.* **1992**, *194*, 181–186.
- [21] Hisatsune, I.; Miller Jr., P. *J. Chem. Phys.* **1963**, *38*, 49–54.
- [22] Tyndall, G.; Stedman, K.; Schneider, W.; Burrows, J.; Moortgat, G. *J. Photochem.* **1987**, *36*, 133–139.
- [23] Ogai, A.; Qian, C.; Iwata, L.; Reisler, H. *Chem. Phys. Lett.* **1988**, *146*, 367–374.
- [24] Bai, Y.; Ogai, A.; Qian, C.; Iwata, L.; Segal, G.; Reisler, H. *J. Chem. Phys.* **1989**, *90*, 3903–3914.
- [25] Qian, C.; Ogai, A.; Iwata, L.; Reisler, H. *J. Chem. Phys.* **1990**, *92*, 4296–4307.
- [26] Rieley, H.; McMurry, D.; Haq, S. *Faraday Trans.* **1996**, *92*, 933–939.
- [27] Russ, F. *Z. Phys. Chem.* **1914**, *82*, 217–222.
- [28] Hisatsune, I. *J. Phys. Chem.* **1961**, *65*, 2249–2253.
- [29] Rieley, H.; Colby, D.; McMurry, D.; Reeman, S. *J. Phys. Chem. B* **1997**, *101*, 4982–4991.
- [30] Linstrom, P., Mallard, W., Eds. NIST Chemistry WebBook, NIST Standard Reference Database Number 69., <http://webbook.nist.gov> (accessed 05/04/2015).
- [31] Y.K., K.; Rudd, M. *Phys. Rev. A* **1994**, *50*, 3954–3966.
- [32] Slack, G. A. *Phys. Rev.* **1962**, *126*, 427–441.
- [33] Andersson, O.; Inaba, A. *Phys. Chem. Chem. Phys.* **2005**, *7*, 1441–1449.
- [34] English, N.; Tse, J.; Gallagher, R. *Phys. Rev. B* **2010**, *83*, 092201.
- [35] English, N.; Tse, J. *Phys. Rev. B* **2011**, *83*, 184114.
- [36] Yang, R.; Gudipati, M. *J. Chem. Phys.* **2014**, *140*, 104202.
- [37] Kim, S.; Kang, H. *J. Phys. Chem. Lett.* **2010**, *1*, 3085–3089.
- [38] Lignell, H.; Varner, M.; Finlayson-Pitts, B.; Benny Gerber, R. *J. Chem. Phys.* **2012**, *405*, 52–59.
- [39] Susa, A.; Koda, S. *J. Atmos. Chem.* **2003**, *43*, 197–217.
- [40] Bar-Nun, A.; Dror, J.; Kochavi, E.; Laufer, D. *Phys. Rev. B* **1987**, *35*, 2427–2435.

- [41] Thrower, J.; Burke, D.; Collings, M.; Dawes, A.; Holtom, P.; Jamme, F.; Kendall, P.; Brown, W. A.; Clark, I.; Fraser, H.; McCoustra, M.; Mason, N.; Parker, A. *Astrophys. J.* **2008**, *673*, 1233–1239.
- [42] Perez, D.; Lewis, L.; Lorazo, P.; Meunier, M. *Appl. Phys. Lett.* **2006**, *89*, 141907.
- [43] Thrower, J.; Burke, D.; Collings, M.; Dawes, A.; Holtom, P.; Jamme, F.; Kendall, P.; Brown, W.; Clark, I.; Fraser, H.; McCoustra, M.; Mason, N.; Parker, A. *Astrophys. J.* **2008**, *673*, 1233–1239.
- [44] Thrower, J.; Collings, M.; McCoustra, M.; Burke, D.; Brown, W. A.; Dawes, A.; Holtom, P.; Kendall, P.; Mason, N.; Jamme, F.; Fraser, H.; Clark, I.; Parker, A. *J. Vac. Sci. Technol., A* **2008**, *26*, 919–924.
- [45] Thrower, J.; Abdulgalil, A.; Collings, M.; McCoustra, M.; Burke, D.; Brown, W.; Dawes, A.; Holtom, P.; Kendall, P.; Mason, N.; Jamme, F.; Fraser, H.; Rutten, F. J. *J. Vac. Sci. Technol., A* **2010**, *28*, 799–806.
- [46] Smith, R.; Huang, C.; Wong, E.; Kay, B. *Phys. Rev. Lett.* **1997**, *79*, 909–912.
- [47] McKean, S. M. Energy Transfer in Amorphous Solid Water: Light-Mediated Expulsion of N₂O₄ Guest Molecules., Ph.D. Thesis, University of Southern California, 2015.

Introducing a Third Species: Molecular Transport and Isotope Exchange

There are inherent limitations to the experimental approach described in this dissertation. We were unable to measure the excitation state of desorbed species, or to investigate structural changes on the surface except with FTIR spectroscopy. FTIR spectroscopy itself is limited in the types of changes we can detect: the amount of material removed, bulk changes, and species with strong peaks in the 1850-7000 cm^{-1} detection range. This last limitation meant that we had to focus on changes in the O–H stretch signal, as N_2O_4 only has one weak combination band that fell in the detection region and was mainly used as an indicator of the presence or absence of the species itself. To address the subtleties of transport within the ASW sandwiches, a set of molecules were introduced to profile the effect of energy transfer at different depths during the irradiation process.

5.1 Introduction

Building a model for molecular transport in amorphous solid water has proven to be a difficult task due to the variety of morphologies of ASW and its complex interactions with guest molecules [1–3]. Work done by Kay and coworkers has shown that a thermally-induced “molecular volcano,” where guest species are energetically ejected

from an ASW matrix upon heating, is due to top-down growth of fissures during crystallization [4]. These cracks provide a pathway from the pores containing the trapped species to vacuum; material that is not along the path of these fissures remains trapped in the crystalline ice until it can co-desorb with the water bulk at a higher temperature.

Another method of transport that still requires study is the “bottom-up” pathway. The groups of Kay [5] and Bar-Nun [6] have also investigated this phenomenon, which is the mechanism attributed to bursts of material that are released below crystallization temperature upon heating. The tentative explanation put forth is the structural collapse of ASW due to extreme pressure of the escaping material during heating. The work described in the previous chapter presented a model where laser-heating of a buried stratum induced catastrophic changes in the upper ASW layer with resulting fissures allowing the release of a hot fluid into vacuum. However, working with only two species gave somewhat limited insight into how energy is transferred through the film during this process. This chapter focuses on studies where a third species was introduced to better probe energy transfer in ASW sandwiches. By placing a thin film of another material in the sandwich, depth profiling can be carried out.

Carbon dioxide and acetylene are attractive probe molecules because they are readily available. Furthermore, both molecules are known to exist in the ISM and may interact with ASW on the surface of dust grains in molecular clouds [7]. Carbon dioxide as a guest molecule has been utilized previously by this lab in multiple studies [8, 9] and most recently was found to be preferentially released when the surrounding ASW matrix was disturbed with laser radiation [10]. This mobility can be exploited in order to learn more about structural changes within the system studied herein.

Alternatively, deuterated water (D_2O) is useful as an isotopically marked species that can be differentiated from H_2O but does not affect the properties of a film significantly. However, these two types of water can undergo proton exchange to form HDO:



The Grotthuss mechanism explains this process through proton-hopping; excess protons from the autoionization of water travel along a cluster of water molecules by “hopping” from molecule to molecule [11]. In the solid phase, isotope exchange is not as facile but follows similar rules. It is mediated by defects that migrate through the solid that originate as excess protons or Bjerrum defects [12]. Bjerrum defects are a distortion of a normal hydrogen bond and exist as two varieties: D defects have two protons, L defects have no protons. Also, the rate of H/D exchange can be increased through the introduction of H^+ or OH^- [13–15]. If exchange occurred under standard experimental conditions during sample formation, it would be useless as a probe molecule as D_2O and H_2O could no longer be considered discrete layers. However, exchange is not observed on experimental time scales below 120 K [16]. As experiments are carried out at 90–100 K, isotopic exchange can act as an indicator of film mechanisms and changes during and after ablation that encourage diffusion, collisions, etc.

D_2O and H_2O interactions are also of interest to the astrochemical community due to prevalence of water in the ISM. Furthermore, isotopic composition observed in interstellar water compared to terrestrial water has been investigated in order to understand the origin of water on Earth [17, 18]. In this work, D_2O is utilized as a probe species in ASW under astronomically relevant conditions and the implications of isotope exchange following irradiation with UV radiation are discussed.

5.2 Experimental

Refer to the experimental section in the previous chapter (Section 4.2) for a detailed description of the procedure used for data collection. A brief summary of experimental methods will be given, followed by details of changes made for this set of experiments. 266-nm radiation was used to irradiate layered ASW/ N_2O_4 films containing a third

molecular species (CO_2 , C_2H_2 , or D_2O) grown on a $\text{MgO}(100)$ substrate kept at 90 or 100 K. The previously established convention of using Langmuirs (L) for N_2O_4 thickness and monolayers (ML) for all other species will be continued in this chapter. Material leaving the film upon irradiation was collected using a pulsed TOFMS, which collected a full mass spectrum every 10 μs . A grid of nine spots were irradiated on each film, and the temporal profiles obtained from each could be averaged together to increase S/N.

5.2.1 CO_2 and C_2H_2

Films with CO_2 and C_2H_2 were grown at ~ 90 K; all other films were grown at 100 K. Background dosing was used to deposit thin layers of CO_2 or C_2H_2 (100 ML) at different depths in ASW/ N_2O_4 sandwiches, depicted in Figure 5.1.

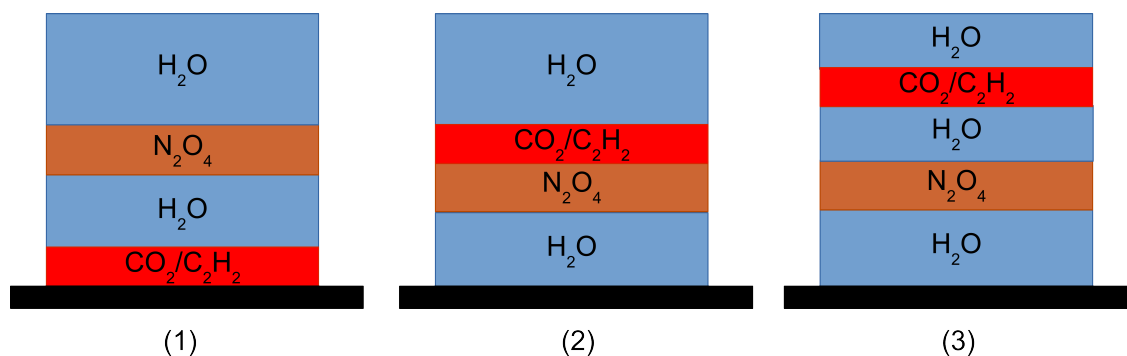


Figure 5.1: Cartoon depiction of different sandwich configurations using a third species as a probe (black represents the MgO substrate). Typical ASW sandwiches are deposited in layers, with layers of CO_2 or C_2H_2 deposited at different depths within a film. Thicknesses used were 300 ML for the bottom H_2O spacer, 80 L for the N_2O_4 layer, and 100 ML of CO_2 or C_2H_2 . The top H_2O layer was 200 ML [consisting of two separate 100 ML sections for configuration (3)].

5.2.2 D_2O

Split films of H_2O and D_2O were grown via background deposition as the top layer of ASW/ N_2O_4 sandwiches at ~ 100 K. The order of the layers was swapped per experimental needs. FTIR spectroscopy was also used to inspect H/D exchange. After an initial background spectrum was collected, layers of H_2O and D_2O were deposited

by background deposition while the substrate was in Tier 3 (refer to Section 3.1 for a diagram). Spectra were then collected after heating the film to a maximum of 160 K for 1.5 minutes.

5.3 Results

The first set of data presented are preliminary results that need more exploration in future experiments. It is important to note that CO₂ and C₂H₂ experiments were conducted before a re-calibration of the ion gauge. Also, laser energy was adjusted using an iris before installation of a telescope to collimate the beam, which may have resulted in a difference in beam diameter incident on the surface. As such, thicknesses of material are not comparable with other experiments discussed in the rest of this dissertation, and area of the surface that was irradiated was not as well regulated. However, the tight focusing of the beam ensures that area changes were likely minimal. It can be assumed that experiments conducted at the same laser energy are comparable to each other. Despite this, the data are worth discussion due to some intriguing trends. Next, isotopic data will be discussed, which is of good quality and displays interesting characteristics.

5.3.1 Depth Profiling With CO₂ and C₂H₂

Due to our lab's experience with CO₂, it was chosen as the first candidate for a probe species. We had seen previously that it was highly mobile at low temperatures and would be preferentially released from ASW if there was any significant morphological change [10]. Therefore, it was an attractive choice because any disturbance in the ASW morphology that would produce pathways to vacuum could be detected as CO₂ signal.

Films were dosed with a probe layer of CO₂ in each of the three configurations shown in Figure 5.1 and then irradiated with focused 266-nm radiation. As expected,

almost no CO_2 was liberated from the ASW underlayer when irradiating films in configuration (1). However, the second shot did show an increase in CO_2 signal (Figure 5.2). This is an intriguing result that points to structural change occurring in the bottom ASW spacer. First, it is possible that there are slight morphological changes in the ASW spacer that connect existing pores and provide a pathway for the CO_2 to escape during the second laser pulse. Second, enough energy may enter the ASW/ CO_2 spacer that the CO_2 can diffuse up through the impeding ASW (and remaining N_2O_4) on the first pulse but freezes before reaching vacuum. Upon the reintroduction of energy via a second pulse, CO_2 becomes mobile again and a fraction is able to escape the film due to its proximity to vacuum.

Comparing configuration (2) and configuration (3) provided further insight into material removal processes. More CO_2 was detected when it was dosed on top of the N_2O_4 layer than when it was sandwiched in the upper ASW layer. Furthermore, there is a noticeable difference in the shape of the CO_2^+ temporal profile when comparing configuration (2) and configuration (3) (Figure 5.3). When directly above the N_2O_4 , the CO_2^+ signal tracks the NO_x^+ signal closely, with an apparent peak in signal in the earliest extractions. In contrast, configuration (3) results in CO_2^+ signal that peaks around 100 μs , and tracks more closely with the H_2O^+ signal. These differences point to two different pathways to material removal: mixing with the hot N_2O_4 layer and “scraping” of the walls as the heated fluid escapes. When CO_2 is dosed next to the N_2O_4 it mixes with the hot fluid and comes spewing out along with it via entrainment, whereas CO_2 buried in the upper H_2O layer is only removed as hot fluid passes by the stratum and scrapes away material. The signal size difference indicates that mixing with hot N_xO_y species is a more effective means of escape from the film compared to scraping the walls of the fissures and subsequent entrainment.

This series of experiments was repeated with acetylene as the guest species. The initial goal was to test whether or not the results were CO_2 -specific. However, acetylene ended up providing another unique set of data. When acetylene was buried under the

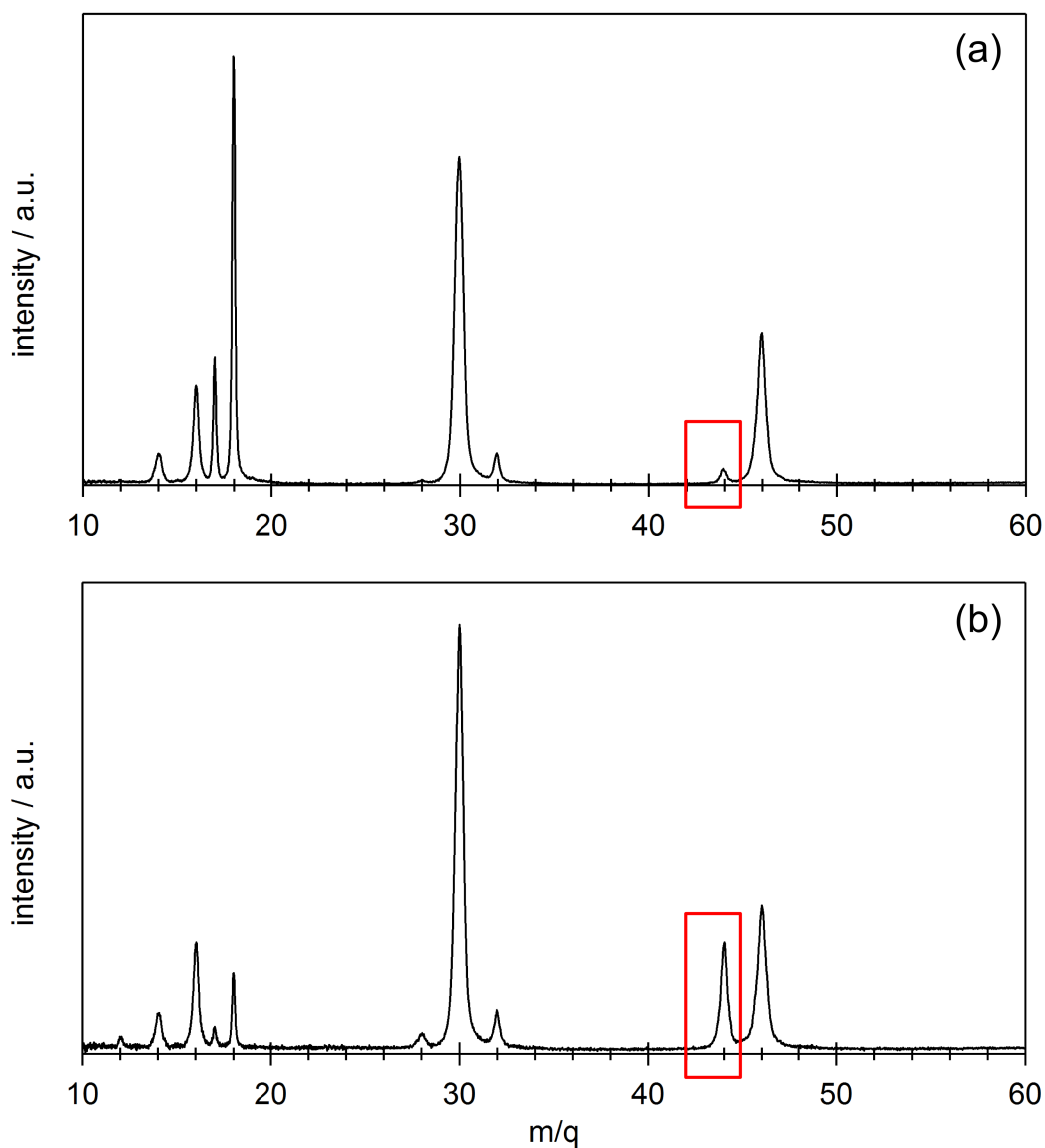


Figure 5.2: Mass spectra averaged from extractions 2-21 where CO_2 is underneath the ASW/ N_2O_4 sandwich [configuration (1) in Figure 5.1]. Mass spectrum (a) is after the first laser pulse, while (b) is from the second pulse incident on the same location (2.0 mJ); CO_2^+ peaks are boxed in red for clarity. In (a), the very small peak at mass 44 shows how little CO_2 escapes the film. This signal increases significantly after the second pulse on the same spot, indicating a morphological change that allows for CO_2 to move upward through the film.

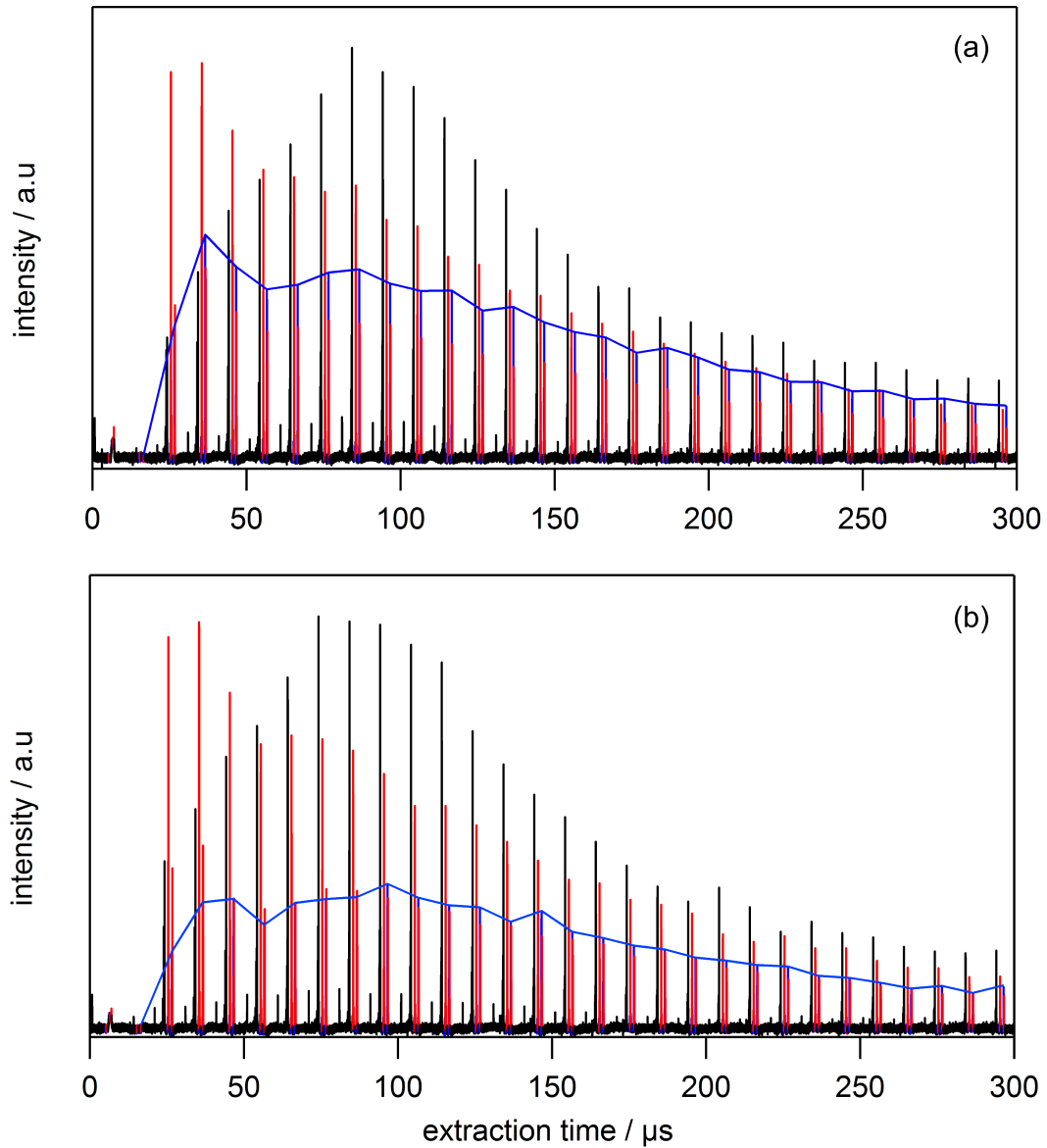


Figure 5.3: Temporal profiles comparing CO_2^+ signal in configuration (2) versus (3) (refer to Figure 5.1). Trace (a) is the result of configuration (2); trace (b) is due to ablation of configuration (3). For both temporal profiles, data was averaged for the first incident shot on 9 spots on the film (2.0 mJ). Signal due to H_2O , N_xO_y and CO_2 are designated by black, red, and blue, respectively. Because CO_2^+ is partially obscured by NO_x^+ signal, a trace of its outline is drawn in blue for clarity. (a) When CO_2 is deposited directly on top of N_2O_4 , its temporal profile tracks with the NO_x^+ signal. (b) Embedding CO_2 in the upper water layer results in a smaller signal when compared to (a), as well as slower CO_2^+ signal that tracks more closely with the water. Taken together, the traces indicate that material removal occurs via two different pathways: mixing with the hot fluid and scraping of fissure walls.

ASW spacer, we obtained data similar to that of CO_2 ; *i.e.*, no C_2H_2 escapes after the first laser pulse (though signal was not detected in subsequent pulses, either). However, the data differed significantly when the acetylene spacer was dosed on top of the N_2O_4 layer. Whereas this configuration resulted in the largest signal of CO_2^+ , there was very little C_2H_2^+ present in the mass spectrum. This was true even with multiple laser pulses incident on the same spot. Finally, the largest C_2H_2^+ signal was detected when it was sandwiched in the top ASW layer. It is worth noting that the shape of the C_2H_2 temporal profile resembles that of CO_2 when it is in the same configuration, strengthening the supposition of material removal from fissure walls.

We tried to address this strange, yet reproducible, result of C_2H_2 “disappearing” in configuration (2) by reducing the ASW spacer between the acetylene and the N_2O_4 layer to see if there was a signal trend. It was found that C_2H_2^+ signal is present even when there is only 20 ML of ASW between it and the N_2O_4 layer, but is significantly reduced or disappears altogether with no spacer (Figure 5.4). There are a few possible explanations for this observation. The obvious explanation is that the acetylene doesn’t stick to the N_2O_4 layer; however, this seems unlikely under experimental conditions. Another possibility is that acetylene is reacting with the sea of hot N_2O_4 ions and fragments that form when the film is irradiated. This explanation is made more attractive by the observation that C_2H_2 signal is not detected after two or more laser pulses on one spot when in configuration (1), which could point to C_2H_2 being consumed in the N_2O_4 layer. Despite this, no possible product fragments (e.g. $\text{C}_2\text{H}_2\text{O}^+$) were detected in any experiments with C_2H_2 . As such, this observation requires further study for elucidation.

5.3.2 Switching to D_2O

Because of the conflicting results from CO_2 and C_2H_2 , D_2O was chosen as the new test species. Deuterated water is a good probe since it behaves similarly to H_2O , and isotope exchange is extremely slow at cryogenic temperatures [15]. As our films were

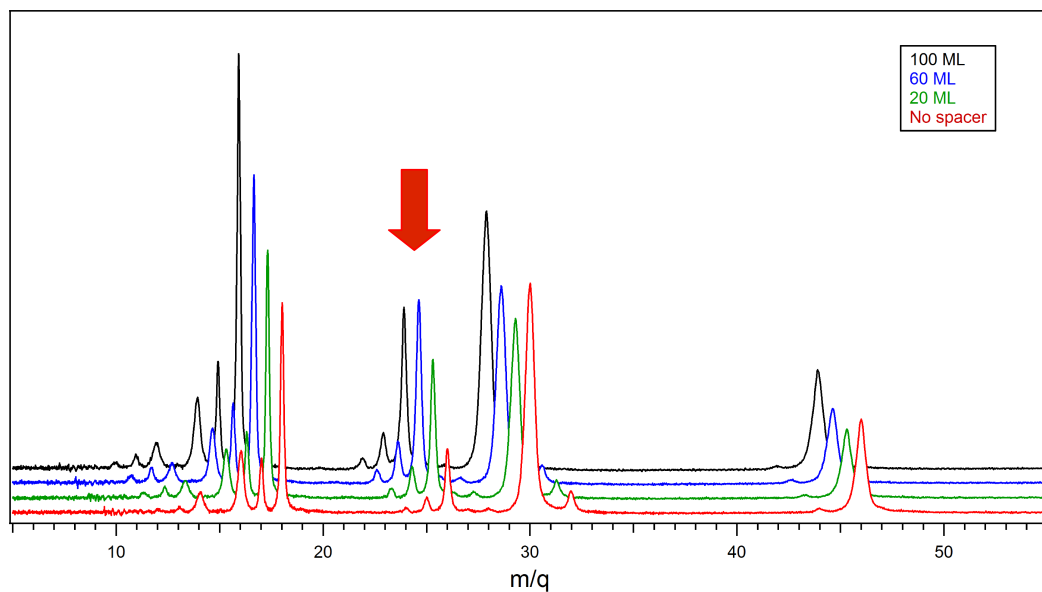


Figure 5.4: Waterfall plot of averaged mass spectra (8-9 spots, 20 extractions) from experiments using C_2H_2 in configuration (3) where the water spacer between C_2H_2 and N_2O_4 ranged from 100 to 0 ML. The main fragments detected from C_2H_2 are $C_2H_2^+$, C_2H^+ , and C_2^+ (indicated by the red arrow). Change in C_2H_2 fragment signal is small as the H_2O spacer between N_2O_4 and C_2H_2 is decreased. However, the complete removal of a water spacer results in a significant C_2H_2 signal drop.

grown and kept at 100 K, H/D exchange does not occur without an external trigger. This was verified under our experimental conditions via FTIR monitoring of a layered binary ice of H₂O and D₂O. Isotope exchange results in the sharpening of central features in both the O–D and O–H stretch peaks at 2400 and 3300 cm⁻¹, respectively [15, 19]. Within the time frame of a typical irradiation experiment (10-20 minutes), no exchange was detected. Even heating the film above the crystallization temperature of 140 K didn't result in measurable isotope exchange unless heating was maintained for over a minute (Figure 5.5). This showed that if any HDO⁺ was detected in TOFMS experiments, it must occur during the irradiation process.

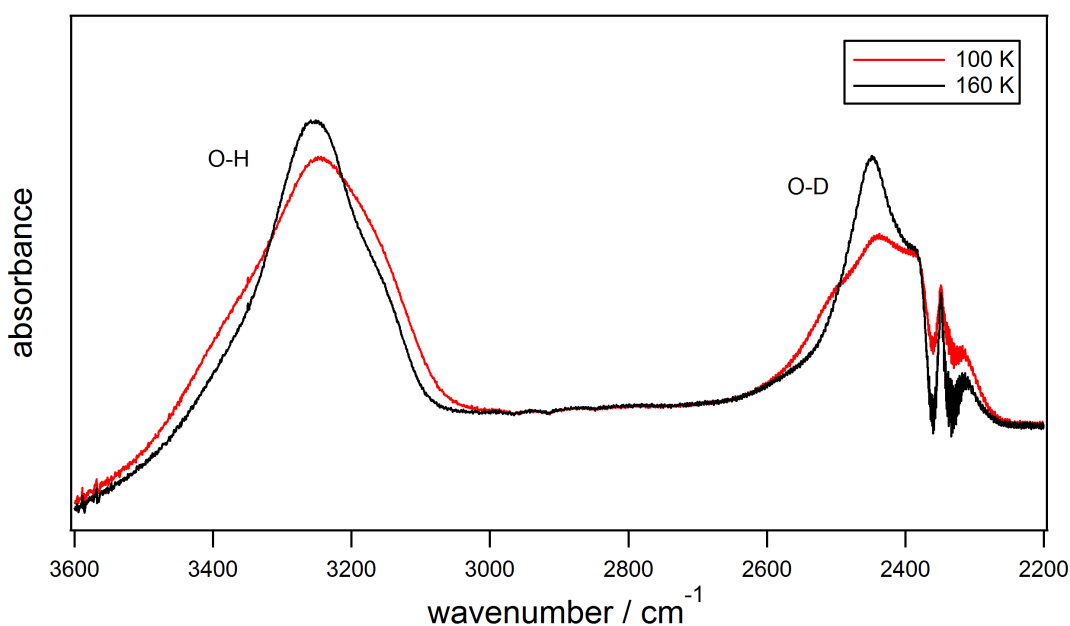


Figure 5.5: Overlaid FTIR spectra of a film initially grown at 100 K of 300 ML of H₂O deposited on 300 ML of D₂O (red) that was then heated to 160 K for 1.5 minutes (black). The appearance of a central structure in both peaks is indicative of HDO exchange occurring; there may be some contribution from crystallization of the film, but the impact should be small due to heating the film for <2 minutes. This shape change was not detected at lower temperatures or when the sample was left to sit for 20 minutes at 100 K. The negative-peak distortion of the O–D peak is due to background age.

Deuterated water was grown along with H₂O in layered configurations as depicted in Figure 5.6. When irradiated, HDO⁺ was detected as a significant product, indicating

isotope exchange was occurring. The size of HDO^+ signal in Figure 5.6 implies that extensive mixing is occurring as hot N_xO_y species are traveling through fissures. It is important to note that assuming that material is removed as hot fluid scrapes the fissure walls, H/D exchange can only happen in the upper half of the sandwich. Allowing for such a short area for exchange to occur (approximately 140 nm for the spectra shown in Figure 5.6) emphasizes the energetic nature of material removal and efficiency of mixing during irradiation. It also discourages a model involving the release of large clusters, as that would prohibit efficient isotope exchange. Another interesting feature of Figure 5.6 is how similar the HDO^+ signal is for both spectra despite the different film configurations. This points to a process where material is removed along the entire length of the fissure instead of a fraction of the fissure. Furthermore, it is evidence against significant evaporation from the surface of the film as a mechanism, as there is no appreciable change in signal when D_2O is on top or underneath H_2O .

Every mass spectrum detected from this set of experiments, with upper layer thickness ranging from 200-1200 ML, showed some amount of isotope exchange. Also, the placement of the D_2O probe layer did not have a significant impact on the amount of isotopic mixing observed, *i.e.*, having D_2O above or below the H_2O layer did not change the amount of HDO present. However, the amount of isotope exchange was dependent on the thickness of the upper $\text{H}_2\text{O}/\text{D}_2\text{O}$ layer. Because quantitative analysis of isotopically mixed species is complicated by the impossibility of collecting a pure HDO spectrum, a ratio of detected ions was used. The ratio chosen was $\text{HDO}^+/\text{D}_2\text{O}^+$ (values based on peak areas), as mass 19 and 20 can only originate from these species. It should be noted that mass 19 can also be assigned to the protonated water monomer, H_3O^+ , but this species was not detected in any experiments with segregated N_2O_4 layers. Therefore, it was assumed to have a negligible contribution to mass 19 signal. This ratio was designated R_I and used as an indicator of the percentage of mixing that occurred during irradiation of the film. Figure 5.7 is a plot of R_I vs. the thickness of $\text{D}_2\text{O}/\text{H}_2\text{O}$ layer thickness. There is a clear decrease in R_I as the thickness of D_2O and

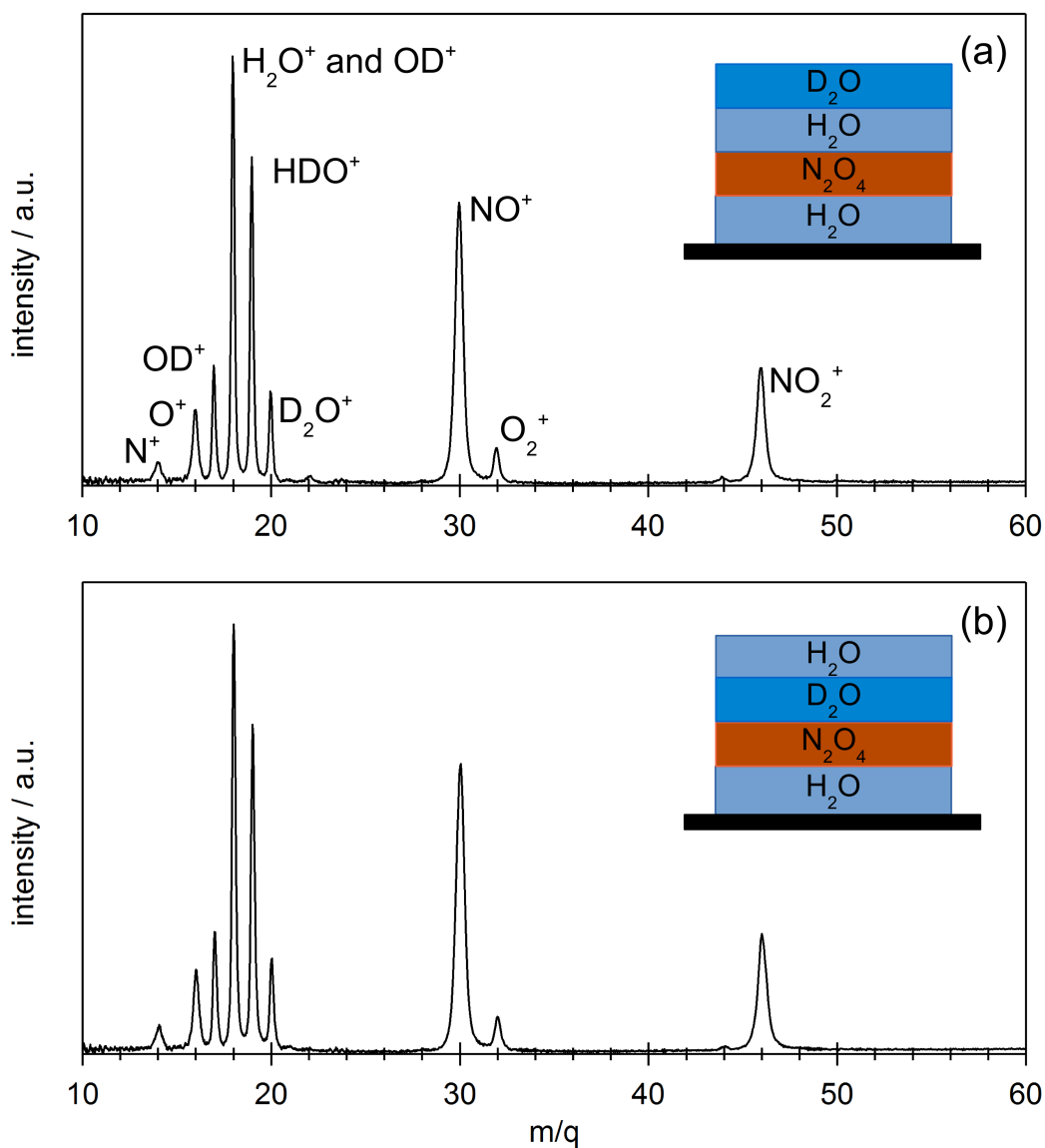


Figure 5.6: Representative mass spectra showing HDO^+ formed from isotopic scrambling during the ablation process. The spectra are averaged from the first 20 extractions yielding signal from first laser pulse temporal profiles (1.5 mJ). Mass peaks are labeled in (a) for clarity. The film layer thicknesses for both samples (a) and (b) are: 300 ML H_2O , 80 L N_2O_4 , and 200 ML each of H_2O and D_2O (configurations depicted in cartoons).

H₂O as increased. This trend points to less efficient mixing of species as the upper layer increases in thickness.

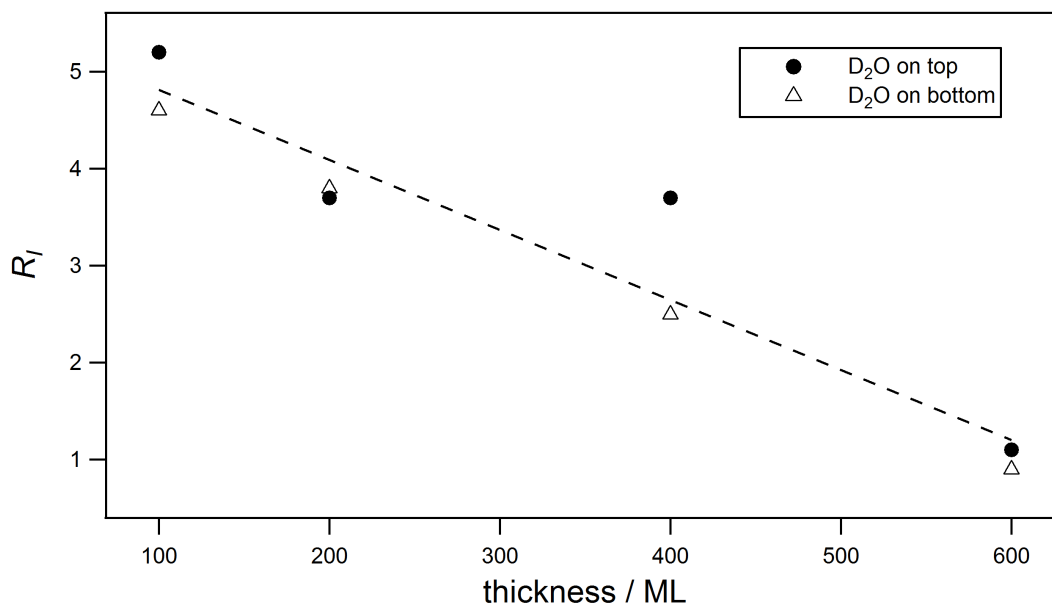


Figure 5.7: Plot showing the inverse between R_I and film thickness. R_I values were calculated for sandwich configurations like that depicted in Figure 5.6, comparing D₂O on top of a layer of H₂O or underneath a layer of H₂O. The thicknesses reported on the x -axis refer to the thickness of the individual D₂O and H₂O layers (*i.e.*, the top layer of the sandwich is twice as thick). There is a clear decrease in R_I as the thickness of the H₂O and D₂O layers increases.

5.4 Discussion

Three different molecules were used as probes to better understand the effect of extreme heating of a buried stratum in amorphous solid water. The significance of the results will be discussed in the order in which they were presented, and then a summary of implications for the proposed model will be given.

Carbon dioxide and acetylene proved to be important for gaining insight into heat transfer in ASW, despite some differences in behavior. As previously established, when

buried N_2O_4 is heated with UV radiation, it becomes an extremely hot fluid that fractures the ASW layer to form fissures through which material can escape. Material immediately surrounding the N_2O_4 layer will become heated and mixed with the hot fluid produced, but the extent of this mixing is inherently limited due to poor thermal conductivity within the film. This is deduced from the different behavior of CO_2 when placed at different depths within the film. Carbon dioxide that is in direct thermal contact with the hot N_2O_4 layer is able to escape along with the hot fluid through fissures with relative ease compared to CO_2 embedded in the upper ASW layer, as is apparent from the change in overall signal and temporal profile shape. This contrasts with the “top-down” process described by May and coworkers [4], where material closer to the surface is preferentially released as cracks propagate downward from the vacuum interface. It may be expected that even though the “bottom-up” mechanism of N_xO_y expulsion from fissures is robust, the mobility of CO_2 would mitigate the effect on signal size (*i.e.* depth would play a more dominant role). However, CO_2 escapes more efficiently with the hot N_xO_y despite the increased distance of travel to vacuum. This reinforces how energetic a process is occurring during irradiation with 266-nm laser pulses.

Introducing D_2O as a probe species gave additional insight to the molecular transport model. However, data interpretation was complicated by the fact that it is difficult to deconvolute the populations of each isotopic parent species as the cracking pattern of pure HDO is impossible to obtain due to the statistical populations of 1:1:2 that exist when equal parts H_2O and D_2O are mixed. Despite this, some qualitative statements can be made about these data.

It was found by analysis of FTIR spectra taken over experimental time scales that isotope exchange does not occur within our samples at 100 K. Therefore, it can only occur either in the film during the laser heating and subsequent release of N_2O_4 or directly above the film surface. Laser heating of the film itself is insufficient to induce exchange on a significant scale. Experiments carried out by Park and coworkers [20]

investigated the rate of isotope exchange in thin binary films exposed to HCl at 95 and 140 K. Even with the benefit of the HCl catalyst and a low activation energy (9.8 kJ/mol), exchange was only observed at 140 K and the process continued for at least 10 minutes without reaching complete exchange. Based on calculations conducted in our lab [21], thin upper ASW films (300 ML) can reach a surface temperature of 195 K and internal temperatures above that, but cool back to 100 K within 150 ns. Thicker films (>600 ML) heat and cool more slowly, but reach a lower maximum temperature of <120 K. Neither of these cases engenders H/D exchange from laser heating, so other explanations are needed for this observation.

It is plausible that some exchange occurs due to gas-phase collisions as the hot mix of chemicals leaves the film. Past and current data show that collisions are a feature of our system due to the density of fissures at the ASW/vacuum interface and the fluid that escapes from the fissures. Experimentally, it is detected as an unphysically long “tail” in temporal profile data that can extend for over 1 ms. However, the orientation and energy for these collisions to result in isotope exchange would likely make this path a small contributor to the overall population of HDO.

Isotope exchange can also occur as hot N_2O_4 carves out channels in the ASW film, scraping the walls and encouraging mixing of H_2O and D_2O . This is a likely scenario that is further supported by the similarity of exchange signal independent of D_2O arrangement. It also indicates that water molecules are removed from the fissure walls along the entire path length.

The large fraction of HDO^+ detected in relation to the D_2O peak (see Figures 5.6 and 5.7) reveals that mixing is extremely high and indicates a very dense plume of material. Furthermore, it reinforces the proposal that large chunks of material are *not* being released in this mechanism, as that would prohibit extensive isotope exchange. Interestingly, the mixing ratio decreases with increasing film thickness. Such a trend may point to wider fissures that provide fewer opportunities for isotope exchange, but

to be more definitive on this subject would be speculative. Further study is needed to understand this trend as it relates to the heating of a buried stratum model.

5.5 Conclusions

This chapter has presented data that builds on the “fissure” model detailed in Chapter 4. The extreme heating of a buried stratum was analyzed by introducing a probe species (CO_2 , C_2H_2 , or D_2O) at different levels within a typical “sandwich” configuration. Focused 266-nm radiation was used to irradiate the film, and the behavior of the probe species was tracked relative to N_xO_y and H_2O fragments. Carbon dioxide and acetylene gave valuable insight into the effective quenching of the film by MgO acting as a heat sink. Furthermore, CO_2 behaved differently when placed above the N_2O_4 layer compared to being embedded in the upper ASW layer. This implied that there were two driving forces behind material removal. Molecules in direct contact with the hot N_2O_4 fluid become entrained and escape from the ASW film with similar speeds. Material in upper layers is removed as the hot fluid scrapes the walls. Introducing D_2O provided further insight into transport and molecular interactions within the film. The presence of H/D exchange products supported scraping of fissure walls along the entire path to vacuum.

Continued study of these systems using FTIR spectroscopy will be beneficial for quantitatively measuring shot-by-shot material removal. In particular, the absorption bands of CO_2 centered at 2350 and 3800 cm^{-1} are easily detected and their decay can be measured against that of ASW at 3400 cm^{-1} . Also, further experimentation is required to explore the result of acetylene’s possible reaction during irradiation. By varying placement and thickness of C_2H_2 layers within ASW films, we may be able to determine the nature of its interaction with its environment and determine details of any reactions that may take place. Understanding what chemistry can occur during the expulsion of material from the film may have implications for Enceladus, with its jets of molecularly-rich water plumes. Knowing what species can survive a trip from a buried ocean

through a thick crust of ASW can give insight into the material that is detected in these “volcanoes.”

Chapter References

- [1] Loerting, T.; Winkel, K.; Seidl, M.; Bauer, M.; Mitterdorfer, C.; Handle, P.; Salzmann, C.; Mayer, E.; Finney, J.; Bowron, D. *Phys. Chem. Chem. Phys.* **2011**, *13*, 8737–8794.
- [2] Hama, T.; Watanabe, N. *Chem. Rev.* **2013**, *113*, 8783–8839.
- [3] Manca, C.; Martin, C.; Roubin, P. *J. Phys. Chem. B* **2003**, *107*, 8929–8934.
- [4] May, R.; Smith, R.; Kay, B. *J. Chem. Phys.* **2013**, *138*, 104501.
- [5] May, R.; Smith, R.; Kay, B. *J. Chem. Phys.* **2013**, *138*, 104502.
- [6] Laufer, D.; Bar-Nun, A.; Igal, P.; Jacovi, R. *Icarus* **2013**, *222*, 73–80.
- [7] Herbst, E. *AIP Con. Proceed.* **2013**, *1543*, 15–30.
- [8] Kumi, G.; Malyk, S.; Hawkins, S.; Reisler, H.; Wittig, C. *J. Phys. Chem. A* **2006**, *110*, 2097–2105.
- [9] Malyk, S.; Kumi, G.; Reisler, H.; Wittig, C. *J. Phys. Chem. A* **2007**, *111*, 13365–13370.
- [10] Rebolledo-Mayoral, O.; Stomberg, J.; McKean, S.; Reisler, H.; Wittig, C. *J. Phys. Chem. C* **2012**, *116*, 563–569.
- [11] De Grotthuss, C. *Ann. Chim.* **1806**, *58*, 54–73.
- [12] Collier, W.; Ritzhaupt, G.; Devlin, J. *J. Phys. Chem.* **1984**, *88*, 363–368.
- [13] Lee, C.; Lee, P.; Kim, Y.; Kang, H. *J. Chem. Phys.* **2007**, *127*, 084701.
- [14] Kim, J.; Kim, Y.; Kang, H. *J. Chem. Phys.* **2009**, *131*, 0044705.
- [15] Blomquist, J.; Andersson, M.; Uvdal, P. *Phys. Rev. Lett.* **2011**, *107*, 216101.
- [16] Gálvez, Ó.; Maté, B.; Herrero, V.; Escribano, R. *Astrophys. J.* **2011**, *738*, 133–138.
- [17] Robert, F. *Science* **2001**, *293*, 1056–1058.
- [18] Sarafian, A.; Nielsen, S.; Marschall, H.; McCubbin, F.; Monteleone, B. *Science* **2014**, *31*, 623–626.
- [19] Cwiklik, L.; Devlin, J.; Buch, V. *J. Phys. Chem. A* **2009**, *113*, 7482–7490.
- [20] Park, S.; Jung, K.; Kang, H. *J. Chem. Phys.* **2004**, *121*, 2765–2774.

- [21] McKean, S. M. Energy Transfer in Amorphous Solid Water: Light-Mediated Expulsion of N_2O_4 Guest Molecules., Ph.D. Thesis, University of Southern California, 2015.

Future Work

This dissertation has dealt mainly with the development of a qualitative model that explains how a hot fluid (N_2O_4 and derivative species) forces its way through an ASW film. Due to the many variables and unknowns in the experimental approach and proposed mechanism, currently it is not possible to be quantitative about the changes that occur in the ASW, not to mention its morphology after irradiation. Some of these issues can be addressed by making adjustments to equipment in the laboratory. A change in experimental strategy is required as well to address other questions that remain. Proposed experiments would utilize gold nanoparticles to create fissures of known length and diameter, which can then be doped with molecules of interest. This chapter discusses changes in experimental apparatus first, then discusses increased exploration of systems already investigated, and finally covers the implementation of gold nanoparticles as fissure-creators along with preliminary results.

6.1 Improvements in Experimental Apparatus

There are some practical changes that can address experimental shortcomings. The easiest to implement would be the purchase and installation of a mercury-cadmium-telluride (MCT) detector for the FTIR spectrometer. MCT detectors are sensitive over the range $600\text{-}8000\text{ cm}^{-1}$, which includes the primary absorption bands of N_2O_4 [1], and as such would improve our detection capabilities. The successful implementation

of a MCT detector may require a change in substrate material and UHV chamber windows along the FTIR beam path, as MgO and CaF₂ drop to 50% transmission around 1250 cm⁻¹ and 1050 cm⁻¹, respectively. A material that would allow access to lower energy absorption bands is BaF₂, though implementation may not be easy. BaF₂ windows are available from several vendors, but there may be some trial and error required for substrate preparation. The cleaving method used to produce clean MgO substrates may not be so facile with a softer material like BaF₂.

Another change that would expand experimental possibilities would be the installation of a helium cryostat. Two closed-cycle refrigerators are already available to the lab, but may need refurbishing. This would extend our temperature range to ≤ 20 K and would result in improved control over substrate temperature. Such a change would allow for a much larger range of molecules to condense on the surface, including non-reactive gases such as N₂, Ar, Kr, and CH₄. This opens up an experimental route to investigating fissure capacity by inert gas uptake, a method used by other groups researching ASW morphology [2, 3]. After a film with fissures is generated, a probe gas can be deposited to fill the fissures. A suitable choice would be N₂, which does not form multilayers on an ASW surface at 27 K and has been used by Bruce Kay with success [4]. Then, TPD experiments can be conducted to measure the overall signal of the probe gas (in this case, N₂) and the capacity of the fissures may be determined in a quantitative way. It may be possible to use different probe gases to determine information about the size and nature of the fissures (e.g. to look at how much dangling -OH is present, desorption temperatures of the probe gas could be examined).

A final addition to the experimental system would be the introduction of a cryogenic quartz crystal microbalance (CQCM). This would allow for exact measurements of film thickness after vapor deposition, which has proven to be difficult with our current equipment. While the low temperature limit of a CQCM is typically around 75 K (though some have been reported in the literature to be used at 30-40 K [5]), it would

still be extremely useful for calibrating films grown under standard experimental conditions.

6.2 Introducing a Third Species: What Next?

D₂O, CO₂, and C₂H₂ have already been utilized as probe molecules for understanding energy transfer in ASW films (refer to Chapter 5 for a discussion of these experiments). However, the scope of these experiments was relatively limited and did not fully explore what could be learned using these materials.

¹²CO₂ and ¹³CO₂ are attractive species for probing material removal quantitatively because of their strong absorption peaks at 2350 cm⁻¹ and 2280 cm⁻¹, respectively. If ¹²CO₂ is codeposited with N₂O₄ and the film is subsequently ablated, removal on a shot-by-shot basis can be tracked by FTIR for both species. In addition, ¹³CO₂ can be dosed as an embedded stratum in the top ASW layer. This way, a comparison can be made between material that is removed via entrainment in the hot fluid versus material that is removed from the fissure walls. Another direction to pursue would be deposition of ¹³CO₂ and ¹²CO₂ at different levels in the ASW in order to examine fissure formation. Exploring various combinations would invariably invite more ideas for experimental investigation.

6.3 Gold nanoparticles as Fissure-Creators

Gold nanoparticles are an increasingly useful scientific tool in chemistry, medicine, and materials science. Their shape and size can dictate very specific absorption spectra via inducement of surface plasmonic resonance (SPR). In conjunction with short laser pulses, this can result in very fast heating of the particles as energy absorbed gets converted to heat. Being able to tailor gold nanoparticles with respect to their size, shape, and absorption range has enabled a variety of medical applications involving selective damage, such as destroying cancer cells[6].

The ability to selectively remove material is also appealing for introducing structural features to a film, which is proposed for the future direction of this project. In other words, gold nanoparticles can be used to create fissures of a known size in an ASW film in a step-wise fashion. First, a MgO surface would be doped with gold nanoparticles. The coverage would be kept low enough that the average interparticle distance is at least an order of magnitude larger than the nanoparticle diameter to minimize side effects due to particle interaction. After installation of the surface in the vacuum chamber, a layer of N_2O_4 followed by a ASW layer would be grown over the nanoparticles. Then, the surface would be subjected to 532 nm radiation which excites the plasmon resonance of the nanoparticles [7]. The excitation quickly degrades to heat on a ps timescale [8], which rapidly heats the gold nanoparticles and material above it. Molecules above the gold nanoparticles desorb due to this heat, forming vertical channels in the ASW film (Figure 6.1). Because of the known diameters of the nanoparticles and the known thickness of the ASW film, it is possible to approximate the dimensions of these fissures. The nature of this method makes the density and diameter of fissures customizable by adjusting nanoparticle doping concentration and size. Different fissure shapes can be achieved by utilizing nanorods in place of spheres, which are easily excited with 1064 nm radiation. Thicker films can be achieved iteratively, by adding layers of ASW until nanoparticle heating no longer removes material. Then, UV radiation (355 or 266 nm) can be used to excite the N_2O_4 layer and make longer fissures.

Once channels of known dimension are formed, they can be doped with molecules of interest and further probed using LID, FTIR, and TPD techniques. This “bottom-up” method of creating fissures differs greatly from the standard procedures for introducing morphological changes in ASW, which include extreme pressure (GPa) and thermal and radiative heating [9]. Instead of triggering morphological changes throughout the entire film that are difficult to quantify, a size and shape limit is put in place. Furthermore, the distribution density of fissures can be easily adjusted by changing the density

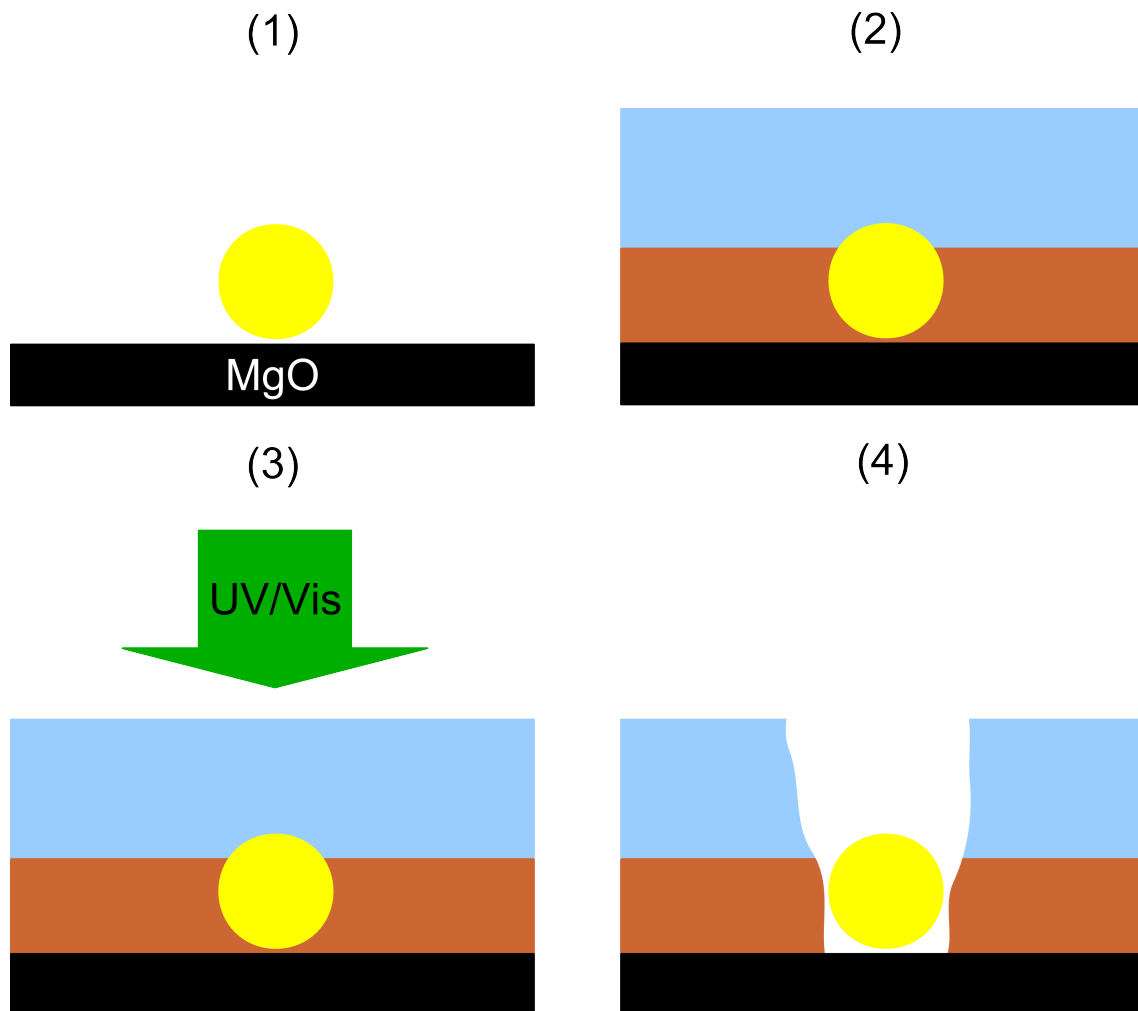


Figure 6.1: Cartoon depiction of how gold nanoparticles can be used to form channels in ASW using 532 nm radiation, which is resonant with 10-80 nm gold nanoparticles. (1) Nanoparticles are deposited on a bare MgO surface, and particle density is determined using AFM. (2) A layer of N_2O_4 , followed by ASW is grown over the nanoparticles. (3) 532 nm radiation is focused on the surface, heating the nanoparticles via surface plasmon resonance to remove material. Once SPR heating is no longer able to remove material, UV radiation (355/266 nm) is used to excite the N_2O_4 layer. (4) This iterative process can form vertical channels in the ice that are roughly the diameter of the gold nanoparticle and length of the film. Once these channels are formed, they can be doped with molecules of interest and the film can be further probed with spectroscopic techniques.

of nanoparticle distribution on the substrate. This would be the first example of experimentally grown ASW fissures with known dimensions and distribution, which could be characterized quantitatively.

6.4 Experimental Strategy

In order to test the validity of this novel technique, some preliminary experiments were carried out. One goal was to test the ease of sample preparation with our existing apparatus. Another goal was assessing the feasibility of the proposed method, *i.e.*, can gold nanoparticles remove water via 532 nm laser radiation? In order to do this, it was necessary to prepare MgO substrates with deposited gold nanoparticles and install them in our UHV chamber. Then, ASW films could be grown and irradiated with minor changes to our typical experimental set-up.

6.4.1 Surface Preparation and Experimental Adjustments

A new surface had to be prepared, as water was found to not wet aged pieces of MgO(100). Since no FTIR would be carried out in these initial tests, we only cleaved one side to make a new substrate from a block of MgO(100). The smoothness of the MgO substrate was then analysed using atomic force microscopy (AFM), and it was found to be relatively smooth with terraces as the main defect feature (refer to Figure 3.3 in Chapter 3).

Gold nanoparticles (10, 20, 40, and 80 nm; citrate-capped spheres in DI water; Nanopartz) were deposited by wetting the surface of the MgO(100) substrate with one drop of a solution whose concentration was diluted with distilled water to $4\text{--}6 \times 10^{10}$ nps/mL. Evaporation was accelerated by directing a flow of dry N₂ at the freshly-wetted surface. This deposition method resulted in a surface density of approximately 1-10 nanoparticles per square micron (Figures 6.2 and 6.4a). The surface was reinstalled in the chamber in the typical configuration (refer to Chapter 3 for a

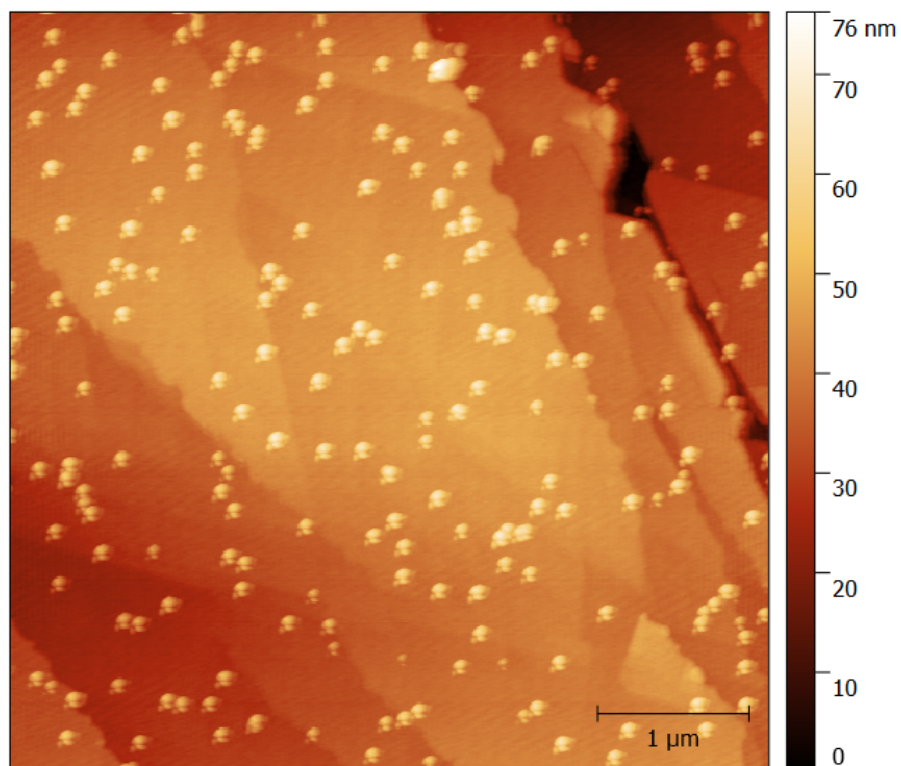


Figure 6.2: AFM image of a MgO(100) surface wetted with one drop of a solution containing 20 nm gold nanoparticles with a concentration of approximately 6×10^{10} nps/mL. This scan was taken from the center of the surface, where the density of the particles was ~ 10 nanoparticles per square micron. In scans taken near the edge of the surface, the density of nanoparticles was slightly higher and more aggregates of particles were visible.

more detailed description), but the oxygen annealing procedure was not carried out to avoid possible melting, migration, and sintering of nanoparticles on the substrate. We were able to successfully make substrates with 20 and 80 nm nanoparticles, but had deposition issues with 10 and 40 nm nanoparticles. The 10 nm nanoparticles appeared to be too mobile for the wetting deposition method, and as such aggregated in the area that evaporated last instead of sticking to the surface where initially deposited. While trying to make a surface with 40 nm nanoparticles, we ran into repeated issues of contamination and were forced to abandon the attempt.

6.5 Initial Results

We were able to test the efficacy of the proposed method by using 532 nm radiation to irradiate the surface, which was easily generated as the second harmonic of our existing Nd:YAG laser (refer to Figure 3.6 in Chapter 3 for a schematic of the laser set-up). The simplest system, consisting of ASW grown over gold nanoparticles, showed modest signal with one laser pulse (Figure 6.3). This verified that SPR heating of gold nanoparticles is capable of selectively removing ASW from a film under typical experimental conditions.

Mixed in with the water fragments were CO^+ and CO_2^+ , which were evidence of the citrate ligands breaking apart and flying off of the gold nanoparticles. The appearance of the citrate fragments was decreased by increasing the thickness of the ASW film. This may be due to citrate fragments becoming “caught” in longer channels or the dispersion of heat through a thicker film limiting their fracture and movement.

We attempted to find the film thickness cut-off for ASW removal using 20 nm gold nanoparticles by testing films of thicknesses ranging from 300-1200 ML. We were able to consistently get signal with a 300 ML-thick film, which is roughly equivalent to 100 nm of material on the nanoparticles. Six hundred monolayers of ASW also resulted in signal, but no signal was detected with 1200 ML (480 nm). These results couldn't be

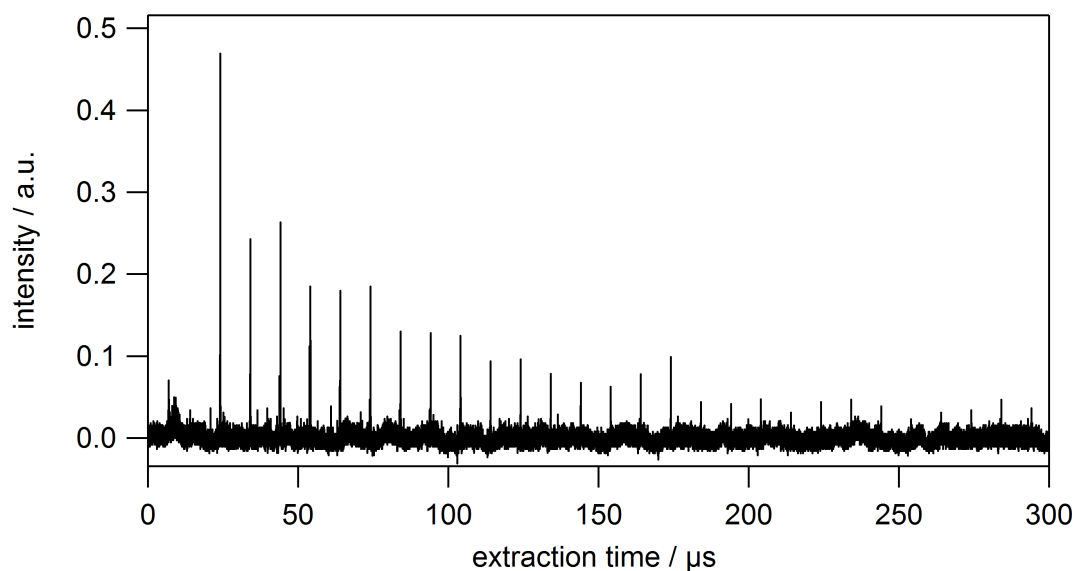


Figure 6.3: A temporal profile of 300 ML of ASW grown over 20 nm gold nanoparticles after irradiation with 6.4 mJ of focused 532 nm light (average of three spots). The majority of the signal is due to water and water fragments, with some contribution from citrate fragments.

repeated rigorously as we had an issue with nanoparticle degradation, discussed in the following section.

Another interesting finding came from introducing a N_2O_4 layer. Irradiating a film with ASW underneath a layer of N_2O_4 resulted in less desorbing material than when N_2O_4 was underneath an ASW layer. Understanding this preliminary finding requires further study and speculation will not be engaged in at this time.

6.5.1 Nanoparticle Breakdown

While we were able to get measureable desorption signal, which increased with nanoparticle size and film thickness (to a cutoff point), the nanoparticles seemed to have an irradiation lifetime. The alignment of our laser, combined with the precision movement of the surface in the x and z direction, resulted in repeated irradiation of specific spots on the surface. After conducting an experiment on a designated location

on the surface, returning to that location with a new film would have either smaller signal or no signal at all. Adjusting the position slightly to a spot that had not been irradiated in previous experiments gave strong signal. This indicated that distortion of the particles was occurring such that they were no longer absorbing at 532 nm. This was confirmed by several AFM images that appear to show conglomerated (20 nm) or obliterated particles (80 nm) in irradiated areas. Before and after images of 80 nm particles are shown in Figure 6.4. In the case of the 80 nm particles, the dramatic “exploded” appearance coincides with the findings of other groups working with nanoparticles in the liquid phase [6, 10, 11].

6.6 Summary and Future Experiments

Based on preliminary results, it is possible to form channels of known diameter in ASW using gold nanoparticles with 532 nm radiation. The method we used had issues, and would benefit from the following refinements:

- fine-tuning of the nanoparticle deposition process to accommodate more sizes and even distribution
- careful study of laser fluence to determine a balance between signal and nanoparticle degradation
- use of gold nanoparticles capped with a more robust material, such as silica
- characterization of film thicknesses to obtain the optimum nanoparticle size/ASW film thickness combination
- testing of gold nanorods to create wider fissures via irradiation with 1064 nm light

Once surfaces can be easily installed and used repeatedly to create films, more complex experiments can be carried out. For example, after fissures have been created in an ASW film, they can be doped with a radiation-absorbing molecule. This film can then

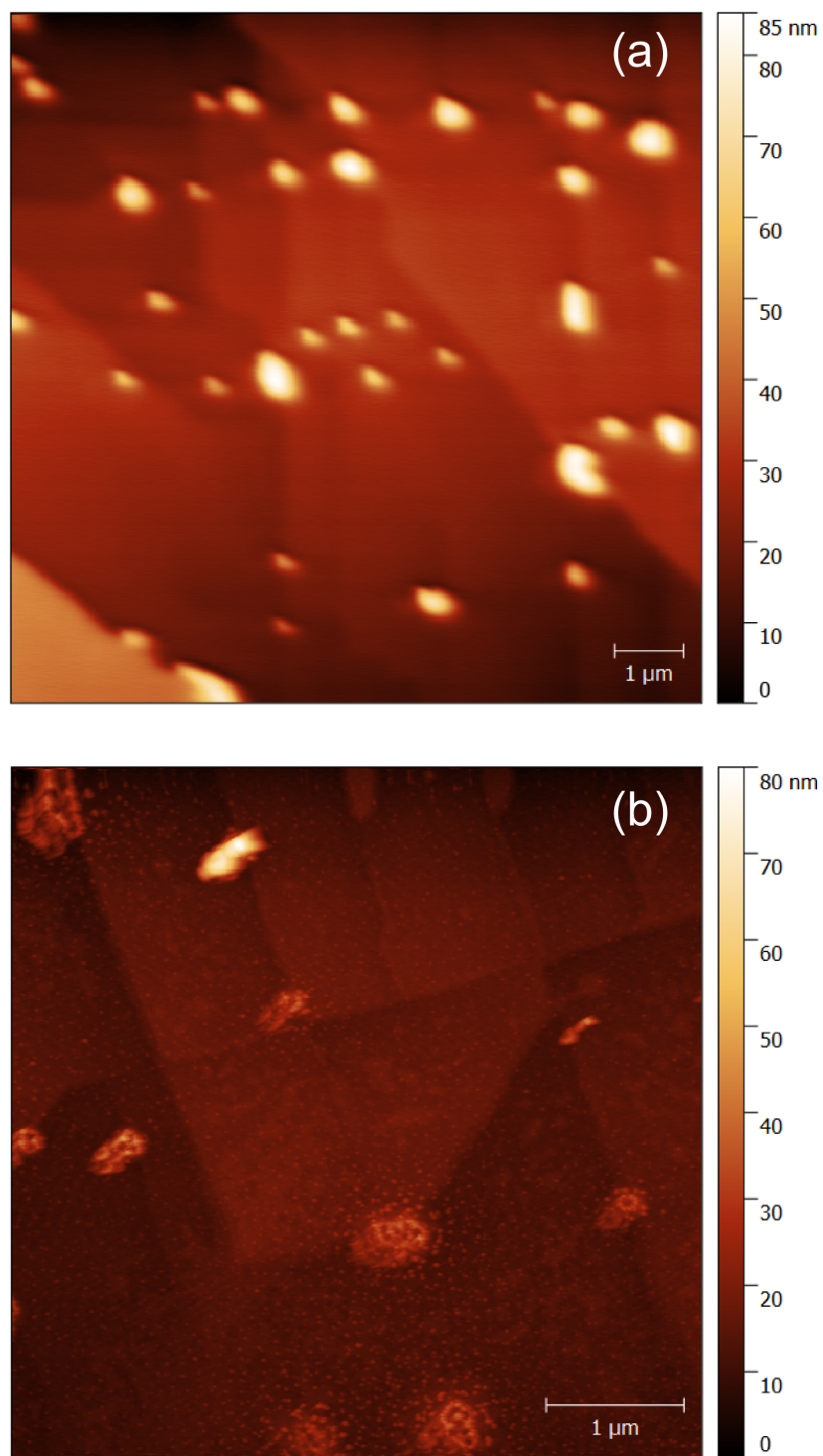


Figure 6.4: AFM images of 80 nm gold nanoparticles on the MgO substrate before (a) and after (b) laser ablation. The particle density of the freshly-prepared film was approximately 1 particle per micron. The particles in (b) have experienced several 532 nm pulses at a fluence of up to $\sim 3 \text{ J/cm}^2$.

be irradiated and energy transfer to ASW could be analyzed. Also, the fissure model proposed in Chapter 4 could be explored further by varying the distribution density of nanoparticles on the surface. By lowering the density of the nanoparticles, and thus fissures, the structure of temporal profiles from resulting films could be examined and contrasted with the data presented in this dissertation (which is posited to be the result of a high fissure density system). The complicated nature of ASW as a system invites further study, and the ideas presented in this chapter can improve characterization and understanding.

Chapter References

- [1] Mélen, F.; Pokorni, F.; Herman, M. *Chem. Phys. Lett.* **1992**, *194*, 181–186.
- [2] Bar-Nun, A.; Dror, J.; Kochavi, E.; Laufer, D. *Phys. Rev. B* **1987**, *35*, 2427–2435.
- [3] Bar-Nun, A.; Kleinfeld, I.; Kochavi, E. *Phys. Rev. B* **1988**, *38*, 7749–7754.
- [4] Smith, R.; Zubkov, T.; Dohnálek, Z.; Kay, B. *J. Phys. Chem. B* **2009**, *113*, 4000–4007.
- [5] Raut, U.; Famá, M.; Teolis, B.; Baragiola, R. *J. Chem. Phys.* **2007**, *127*, 204713.
- [6] Letfullin, R.; Joenathan, C.; George, T.; Zharov, V. *Nanomedicine* **2006**, *1*, 473–480.
- [7] Fox, M., *Optical Properties of Solids*; Oxford University Press: 2010.
- [8] Nedyalkov, N.; Imamova, S.; Atanasov, P.; Toshkova, R.; Gardeva, E.; Yossifova, L.; Alexandrov, M.; Obara, M. *Appl. Surf. Sci.* **2011**, *257*, 5456–5459.
- [9] Angell, C. *Annu. Rev. Phys. Chem.* **2004**, *55*, 559–583.
- [10] Cavicchi, R. E.; Meier, D.; Presser, C.; Prabhu, V.; Guha, S. *J. Phys. Chem. C* **2013**, *117*, 10866–10875.
- [11] Werner, D.; Hashimoto, S. *J. Phys. Chem. C* **2011**, *115*, 5063–5072.

BIBLIOGRAPHY

- Andersson, O.; Inaba, A. *Phys. Chem. Chem. Phys.* **2005**, *7*, 1441–1449.
- Andrews, B.; Anderson, A. J. *Chem. Phys.* **1981**, *74*, 1534–1537.
- Angell, C. *Annu. Rev. Phys. Chem.* **2004**, *55*, 559–583.
- Angell, C. *Science* **2008**, *319*, 582–587.
- Ayotte, P.; Smith, R.; Stevenson, K.; Dohnálek, Z.; Kimmel, G.; Kay, B. J. *Geophys. Res.* **2001**, *106*, 33387–33392.
- Bach, W.; Breuer, H. *Faraday Discuss. Chem. S.* **1974**, *58*, 237–243.
- Backus, E.; Grecea, M.; Kleyn, A.; Bonn, M. *Phys. Rev. Lett.* **2004**, *92*, 236101.
- Bai, Y.; Ogai, A.; Qian, C.; Iwata, L.; Segal, G.; Reisler, H. *J. Chem. Phys.* **1989**, *90*, 3903–3914.
- Gandyopadhyay, D.; Mohan, S.; Ghosh, S.; Choudhury, N. *J. Phys. Chem. B* **2013**, *117*, 8831–8843.
- Baragiola, R. *Planet. Space Sci.* **2003**, *51*, 953–961.
- Bar-Nun, A.; Dror, J.; Kochavi, E.; Laufer, D. *Phys. Rev. B* **1987**, *35*, 2427–2435.
- Bar-Nun, A.; Kleinfeld, I.; Kochavi, E. *Phys. Rev. B* **1988**, *38*, 7749–7754.
- Bass A.M. and Ledford Jr., A.; Laufer, A. *J. Res. Nat. Bur. Stand. A* **1976**, *80A*, 143–166.
- Beavis, R.; Chait, B. *Chem. Phys. Lett.* **1991**, *181*, 479–484.
- Bernal, J.; Fowler, R. *J. Chem. Phys.* **1933**, *1*, 515–548.
- Blomquist, J.; Andersson, M.; Uvdal, P. *Phys. Rev. Lett.* **2011**, *107*, 216101.
- Bolduan, F.; Jodl, H.; Loewenschuss, A. *J. Res. Nat. Bur. Stand. A* **1976**, *80A*, 143–166.
- Brown, D.; George, S.; Huang, C.; Wong, E.; Rider, K.; Smith, R.; Kay, B. J. *Phys. Chem.* **1996**, *100*, 4988–4995.

Brovchenko, I.; Oleinikova, A. *J. Chem. Phys.* **2006**, *124*, 164505.

Brüggeller, P.; Mayer, E. *Nature* **1980**, *288*, 569–571.

Burgess, D.; Stair, P.; Weitz, E. *J. Vac. Sci. Technol., A* **1986**, *4*, 1362–1366.

Burke, D.; Brown, W. *Phys. Chem. Chem. Phys.* **2010**, *12*, 5947–5969.

Burton, E.; Oliver, W. *Nature* **1935**, *135*, 505–506.

Cavicchi, R. E.; Meier, D.; Presser, C.; Prabhu, V.; Guha, S. *J. Phys. Chem. C* **2013**, *117*, 10866–10875.

Chiu, W. *Ann. Rev. Biophys. Biophys. Chem.* **1986**, *15*, 237–257.

Cholette, F.; Zubkov, T.; Smith, R.; Dohnálek, Z.; Kay, B.; Ayotte, P. *J. Phys. Chem. B* **2009**, *113*, 4131–4140.

Chrysanthou, A.; Grieveson, P. *Mat. Sci. Eng. A* **1995**, *194*, L11–L14.

Chuang, T. *Surf. Sci. Rep.* **1983**, *3*, 1–105.

Chyba, C.; Sagan, C. *Nature* **1992**, *355*, 125–132.

Collier, W.; Ritzhaupt, G.; Devlin, J. *J. Phys. Chem.* **1984**, *88*, 363–368.

Time-of-Flight Mass Spectrometry; Cotter, R. J., Ed.; American Chemical Society: 1994.

Cwiklik, L.; Devlin, J.; Buch, V. *J. Phys. Chem. A* **2009**, *113*, 7482–7490.

Debenedetti, P. *J. Phys.: Condens. Matter* **2003**, *15*, R1669–R1726.

Devlin, J. *J. Geophys. Res.* **2001**, *106*, 33333–33349.

Dixon-Warren, S. J.; Jackson, R.; Polanyi, J.; Rieley, H.; Shapter, J.; Weiss, H. *J. Phys. Chem.* **1992**, *96*, 10983–10994.

Dohnálek, Z.; Ciolli, R.; Kimmel, G.; Stevenson, K.; Smith, R.; Kay, B. *J. Chem. Phys.* **1999**, *110*, 5489–5492.

Dohnálek, Z.; Kimmel, G.; Ayotte, P.; Smith, R.; Kay, B. *J. Chem. Phys.* **2003**, *118*, 364–372.

Draine, B. *Annu. Rev. Astron. Astrophys.* **2003**, *41*, 241–289.

Ediger, M.; Angell, C.; Nagel, S. *J. Phys. Chem.* **1996**, *100*, 13200–13212.

Edwards, G. *Laser Photonics Rev.* **2009**, *3*, 545–555.

English, N.; Tse, J.; Gallagher, R. *Phys. Rev. B* **2010**, *83*, 092201.

- English, N.; Tse, J. *Phys. Rev. B* **2011**, *83*, 184114.
- Essmann, U.; Geiger, A. *J. Chem. Phys.* **1995**, *103*, 4678–4692.
- Faizullin, M.; Vinogradov, A.; Koverda, V. *Chem. Eng. Sci.* **2015**, 000–000.
- Fanetti, S.; Pagliai, M.; Citroni, M.; Lapini, A.; Scandolo, S.; Righini, R.; Bini, R. *J. Phys. Chem. Lett.* **2014**, *5*, 3804–3809.
- Finney, J.; Bowron, D.; Soper, A.; Loerting, T.; Mayer, E.; Hallbrucker, A. *Phys. Rev. Lett.* **2002**, *89*, 205503(4).
- Fox, M., *Optical Properties of Solids*; Oxford University Press: 2010.
- Fresneau, A.; Danger, G.; Rimola, A.; Theule, P.; Duvernay, F.; Chiavassa, T. *MNRAS* **2014**, *443*, 2991–3000.
- Gálvez, Ó.; Maté, B.; Herrero, V.; Escribano, R. *Astrophys. J.* **2011**, *738*, 133–138.
- Guilhaus, M. *J. Mass. Spectrom.* **1995**, *30*, 1519–1532.
- Giovambattista, N.; Stanley, H.; Sciortino, F. *Phys. Rev. Lett.* **2005**, *94*, 107803.
- Giobambattista, N.; Amann-Winkel, K.; Loerting, T. In *Liquid Polymorphism: Advances in Chemical Physics, Volume 152*, Stanley, H., Ed.; John Wiley & Sons, Inc.: Somerset, NJ, 2013.
- De Grotthuss, C. *Ann. Chim.* **1806**, *58*, 54–73.
- Günster, J.; Liu, G.; Stultz, J.; Krischok, S.; Goodman, D. W. *J. Phys. Chem. B* **2000**, *104*, 5738–5743.
- Halfen, D.; Apponi, A.; Ziurys, L. *Astrophys. J.* **2001**, *561*, 244–253.
- Hama, T.; Watanabe, N. *Chem. Rev.* **2013**, *113*, 8783–8839.
- Hansen, C.; Shemansky, D.; Esposito, L.; Stewart, A.; Lewis, B.; Colwell, J.; Hendrix, A.; West R.A., W. J.; J.H. Teolis, B.; Magee, B. *Geophys. Res. Lett.* **2011**, *38*, L11202.
- Hasselbrink, E.; Jakubith, S.; Nettesheim, S.; Wolf, M.; Cassuto, A.; Ertl, G. *J. Chem. Phys.* **1990**, *92*, 3154–3169.
- Hawkins, S.; Kumi, G.; Malyk, S.; Reisler, H.; Wittig, C. *Chem. Phys. Lett.* **2005**, *404*, 19–24.
- Herbst, E. *AIP Con. Proceed.* **2013**, *1543*, 15–30.
- Hisatsune, I. *J. Phys. Chem.* **1961**, *65*, 2249–2253.

- Hisatsune, I.; Miller Jr., P. J. *Chem. Phys.* **1963**, *38*, 49–54.
- Ho, W. In *Desorption Induced by Electronic Transitions*, Betz, G., Varga, P., Eds.; Springer-Verlag: Berlin, 1990.
- Hobbs, P. V., *Ice physics*; Oxford: Clarendon Press: 1974.
- Hurford, A.; Helfenstein, P.; Hoppa, G.; Greenberg, R.; Bills, B. *Nature* **2007**, *447*, 292–294.
- Huth-Fehre, T.; Becker, C. *Rapid Commun. Mass Sp.* **1991**, *5*, 378–382.
- Iess, L.; Stevenson, D. J.; Parisi, M.; Hemingway, D.; Jacobson, R. A.; Lunine, J. I.; Nimmo, F.; Armstrong, J. W.; Asmar, S. W.; Ducci, M.; Tortora, P. *Science* **2014**, *344*, 78–80.
- Jenniskens, P.; Blake, D.; Wilson, M.; Pohorille, A. *Astrophys. J.* **1995**, *455*, 389–401.
- Johari, G.; Andersson, O. *Thermochim. Acta* **2007**, *461*, 14–43.
- Jones, L.; Swanson, B.; Agnew, S. J. *Chem. Phys.* **1985**, *82*, 4389–4390.
- Kang, H. *Acc. Chem. Res.* **2005**, *38*, 893–900.
- Kawasaki, M.; Kasatani, K.; Hiroyasu, S.; Shinohara, H.; Nobuyuki, N. *Chem. Phys.* **1983**, *78*, 65–74.
- Y.K., K.; Rudd, M. *Phys. Rev. A* **1994**, *50*, 3954–3966.
- Kim, Y. D.; Stultz, J.; Goodman, D. W. *J. Phys. Chem. B* **2002**, *106*, 1515–1517.
- Kim, J.; Kim, Y.; Kang, H. *J. Chem. Phys.* **2009**, *131*, 0044705.
- Kim, S.; Kang, H. *J. Phys. Chem. Lett.* **2010**, *1*, 3085–3089.
- Kimmel, G.; Stevenson, K.; Dohnálek, Z.; Smith, R.; Kay, B. *J. Chem. Phys.* **2001**, *114*, 5284–5294.
- Kimmel, G.; Stevenson, K.; Dohnálek, Z.; Smith, R.; Kay, B. *J. Chem. Phys.* **2001**, *114*, 5295–5303.
- Knözinger, E.; Jacob, K.; Hofmann, P. *J. Chem. Soc. Faraday Trans.* **1993**, *89*, 1101–1107.
- Kondo, T.; Kato, H.; Bonn, M.; Kawai, M. *J. Chem. Phys.* **2007**, *127*, 094703.
- König, H. *Z. Kristallogr.* **1944**, *105*, 279–286.
- Korolik, M.; Suchan, M.; Johnson, M.; Arnold, D.; Reisler, H.; Wittig, C. *Chem. Phys. Lett.* **2000**, *326*, 11–21.

- Kumi, G.; Malyk, S.; Hawkins, S.; Reisler, H.; Wittig, C. *J. Phys. Chem. A* **2006**, *110*, 2097–2105.
- Kvick, Å.; McMullan, R.; Newton, M. *J. Chem. Phys.* **1982**, *78*, 3754–3761.
- Laufer, D.; Bar-Nun, A.; Igal, P.; Jacovi, R. *Icarus* **2013**, *222*, 73–80.
- Lee, C.; Lee, P.; Kim, Y.; Kang, H. *J. Chem. Phys.* **2007**, *127*, 084701.
- Letfullin, R.; Joenathan, C.; George, T.; Zharov, V. *Nanomedicine* **2006**, *1*, 473–480.
- Lignell, H.; Varner, M.; Finlayson-Pitts, B.; Benny Gerber, R. *J. Chem. Phys.* **2012**, *405*, 52–59.
- Limmer, D.; Chandler, D. *PNAS* **2014**, *111*, 9413–9418.
- Linstrom, P., Mallard, W., Eds. NIST Chemistry WebBook, NIST Standard Reference Database Number 69., <http://webbook.nist.gov> (accessed 05/04/2015).
- Lippert, T. *Plasma Process. Polym.* **2005**, *2*, 525–546.
- Livingston, F.; Smith, J.; George, S. *Anal. Chem.* **2000**, *72*, 5590–5599.
- Loerting, T.; Giovambattista J. *Phys. Condens. Matter* **2006**, *18*, R919–R977.
- Loerting, T.; Salzmann, C.; Kohl, I.; Mayer, E.; Hallbrucker, A. *Phys. Chem. Chem. Phys.* **2001**, *3*, 5355–5357.
- Loerting, T.; Winkel, K.; Seidl, M.; Bauer, M.; Mitterdorfer, C.; Handle, P.; Salzmann, C.; Mayer, E.; Finney, J.; Bowron, D. *Phys. Chem. Chem. Phys.* **2011**, *13*, 8737–8794.
- Loparo, J.; Roberts, S.; Tokmakoff, A. *J. Chem. Phys.* **2006**, *125*, 194521.
- Lorazo, P.; Lewis, L.; Meunier, M. *Phys. Rev. Lett.* **2003**, *91*, 225502.
- Malenkov, G. *J. Phys: Condens. Matter* **2009**, *21*, 283101.
- Malyk, S.; Kumi, G.; Reisler, H.; Wittig, C. *J. Phys. Chem. A* **2007**, *111*, 13365–13370.
- Malyk, S. Transport and Guest-Host Interactions in Amorphous and Crystalline Ice., Ph.D. Thesis, University of Southern California, 2009.
- Manca, C.; Martin, C.; Roubin, P. *J. Phys. Chem. B* **2003**, *107*, 8929–8934.
- Manca, C.; Martin, C.; Roubin, P. *Chem. Phys.* **2004**, *300*, 53–62.
- Maté, B.; Rodríguez-Lazcano, Y.; Herrero, V. *Phys. Chem. Chem. Phys.* **2012**, *14*, 10595–10602.

Matthias, E.; Reichling, M.; Siegel, J.; Käding, O.; Petzoldt, S.; Skurk, H.; Bizenberger, P.; Neske, E. *Appl. Phys. A* **1994**, *58*, 129–136.

May, R.; Smith, R.; Kay, B. J. *Phys. Chem. Lett.* **2012**, *3*, 327–331.

May, R.; Smith, R.; Kay, B. J. *Chem. Phys.* **2013**, *138*, 104501.

May, R.; Smith, R.; Kay, B. J. *Chem. Phys.* **2013**, *138*, 104502.

McGonagle, D.; Ziurys, L.; Irvine, W.; Minh, Y. *Astrophys. J.* **1990**, *359*, 121–124.

McKean, S. M. Energy Transfer in Amorphous Solid Water: Light-Mediated Expulsion of N₂O₄ Guest Molecules., Ph.D. Thesis, University of Southern California, 2015.

Mélen, F.; Pokorni, F.; Herman, M. *Chem. Phys. Lett.* **1992**, *194*, 181–186.

Mitlin, S.; Leung, K. J. *Phys. Chem. B* **2002**, *106*, 6234–6247.

Mishima, O.; Calvert, L.; Whalley, E. *Nature* **1984**, *310*, 393–395.

Mishima, O.; Stanley, H. *Nature* **1998**, *396*, 329–335.

Mooney, J.; Kambhampati, P. J. *Phys. Chem. Lett.* **2013**, *4*, 3316–3318.

Moore, E.; Molinero, V. *Phys. Chem. Chem. Phys.* **2011**, *13*, 20008–20016.

Nedyalkov, N.; Imamova, S.; Atanasov, P.; Toshkova, R.; Gardeva, E.; Yossifova, L.; Alexandrov, M.; Obara, M. *Appl. Surf. Sci.* **2011**, *257*, 5456–5459.

Ogai, A.; Qian, C.; Iwata, L.; Reisler, H. *Chem. Phys. Lett.* **1988**, *146*, 367–374.

Pan, Y.; Cotter, R. *Org. Mass Spectrom.* **1992**, *27*, 3–8.

Park, S.; Jung, K.; Kang, H. J. *Chem. Phys.* **2004**, *121*, 2765–2774.

Perez, D.; Lewis, L. *Appl. Phys. A* **2004**, *79*, 987–990.

Perez, D.; Lewis, L.; Lorazo, P.; Meunier, M. *Appl. Phys. Lett.* **2006**, *89*, 141907.

Poole, P.; Essmann, U.; Sciortino, F.; Stanley, H. *Phys. Rev. E* **1993**, *48*, 4605–4610.

Porco, C.; DiNino, D.; Nimmo, F. *Astron. J.* **2014**, *148*, 45.

Qian, C.; Ogai, A.; Iwata, L.; Reisler, H. J. *Chem. Phys.* **1990**, *92*, 4296–4307.

Raut, U.; Famá, M.; Teolis, B.; Baragiola, R. J. *Chem. Phys.* **2007**, *127*, 204713.

Ready, J. J. *Appl. Phys.* **1965**, *36*, 462–468.

- Rebolledo-Mayoral, O.; Stomberg, J.; McKean, S.; Reisler, H.; Wittig, C. *J. Phys. Chem. C* **2012**, *116*, 563–569.
- Rice, S.; Sceats, M. *J. Phys. Chem.* **1981**, *85*, 1108–1119.
- Rieley, H.; McMurry, D.; Haq, S. *Faraday Trans.* **1996**, *92*, 933–939.
- Rieley, H.; Colby, D.; McMurry, D.; Reeman, S. *J. Phys. Chem. B* **1997**, *101*, 4982–4991.
- Robert, F. *Science* **2001**, *293*, 1056–1058.
- Russ, F. *Z. Phys. Chem.* **1914**, *82*, 217–222.
- Safarik, D.; Mullins, C. *J. Chem. Phys.* **2004**, *121*, 6003–6010.
- Sarafian, A.; Nielsen, S.; Marschall, H.; McCubbin, F.; Monteleone, B. *Science* **2014**, *31*, 623–626.
- Schober, H.; Koza, M.; Tölle, A.; Masciovecchio, C.; Sette, F.; Fujara, F. *Phys. Rev. Lett.* **2000**, *85*, 4100–4103.
- Shalit, A.; Perakis, F.; Hamm, P. *J. Phys. Chem. B* **2013**, *117*, 15512–15518.
- Shephard, J.; Evans, J.; Salzmann, C. *J. Phys. Chem. Lett.* **2013**, *4*, 3672–3676.
- Slack, G. A. *Phys. Rev.* **1962**, *126*, 427–441.
- Smith, R.; Huang, C.; Wong, E.; Kay, B. *Phys. Rev. Lett.* **1997**, *79*, 909–912.
- Smith, R.; Huang, C.; Kay, B. *J. Phys. Chem. B* **1997**, *101*, 6123–6126.
- Smith, R.; Kay, B. *Nature* **1999**, *398*, 788–791.
- Smith, R.; Zubkov, T.; Dohnálek, Z.; Kay, B. *J. Phys. Chem. B* **2009**, *113*, 4000–4007.
- Smith, R.; Petrik, N.; Kimmel, G.; Kay, B. *Acc. Chem. Res.* **2012**, *45*, 33–42.
- Smoluchowski, R. *Astrophys. J.* **1981**, *244*, L31–L34.
- Starr, D.; Weis, C.; Yamamoto, S.; Nilsson, A.; Bluhm, H. *J. Phys. Chem. C* **2009**, *113*, 7355–7363.
- Stirniman, M. J.; Huang, C.; Smith, R. S.; Joyce, S. A.; Kay, B. D. *J. Chem. Phys.* **1996**, *105*, 1295–1298.
- Suchan, M. M. Molecule-Surface Interactions in HCl/MgO and Water/MgO Systems., Ph.D. Thesis, University of Southern California, 2001.
- Susa, A.; Koda, S. *J. Atmos. Chem.* **2003**, *43*, 197–217.

- Thrower, J.; Burke, D.; Collings, M.; Dawes, A.; Holtom, P.; Jamme, F.; Kendall, P.; Brown, W.; Clark, I.; Fraser, H.; McCoustra, M.; Mason, N.; Parker, A. *Astrophys. J.* **2008**, *673*, 1233–1239.
- Thrower, J.; Collings, M.; McCoustra, M.; Burke, D.; Brown, W.; Dawes, A.; Holtom, P.; Kendall, P.; Mason, N.; Jamme, F.; Fraser, H.; Clark, I.; Parker, A. *J. Vac. Sci. Tech.* **2008**, *26*, 919–924.
- Tielens, A.; Hagen, W. *Astron. Astrophys.* **1982**, *114*, 245–260.
- Thrower, J.; Collings, M.; McCoustra, M.; Burke, D.; Brown, W. A.; Dawes, A.; Holtom, P.; Kendall, P.; Mason, N.; Jamme, F.; Fraser, H.; Clark, I.; Parker, A. *J. Vac. Sci. Technol., A* **2008**, *26*, 919–924.
- Thrower, J.; Burke, D.; Collings, M.; Dawes, A.; Holtom, P.; Jamme, F.; Kendall, P.; Brown, W. A.; Clark, I.; Fraser, H.; McCoustra, M.; Mason, N.; Parker, A. *Astrophys. J.* **2008**, *673*, 1233–1239.
- Thrower, J.; Abdalgilil, A.; Collings, M.; McCoustra, M.; Burke, D.; Brown, W.; Dawes, A.; Holtom, P.; Kendall, P.; Mason, N.; Jamme, F.; Fraser, H.; Rutten, F. *J. Vac. Sci. Technol., A* **2010**, *28*, 799–806.
- Tse, J. *J. Chem. Phys.* **1992**, *1992*, 5482–5487.
- Tyndall, G.; Stedman, K.; Schneider, W.; Burrows, J.; Moortgat, G. *J. Photochem.* **1987**, *36*, 133–139.
- Vandaele, A.; Hermans, C.; Simon, P.; Carleer, M.; Colin, R.; Fally, S.; Mérienne, M.; Jenourvriar, A.; Coquart, B. *J. Quant. Spectrosc. Radiat. Transfer* **1998**, *59*, 171–184.
- Vega, C.; Abascal, J.; Conde, M.; Aragones, J. *Faraday Discuss.* **2009**, *141*, 251–276.
- Van Dishoeck, E.; Herbst, E.; Neufeld, D. *Chem. Rev.* **2013**, *113*, 9043–9085.
- Wenzel, J.; Linderstrom-Lang, C.; Rice, S. *Science* **1975**, *187*, 428–430.
- Werner, D.; Hashimoto, S. *J. Phys. Chem. C* **2011**, *115*, 5063–5072.
- Wiley, W.; McLaren, I. *Rev. Sci. Instrum.* **1955**, *26*, 1150–1157.
- Yang, R.; Gudipati, M. *J. Chem. Phys.* **2014**, *140*, 104202.
- Yabushita, A.; Inoue, Y.; Senta, T.; Kawasaki, M.; Sato, S. *J. Chem. Phys. A* **2004**, *108*, 438–446.
- Yabushita, A.; Kanda, D.; Kawanaka, N.; Kawasaki, M.; Ashfold, M. *J. Chem. Phys.* **2006**, *125*, 133406.

Zhigilei, L.; Kodali, P.; Garrison, B. *Chem. Phys. Lett.* **1997**, *276*, 269–273.

Zhigilei, L.; Kodali, P.; Garrison, B. *J. Phys. Chem. B* **1998**, *102*, 2845–2853.

Zhigilei, L.; Garrison, B. *Rapid Commun. Mass Sp.* **1998**, *12*, 1273–1277.